NASA Contractor Report 4618

Development of a Near-Wall Reynolds-Stress Closure Based on the SSG Model for the Pressure Strain

R. M. C. So, H. Aksoy, T. P. Sommer, and S. P. Yuan
Arizona State University • Tempe, Arizona

National Aeronautics and Space Administration
Langley Research Center • Hampton, Virginia 23681-0001

Prepared for Langley Research Center
under Grant NAG1-1080

August 1994

Summary

Three terms in the Reynolds-stress equation need modeling; they are the turbulent diffusion tensor, the dissipation rate tensor and the velocity-pressure-gradient correlation tensor. Since the diffusion term is of higher order compared to the dissipation rate and velocity-pressure-gradient terms, its model does not need modification in the near-wall region. Numerous high-Reynolds-number models are available for the other two terms. There is considerable agreement on how to improve the near-wall behavior of the dissipation rate tensor, because very near the wall viscous diffusion exactly balances viscous dissipation. On the other hand, there is not much agreement on the proper near-wall modeling of the velocity-pressure-gradient correlation tensor. If the near-wall modifications are to vanish away from the wall, the high-Reynolds-number closure of the Reynolds-stress equations should be recovered exactly. Therefore, near-wall modifications proposed for the velocity-pressure-gradient correlation tensor would depend on the choice of the model adopted for the pressure strain part of this term.

Near-wall modifications to the different pressure-strain models have been proposed by various researchers. However, none has been as thoroughly tested as the proposal put forward by Zhang (1993), who has validated the near-wall model against a wide variety of turbulent flows ranging from simple channel flows to compressible boundary layers at a free stream Mach number greater than 10. His proposal was based on the Launder et al. (1975) or LRR model for the pressure-strain term and the near-wall corrections for this model derived by Lai and So (1990). In order to achieve good correlation with measurements, Zhang (1993) found that an additional term proportional to the product of the turbulent kinetic energy and the strain rate tensor was required in the near-wall proposal of Lai and So (1990). Furthermore, the coefficient modifying this additional term has to be made parametric in the flow Reynolds number and the free stream Mach number and this led to three different functional forms for the coefficient depending on whether the flow to be modeled is an internal flow, an external flow or a compressible flow. Zhang (1993) also found that one of the damping function required modification if adverse pressure gradient flows were to be calculated correctly.

In this research, a near-wall second-order closure based on the Speziale et al. (1991) or SSG model for the pressure-strain term is proposed. Unlike the LRR model, the SSG model is quasi-nonlinear and yields better results when applied to calculate rotating homogeneous turbulent flows. An asymptotic analysis near the wall is applied to both the exact and modeled equations so that appropriate near-wall corrections to the SSG model and the modeled dissipation-rate equation can be derived to satisfy the physical wall boundary conditions as well as the asymptotic near-wall behavior of the exact equations. Two additional model constants are introduced and they are determined by calibrating against one set of near-wall channel flow data. Once determined, their values are found to remain constant irrespective of the type of flows examined. The resultant model is used to calculate simple turbulent flows, near separating turbulent flows, complex turbulent flows and compressible turbulent flows with a free stream Mach number as high as 10. In all the flow cases investigated, the calculated results are in good agreement with data. This new near-wall model is less ad hoc, physically and mathematically more sound and eliminates the empiricism introduced by Zhang (1993). Therefore, it is quite general, as demonstrated by the good agreement achieved with measurements covering a wide range of Reynolds numbers and Mach numbers.

Table of Contents

I. Introduction

The need to introduce near-wall corrections to the pressure-strain term in the modeled Reynolds-stress equation was first recognized by Rotta (1951) and later formalized by Launder et al. (1975). Following the arguments of Rotta (1951), Launder et al. (1975) made a proposal, which has two contributions to the near-wall effect, to account for the disturbances created in the turbulence field by the reflection of the fluctuating pressure in the immediate vicinity of a solid boundary. One contribution corresponded to the reflected-wall influence of the slow part of the pressure-strain model while another contribution accounted for a similar influence of the rapid part. The proposal of Launder et al. (1975), however, failed to satisfy the physical wall boundary conditions for the mean velocities and Reynolds stresses. Consequently, some kind of wall functions have to be invoked in the numerical solution of these modeled equations. Since then, numerous proposals have been made to remedy this shortcoming, so that the governing equations can be integrated directly to the wall. Among the proposals put forward, the models of Hanjalic and Launder (1976), Prud'homme and Elghobashi (1983), Kebede et al. (1984), So and Yoo (1986), Shima (1988), Launder and Tselepidakis (1988), Launder and Shima (1989), Lai and So (1990) and Tselepidakis (1991) can be mentioned. Some of these models have even been validated against complex turbulent flows. Three successful examples can be cited; these are the calculation of a direct numerical simulation (DNS) of a fully developed turbulent flow in a curved channel by So et al. (1991a), the curved pipe flow calculations of Lai et al. (1991a, b) and the rotating pipe flow modeling of Tselepidakis (1991).

A systematic evaluation of the asymptotic behavior of these near-wall second-order models has been carried out by So et al. (1991b). The analyses were compared with the behavior of the exact equations. Also, a comparison of the models' ability to replicate a low-Reynolds-number plane channel flow was performed. In addition, the models were evaluated for their ability to predict the turbulence statistics and the limiting behavior of the structrue parameters compared to DNS data of a fully developed turbulent channel flow (Kim et al. 1987; Mansour et al. 1988). With the exception of the models proposed by Launder and Shima (1989) and Lai and So (1990), none of the models examined were asymptotically correct. Although these two models perform better than others in their predictions of the mean flow and turbulence statistics, they too fail to reproduce the log-law correctly and under-predict the distributions of the turbulent kinetic energy, k, and its dissipation rate, ε, in the near-wall region. Also, all models examined yield a von Karman constant, κ, quite a bit different from the accepted value of 0.41.

Two discrepancies invariably show up when these models are used to calculate simple wall-bounded flows at low bulk Reynolds numbers. One is the poor prediction of the mean velocity in the buffer region and this leads to an inacurate estimate of κ. Another is the incorrect prediction of the near-wall dissipation rate profile and its value at the wall. These two points are very well illustrated by the comparisons of the model calculations with the DNS data of Kim et al. (1987) shown in Figs. 1 and 2. The DNS channel flow data was obtained at a $Re_\tau = u_\tau h/\nu = 180$ which corresponds to a bulk Reynolds number of about 5,600. In these plots, $U^+ = U/u_\tau$, $y^+ = yu_\tau/\nu$ and $\varepsilon^+ = \varepsilon\nu/u_\tau^4$, where U is the mean axial velocity, y is the normal wall coordinate, u_τ is the wall friction velocity, h is the channel half width and ν is the kinematic viscosity. Two model calculations are shown; one labeled LS is from the model of Lai and So (1990), another designated NWLRR is from Zhang (1993) who derived the near-wall corrections based on the Launder et al. (1975) model minus their near-wall corrections, or the commonly labeled LRR model, and solved the ε equation of So et al. (1991c) instead of that adopted by Lai and So (1990). The reason was to improve the prediction of the near-wall behavior of ε. Indeed, the prediction of ε is improved but the calculation of the mean velocity is significantly worse than before. The NWLRR model also gives an incorrect prediction (Fig. 3) of the flat plate boundary layer DNS data of Spalart (1988). Among the near-wall Reynolds-stress models referred to above, not a single model can simultaneously predict the DNS data of Moser and Moin (1987), Kim et al. (1987), Mansour et al. (1988), Spalart (1988) and Lee and Kim (1991) correctly without having to adjust the damping functions in the models. It seems that these poor predictions have little to do with whether the modeled equations are asymptotically consistent. Of course, if they are not, their predictions of the near-wall asymptotes will be very much in error. Therefore, some other factors besides asymptotic consistency influence the predictions of the mean velocity in the buffer region and the near-wall distribution of ε.

It is argued that the incorrect prediction of the mean velocity could be attributed to the performance of the velocity-pressure-gradient correlation model in the near-wall region. Conventional modeling of this correlation term splits it into a pressure-diffusion term and a pressure-strain term. For high-Reynolds-number flows, it is argued that the pressure-diffusion term is small compared to turbulent diffusion and can be neglected. The model for the pressure-strain term is formulated for homogeneous, unbounded turbulent flows with high Reynolds numbers. The presence of a wall gives rise to a reflection of the pressure fluctuations and this, in turn, has an effect on the turbulence field. If the boundary conditions for the pressure are homogeneous, the solution of the Poisson equation for the fluctuating pressure consists of two parts; a rapid part and a slow (return-to-isotropy) part. However, Mansour et al. (1988) showed that for wall-bounded flows, the inhomogeneous pressure boundary condition introduces a third part to this solution. This is the Stokes part and is a consequence of the wall reflection of the fluctuating pressure.

Many researchers assumed that the Stokes part is not important compared to the slow and rapid parts. Therefore, it is usually neglected. However, the importance of this term in near-wall flow modeling was recognized by Launder et al. (1975) and emphasized by Launder and Tselepidakis (1991). The latter work adopted a recent near-wall second-order model and introduced an additional near-wall correction to the pressure-strain model. They managed to improve the prediction of the mean velocity; however, the calculation of the near-wall behavior of the dissipation rate was incorrect. According to Zhang (1993), the near-wall prediction of the dissipation rate could be improved by suitably modifying the dissipation-rate equation alone, while maintaining asymptotic consistency in the near-wall region for the Reynolds stresses. Their NWLRR calculations showed that the predicted behavior of the dissipation rate is correct near a wall but the calculations of the mean velocity in the buffer region is very much in error (Fig. 1).

The wall reflection correction proposed by Launder et al. (1975) has two parts; one corresponding to the reflected-wall influence of the slow part and another corresponding to the reflected-wall influence of the rapid part of the pressure-strain model. This latter contribution is also referred to as the mean strain part of the near-wall effect. In a rigorous derivation of the model for the mean strain part based on kinematic considerations, Launder et al. (1975) found that there should be two terms in the model. The first term was related to stress production while the second term is related to kS_{ij}, where S_{ij} is the strain-rate tensor. Since the second term only contributed to the shear stress equation alone in a two-dimensional wall-bounded flow, Launder et al. (1975) argued that it was not as important as the first term in the determination of stress anisotropy near a wall. Consequently, the coefficient associated with the second term could be set to zero without loss of generality.

It is precisely for the reason that the second term only contributes to the shear stress equation that this term is expected to have an effect on the prediction of the mean velocity near a wall. Therefore, Zhang (1993) argued for its inclusion and proceeded to modify his NWLRR model. He labeled the modified model as LRR/WR. When the LRR/WR model was used to calculate the DNS data of Spalart (1988), significant improvements were obtained (Fig. 3). Even then, κ was under-estimated by about 15%. However, the predicted ε near the wall followed the DNS trend closely even though the quantitative agreement was not as good. In spite of the slight discrepancies shown at low Reynolds numbers, it can be argued that a near-wall model capable of predicting both the mean velocity and the near-wall behavior of ε fairly well has been deduced. Zhang (1993) applied the LRR/WR model to calculate three different types of flows: internal flows, external flows and compressible flows. Channel as well as Couttee flows were considered in the internal flow category, while flat plate and near-separating boundary layers were calculated in the external flow category. As for compressible flows, a wide range of free stream Mach numbers and wall thermal boundary conditions, ranging from cooled wall to heated wall, were examined. In all these comparisons, good agreement with measurements was obtained provided that the coefficient associated with the term kS_{ij} was made to depend on the flow Reynolds number and Mach Number. Three different functional relations were found to be necessary; one for internal flows, one for external flows and one for compressible flows. Furthermore, it was found necessary to modify the damping function used to limit the extent of the influence of the near-wall corrections for near-separating flow calculations. In essence, the damping function was made to be dependent on a pressure gradient parameter. Physically, all these modifications are rather ad hoc. Therefore, there is a need to continue the search for a more general and less ad hoc approach to derive near-wall corrections to high-Reynolds-number second-order models that are valid for different types of flows with wide ranging Reynolds numbers and Mach numbers.

II. Objectives

There are four objectives in the present research. The first objective is to search for a more suitable model for the velocity-pressure-gradient correlation tensor to use as a base for the derivation of the near-wall corrections. A second objective is to derive appropriate near-wall corrections to the chosen velocity-pressure-gradient model and the associated dissipation-rate equation. The third objective is to validate the near-wall model thus derived over as wide a range of flow data as possible. Finally, the fourth objective is to test the model in different numerical schemes, ranging from simple Newton iteration scheme to two-dimensional elliptic scheme to partially parabolic three-dimensional scheme. The approaches taken to achieve these objectives are outlined below.

Since the proposals of Rotta (1951) and Launder et al. (1975) for the slow and rapid parts of the pressure-strain tensor, much work on pressure-strain modeling has been carried out. Their models are essentially linear. Nonlinear models for the slow and rapid parts have been proposed, for example, by Lumley (1978), Shih and Lumley (1985), Fu et al. (1987) and Speziale et al. (1991). The nonlinear models of Lumley (1978) and Shih and Lumley (1985) have been primarily developed through the use of realizability constraints while that of Speziale et al. (1991) is derived by means of invariant tensor function theory. While the Shih and Lumley (1985) or SL model is nonlinear in both the slow and rapid parts, the Speziale et al. (1991) or SSG model is only quadratically nonlinear in the anisotropic tensor. Their model is formulated to be linear in the rapid part because the energy spectra of the Reynolds stresses are linear. Speziale et al. (1992) show that the SSG model gives the best results when it is applied to calculate a variety of turbulent flows where DNS data are available. They have compared their results with those obtained using the LRR model, the SL model and the Fu et al. (1987), or FLT model. Further evidence of the superior predictive capability of the SSG model is provided by Demuren and Sarkar (1992) who examined a number of models for their ability to calculate channel flows accurately, in particular their ability to correctly recover the log-law and the von Karman constant, κ, assuming wall functions to satisfy the wall boundary conditions. Based on these comparative studies, it is clear that the SSG model is capable of yielding the log behavior correctly and, therefore, is the most suitable model to use for the derivation of asymptotically consistent near-wall corrections to the modeled Reynolds-stress equation.

The near-wall corrections are derived by imposing the condition of asymptotic consistency in the near-wall region. Thus, the contributions of the Stokes part are suitably accounted for and the modeled equations are made to behave like the exact equations, at least to the lowest order of the wall normal coordinate. Simultaneously, the exact and modeled ε equation are analysed for their near-wall behavior and new near-wall corrections are proposed that are consistent with the improvements made to the modeled Reynolds-stress equation. Thus, the new near-wall second-order model is entirely different from the NWLLR and LRR/WR models proposed by Zhang (1993). It is hoped that this new near-wall second-order model, hereafter called Present model, will be able to mimick the near-wall flow as well as the log layer behavior correctly and, at the same time, yield uniformly valid predictions for internal and external wall-bounded turbulent flows, with and without adverse pressure gradient effects, covering a wide range of Reynolds numbers and Mach numbers.

Validations of the Present model are divided into three different categories. A simple flow category consists of internal as well as external flows where DNS data and accurate measurements are available. Specifically, the cases chosen in this category are the channel flow DNS data of Kim et al. (1987) and Kim (1991), the Couette flow DNS data of Lee and Kim (1991), the combined channel/Couette flow measurements of El Telbany and Reynolds (1980, 1981), the pipe flow measurements of Durst et al. (1993), Schildknecht et al. (1979) and Laufer (1954), the flat plate boundary layer DNS data of Spalart (1988) and the boundary-layer measurements of Karlsson and Johansson (1988) and Klebanoff (1954). The second category examined is simple compressible turbulent flows where the validity of the direct extension of incompressible modeling to compressible flows and Morkovin's (1962) hypothesis is tested. The data sets selected are the adiabatic and cooled wall measurements collected by Fernholz and Finley (1977), the highly cooled wall investigation of Kussoy and Horstman (1991) and the heated wall study of Spina and Smits

(1987). Finally, the model is tested for its ability to predict complex turbulent flows. Here, three representative complexities are investigated. One is related to adverse pressure gradient effects and this is represented by the experiments of Samuel and Joubert (1974). Another complexity is associated with turbulence driven secondary motions and this is evaluated by comparing with the fully-developed square duct flow measurements of Lund (1977) and Eppich (1982). The third complexity tested is introduced by system rotation and this is validated against the axially rotating pipe flow measurements of Kikuyama et al. (1983). Zhang (1993) has made calculations of most of these cases. For those cases that Zhang (1993) has not carried out, calculations will also be made using the LRR/WR model. This way, a complete comparison of the two near-wall models can be made and their pros and cons can be assessed.

The ease with which the model can be used with any numerical scheme without the introduction of any undue numerical instability is tested by implenting it into a number of different numerical schemes to solve flow problems. For example, fully-developed flows are solved using either a time march technique (So and Sarkar 1994) or a Newton iteration scheme (Lai and So 1990), because the governing equations can either be reduced to hyperbolic type or to ordinary differential equations. These techniques are used to solve simple internal flow problems. A parabolic code based on the computer program of Anderson and Lewis (1971) is used to calculate boundary-layer flows, incompressible as well as compressible. On the other hand, a two-dimensional elliptic code (Yoo and So 1991) is used to calculate developing flow in an axially rotating pipe. Finally, the partially parabolic three-dimensional code of Lai et al. (1991a, b) is modified to calculate the flow in a square duct. Therefore, the model is tested in simple as well as complicated numerical codes. The presence or absence of numerical instabilities in these calculations is an indication of the robustness of the model.

III. Near-Wall Turbulence Closure Based on the SSG Model

Governing equations

Incompressible turbulent flows are governed by the Reynolds-averaged equations which can be written in Cartesian tensor form as:

$$\frac{\partial \overline{U}_i}{\partial x_i} = 0 \quad , \tag{1}$$

$$\frac{D\overline{U}_i}{Dt} = -\frac{1}{\rho}\frac{\partial \overline{P}}{\partial x_i} + \nu\frac{\partial^2 \overline{U}_i}{\partial x_j \partial x_j} - \frac{\partial \overline{u_i u_j}}{\partial x_j} \quad , \tag{2}$$

where D/Dt is the material derivative, the upper case letters denote the Reynolds averaged quantities and the lower case letters are used to represent the corresponding fluctuating part. Here, the Einstein summation convention is followed, $\overline{U}_i$ is the ith component of the mean velocity, u_i is the ith component of the fluctuating velocity, $\overline{P}$ is the mean pressure, ρ is the fluid density, ν is the kinematic viscosity and x_i is the ith component of the coordinates. These equations need closure because of the presence of the Reynolds stress terms, $\overline{u_i u_j}$. If a Reynolds-stress or second-order closure is invoked, the equations governing the transport of the Reynolds stresses and the dissipation rate of the turbulent kinetic energy are given by (So et al. 1991b)

$$\frac{D\overline{u_i u_j}}{Dt} = \frac{\partial}{\partial x_k}\left(\nu\frac{\partial \overline{u_i u_j}}{\partial x_k}\right) + D_{ij}^T + \left[-\overline{u_i u_k}\frac{\partial \overline{U}_j}{\partial x_k} - \overline{u_j u_k}\frac{\partial \overline{U}_i}{\partial x_k}\right] + \Pi_{ij} - \varepsilon_{ij} \quad , \tag{3}$$

$$\frac{D\varepsilon}{Dt} = \frac{\partial}{\partial x_j}\left(\nu\frac{\partial \varepsilon}{\partial x_j}\right) + \frac{\partial}{\partial x_j}\left(C_\varepsilon\frac{k}{\varepsilon}\overline{u_i u_j}\frac{\partial \varepsilon}{\partial x_i}\right) + C_{\varepsilon 1}\frac{\varepsilon}{k}\widetilde{P} - C_{\varepsilon 2}\frac{\varepsilon\widetilde{\varepsilon}}{k} + \xi \quad , \tag{4}$$

where $\widetilde{\varepsilon} = \varepsilon - 2\nu\left(\partial\sqrt{k} / \partial y\right)^2$, $\widetilde{P}$ is the production of the turbulent kinetic energy, k and $C_\varepsilon = 0.12$, $C_{\varepsilon 1} = 1.50$, $C_{\varepsilon 2} = 1.83$ are constants introduced in the modeling of the ε-equation. The function ξ is identically zero for flows far away from a wall and is introduced to account for near-wall viscous effects. Its specific form will depend on the near-wall models formulated for the Reynolds-stress equation. Therefore, only ξ and D_{ij}^T, Π_{ij}, ε_{ij}, which are the turbulent diffusion tensor, the velocity-pressure-gradient correlation tensor and the dissipation rate tensor, respectively, need modeling in (3) and (4).

Near-wall SSG model

A fairly complete review of near-wall Reynolds-stress closures has been given by So et al. (1991b). Altogether, eight models were reviewed. The models reviewed are fairly similar in that they are based on the LRR model and its variations. There are very little differences in the modeling of the turbulent diffusion of Reynolds stresses because the term is of order y^3. As a result, this term does not need near-wall correction and the model used by Launder et al. (1975) for this term is adopted by most researchers. For high-Reynolds-number flows, the viscous dissipation rate tensor is usually modeled by invoking the assumption of equilibrium turbulence. This assumption cannot satisfy the no slip condition at the wall, therefore, for near-wall flows, the high-Reynolds-number model needs correction. Different forms of the near-wall correction to this term has been proposed by various researchers. However, the few differences that exist among these proposals are not sufficiently great to cause significant discrepancies between the calculated results. Therefore, the proposal of Lai and So (1990), derived by imposing the constraints of Launder and Reynolds (1983), can be adopted for this term. The models for the turbulent diffusion tensor and the viscous dissipation rate tensor can now be written as:

$$D_{ij}^T = \frac{\partial}{\partial x_k}\left[C_s \frac{k}{\varepsilon}\left(\overline{u_i u_l}\frac{\partial \overline{u_j u_k}}{\partial x_l} + \overline{u_j u_l}\frac{\partial \overline{u_k u_i}}{\partial x_l} + \overline{u_k u_l}\frac{\partial \overline{u_i u_j}}{\partial x_l}\right)\right] \quad , \tag{5}$$

$$\varepsilon_{ij} = \frac{2}{3}\varepsilon\,\delta_{ij} + f_{w1}\frac{\varepsilon}{k}\left[-\frac{2}{3}k\,\delta_{ij} + \frac{\overline{u_i u_j} + \overline{u_i u_k}\,n_k n_j + \overline{u_j u_k}\,n_k n_i + n_i n_j \overline{u_k u_l}\,n_k n_l}{1 + 3\overline{u_k u_l}\,n_k n_l / 2k}\right] \quad , \tag{6}$$

where $n_i = (0, 1, 0)$ is the wall unit normal.

The major difference comes in the modeling of the velocity-pressure-gradient correlation tensor. In most approaches, this tensor is split into two parts; a pressure diffusion part and a pressure strain part. The pressure diffusion part is generally neglected in high-Reynolds-number modeling. When near-wall models are devised, most researchers adopt this partition of the velocity-pressure-gradient correlation tensor, and seek a near-wall correction to the high-Reynolds-number model for the pressure strain part. The pressure diffusion part is again neglected. In view of this, the near-wall corrections devised for the pressure strain part will depend on the models adopted for this term. Most near-wall corrections proposed are derived based on the LRR model. The modeled terms consist of a slow part, or a return-to-isotropy part, and a rapid part which accounts for the effects of mean strain. Although this model gives good predictions of the flow behavior for a wide variety of simple shear flows at high Reynolds numbers, its performance for some types of flows, such as rotating homogeneous turbulent flow, near-separating flow, back-step flow, swirling flow, three-dimensional wall jet flow and simple flows at low Reynolds numbers, is not very satisfactory (see Figs. 1 - 3). For example, swirling flow could give rise to a stabilizing or a destabilizing effect on the flow, depending on whether the centrifugal forces created by flow rotation or the extra strain rates, that lead to additional turbulence production, are more pronounced. Therefore, if swirling flows are to be calculated correctly, the competing effects of the centrifugal forces and the extra strain rates have to be accounted for in the turbulence models.

As for the effects of wall proximity near a wall, Launder et al. (1975) suggested the following remedy. They argued that the rapid variation of the mean velocity near a wall could not have been the only factor to affect near-wall turbulence. Instead, they suggested that the wall proximity effects tend to increase the anisotropy of the normal stresses and diminish the shear stress. Furthermore, the wall influence is even felt in regions where the mean strain rates are negligible. Consequently, they proposed to modify their LRR model to include wall-proximity effects. Through a rigorous kinematic consideration, they found that there are two contributions to their corrections. One corresponds to the reflected-wall effects of the slow part and another to the reflected-wall effects of the rapid part. However, their corrections fail to satisfy the physical wall boundary conditions and are not asymptotically correct. Therefore, the resultant modeled equations cannot be integrated directly to the wall and again some kind of wall functions have to be invoked. Besides, their corrections give rise to a global effect even though they were supposed to correct for wall-proximity effects. On the other hand, the proposal of Lai and So (1990) to enforce asymptotic consistency offers a viable alternative. Their derived functional form is similar to that obtained by Launder et al. (1975); however, the coefficients modifying the terms are different. The major difference is that their corrections render the modeled equations valid all the way to the wall and there is no need to invoke wall functions for the numerical solutions of these equations. Furthermore, if swirling and other complex flows are to be calculated correctly, the model for the velocity-pressure-gradient correlation term should be able to account for rotational effects in the flow. According to Speziale et al. (1991), the inadequacy of the LRR model could be attributed to its linear behavior. Therefore, they proposed a modification which includes some nonlinear terms in the anisotropic tensor. The result is the SSG model for the pressure strain term. Since this model gives better prediction of rotating and other homogeneous turbulent flows (Speziale et al. 1992), the present work proposes to adopt this high-Reynolds-number model as base to derive a near-wall model for Π_{ij} so that wall proximity effects and pressure diffusion near a wall are accounted for in the model.

An asymptotic approach similar to that put forward by Lai and So (1990) is used to derive the near-wall correction to the SSG model. In order to ensure that the near-wall correction dies out far away from the wall, a damping function based on the turbulent Reynolds number is proposed for the near-wall correction term. Without going into details, the near-wall SSG model can be written as:

$$\begin{aligned}\Pi_{ij} = & -\left(2C_1\varepsilon + C_1^*\widetilde{P}\right) b_{ij} + C_2\varepsilon\left(b_{ik}b_{kj} - \frac{1}{3}\Pi\,\delta_{ij}\right) - \alpha_1\left(P_{ij} - \frac{2}{3}\widetilde{P}\,\delta_{ij}\right) \\ & - \beta_1\left(D_{ij} - \frac{2}{3}\widetilde{P}\,\delta_{ij}\right) - 2\left(\gamma_1 + \frac{C_3^*}{2}\Pi^{1/2}\right) k\,S_{ij} + \Pi_{ij}^{w} \quad . \end{aligned} \tag{7}$$

In this form, which is written differently from that given by Speziale et al. (1991), the meanings of the individual terms can be easily identified. The first term on the right is equivalent to Rotta's slow part, the second term is essentially the nonlinear contribution to the slow part, the third, fourth and fifth terms are similar to the rapid part proposed by Launder et al. (1975) and the last term is the near-wall correction proposed to render the model regular as a wall is approached. The unknown second-order tensors in (7) are given by:

$$b_{ij} = \frac{1}{2k}\left(\overline{u_iu_j} - \frac{2}{3}k\,\delta_{ij}\right) \quad , \tag{8a}$$

$$S_{ij} = (1/2)\left(\partial\overline{U}_i / \partial x_j + \partial\overline{U}_j / \partial x_i\right) \quad , \tag{8b}$$

$$P_{ij} = -\left[\overline{u_iu_k}\,\partial\overline{U}_j / \partial x_k + \overline{u_ju_k}\,\partial\overline{U}_i / \partial x_k\right] \quad , \tag{8c}$$

$$D_{ij} = -\left[\overline{u_iu_k}\,\partial\overline{U}_k / \partial x_j + \overline{u_ju_k}\,\partial\overline{U}_k / \partial x_i\right] \quad , \tag{8d}$$

where $2\widetilde{P} = P_{ii}$, $\Pi = b_{ij}b_{ij}$, $C_1 = 1.7$, $C_2 = 4.2$, $C_1^* = 1.8$, $C_3^* = 1.3$, $\alpha_1 = (C_4 + C_5)/4$, $\beta_1 = (C_4 - C_5)/4$, $\gamma_1 = (2C_4 - 3C_3)/6$, $C_3 = 0.8$, $C_4 = 1.25$ and $C_5 = 0.4$ are the model constants specified by Speziale et al. (1991) and Π_{ij}^w is the near-wall correcting function which is derived to be

$$\Pi_{ij}^w = f_{w1}\left[\left(2C_1\varepsilon + C_1^*\widetilde{P}\right)b_{ij} - C_2\varepsilon\left(b_{ik}b_{kj} - \frac{1}{3}\Pi\,\delta_{ij}\right) + \alpha^*\left(P_{ij} - \frac{2}{3}\widetilde{P}\,\delta_{ij}\right) + 2\gamma^* k\, S_{ij}\right] + \Pi_{ij}^P \quad . \tag{9}$$

Here, f_{w1} is the damping function and Π_{ij}^P is a near-wall correction proposed to account for pressure diffusion. The final expression derived for Π_{ij}^P can be written as

$$\Pi_{ij}^P = -\frac{1}{3}\left[\frac{\partial}{\partial x_l}\left(\nu\frac{\partial\overline{u_iu_k}}{\partial x_l}\right)n_kn_j + \frac{\partial}{\partial x_l}\left(\nu\frac{\partial\overline{u_ju_k}}{\partial x_l}\right)n_kn_i\right] + \frac{1}{3}\frac{\partial}{\partial x_m}\left(\nu\frac{\partial\overline{u_ku_l}}{\partial x_m}\right)n_kn_ln_in_j \quad . \tag{10}$$

Two near-wall model constants, α^* and γ^*, are introduced and they are optimized to take on values that would give the best prediction of the near-wall asymptotes for one particular fully-developed channel flow. Thus determined, their values are given by $\alpha^* = -0.29$ and $\gamma^* = 0.065$.

The form of (9) is very similar to that proposed by Launder et al. (1975). Three contributions to this correction can be identified. The last term Π_{ij}^P is to account for pressure diffusion which is traditionally neglected in high-Reynolds-number modeling and is absent from Launder et al.'s (1975) proposal. Without this term the modeled Reynolds-stress equation could not be balanced at a wall. The other four terms within the square brackets are essentially similar to those proposed by Launder et al. (1975). The first two terms correspond to the reflected-wall effects of the slow part while the last two terms correspond to the reflected-wall effects of the rapid part. A major difference between (9) and that proposed by Launder et al. (1975) is in the coefficients modifying the terms and the introduction of the damping function qualifying the terms within the square brackets. The damping function is necessary to ensure that the effects of the near-wall corrections are decreasing as y increases. As for the coefficients qualifying the first two terms, they have to be identical to those given in the slow part of (7) to ensure that (7) will satisfy the wall boundary conditions. Therefore, their values are exact and cannot be determined by calibration. On the other hand, the last two terms are of higher order and are not pivotal in determining near-wall balance. They, however, will affect stress anisotropy near the wall. Therefore, their coefficients are not exact and could be determind through calibration.

Since the damping function is introduced into the model to limit the extent of the influence of the near-wall correction, it should vanish at a reasonable distance away from the wall. It is precisely for this reason that it is very difficult to find one single damping function capable of yielding an influence over a limited y range over a wide range of Reynolds numbers. In the course of validating this new near-wall Reynolds-stress model, two damping functions are found to be necessary if different types of flows covering a very wide range of Reynolds numbers are to be predicted correctly. These damping functions are given by

$$f_{w1} = exp\left[-\left(\frac{Re_t}{200}\right)^2\right] \quad , \tag{11a}$$

$$f_{w1} = exp\left[-\left(\frac{ARe_t}{60}\right)^3\right] \quad , \tag{11b}$$

where $Re_t = k^2/\nu\varepsilon$ is the turbulent Reynolds number and $A = 1 - (9/2)(b_{ij}b_{ij} - 2b_{ij}b_{jk}b_{ki})$. The choice of the damping function depends on the flow Reynolds numbers. It is chosen so that the damping functions will vanish in the range $100 < y^+ = yu_\tau/\nu < 200$, depending on the flow Reynolds numbers and the type of flow considered. For example, when channel flow at $Re_\tau = 395$ is calculated, (11a) is more suitable. On the other hand, when Re_τ is reduced to 180, (11b) is appropriate. The same trend is also found for Couette flow, pipe flow, boundary-layer flow with and without adverse pressure gradients, compressible flow and other complex flows. It will be seen later that, for most of the cases calculated, (11a) is used, while (11b) is only used for three cases where the Reynolds numbers are among the lowest in all the flow cases considered.

A similar approach is used to derive the near-wall correcting function ξ for the ε-equation. Again, without going into details, the final result is

$$\xi = f_{w2}\left(- L\frac{\varepsilon}{k}\widetilde{P} + M\frac{\overline{\varepsilon}^2}{k} - N\frac{\varepsilon\,\widetilde{\varepsilon}}{k}\right) \quad , \tag{12}$$

where $f_{w2} = exp\left[-(Re_t/40)^2\right]$ is a damping function to insure the disappearance of the effects of ξ far away from a wall, and L, M, and N are model constants. Subsequent calculations show that these constants should take on values given by $L = 2.25$, $M = 0.5$ and $N = 0.57$. The modified $\overline{\varepsilon} = \varepsilon - 2\nu k/y^2$ is introduced to ensure proper behavior of ε near a wall. Thus modeled, (3) and (4) are valid as a wall is approached and can be used to calculate wall bounded flows where the boundary conditions on $-\overline{u_iu_j}$ and ε are given by: $-\overline{u_iu_j} = 0$ and $\varepsilon_w = 2\nu\left(\partial\sqrt{k}/\partial y\right)^2$. The usual no-slip conditions at the wall are applied to the mean velocities.

Near-wall LRR/WR model

The LRR/WR near-wall model also solves (3) and (4) with the models for D^T_{ij} and ε_{ij} given by (5) and (6), respectively. The differences come in C_ε, which is assumed to take on a value of 0.1 rather than 0.12, (7), (11) and (12). LRR/WR assumes the high-Reynolds-number LRR model for Π_{ij}. Therefore, (7) is now given by

$$\Pi_{ij} = -2C_1\varepsilon\, b_{ij} - \alpha_1\left(P_{ij} - \frac{2}{3}\delta_{ij}\widetilde{P}\right) - \beta_1\left(D_{ij} - \frac{2}{3}\delta_{ij}\widetilde{P}\right) - 2\gamma_1 k\, S_{ij} + \Pi^w_{ij} \quad , \tag{13}$$

where $C_1 = 1.5$, $C_2 = 0.4$, $\alpha_1 = (8 + C_2)/11$, $\beta_1 = (8C_2 - 2)/11$, $\gamma_1 = (30C_2 - 2)/55$ and again Π^w_{ij} is the near-wall correcting function required to make the modeled equation to satisfy the wall boundary conditions exactly. According to Zhang (1993), the expression derived for Π^w_{ij} can be written as

$$\Pi^w_{ij} = f_{w1}\left[2C_1\varepsilon\, b_{ij} + \alpha^*\left(P_{ij} - \frac{2}{3}\delta_{ij}\widetilde{P}\right) - \frac{\varepsilon}{k}\left(\overline{u_iu_k}n_kn_j + \overline{u_ju_k}n_kn_i\right)\right] + 2C_wk\,S_{ij}\left(\frac{k^{3/2}}{\varepsilon\, y}\right) , \tag{14}$$

where $\alpha^* = 0.45$ and C_w is a model coefficient. The first term inside the square bracket is to account for the reflected-wall effects of the slow part, the second term that of the reflected-wall effects of the rapid part and the third term is to compensate for the pressure diffusion effects near a wall. Zhang (1993) argued that the last term was required because a similar term also existed in the original model of Launder et al. (1975) but they neglected it in its final form. The NWLLR model is also given by (13) and (14), except that the last term in (14) is set equal to zero. In other words, the reflected-wall effects are only partially accounted for by the C_1 and α^* terms inside the square bracket.

In order for this modification to work well for a wide variety of turbulent flows, Zhang (1993) found that C_w has to take on different values, while all other model constants remain unchanged. Three different expressions were found to be suitable, where C_w is specified by

$$C_w = -8.05 \, x \, 10^{-3} + 5.19 \, x \, 10^{-3} log \, Re_m \quad , \tag{15a}$$

for internal flows, it is deduced to be

$$C_w = C_{w,\,in} = 4.14 \, x \, 10^{-3} + 3.0 \, x \, 10^{-3} log \, Re_\theta \quad , \tag{15b}$$

for external flows and it is given by

$$C_w = C_{w,\,in} - 5.8 \, x \, 10^{-4} M_\infty \quad , \tag{15c}$$

for compressible flows. In (15c), $C_{w,in}$ was taken to be given by (15b) for $Re_\theta \leq 5{,}500$ and to be $C_{w,in} = 0.0153$ for $Re_\theta > 5{,}500$. Here, Re_m is the bulk Reynolds number based on the channel width or the pipe diameter, Re_θ is the Reynolds number based on the momentum thickness, M_∞ is the free stream Mach number and the damping function $f_{w1} = exp\left[-(Re_t / 150)^2\right]$ is specified by Zhang (1993). This damping function was found to work well for all the incompressible and compressible flow cases attempted by Zhang (1993), except the near-separating flow of Samuel and Joubert (1974). In order to make the model work for adverse pressure gradient flows, it was found necessary to modify the damping function by introducing a dependence on a pressure gradient parameter. Zhang (1993) proposed a modified damping function f_{w1} given by

$$f_{w1} = exp\left[-\left\{Re_t/150\left(1 + 0.13\beta_c\right)\right\}^2\right] \quad , \tag{16}$$

where β_c is the Clauser parameter defined as $\beta_c = \left(\delta^*/\tau_w\right)\left(d P_\infty/dx\right)$. Here, x is the stream coordinate, δ^* is the displacement thickness of the boundary layer, τ_w is the wall shear stress and P_∞ is the free stream pressure. Finally, (12) is derived to be the same, except that the model constants now take on the following values, $L = 2.25$, $M = 1.5$ and $N = 2.0$, while the same f_{w2} is assumed. In other words, both C_w and f_{w1} become problem dependent. Thus modified, the model again gives good results for the near-separating flow case.

Two-equation k-ε model

A two-equation k-ε model can also be obtained from (3) and (4) by contracting (3) and dividing it over by 2 to yield the k-equation. If the terms resulted from the anisotropic near-wall corrections are neglected as suggested by Lai and So (1990), the k equation can be written as

$$\frac{Dk}{Dt} = \frac{\partial}{\partial x_i}\left[\left(\nu + \frac{\nu_t}{\sigma_k}\right)\frac{\partial k}{\partial x_i}\right] + \widetilde{P} - \varepsilon \quad , \tag{17}$$

where $\sigma_k = 1$ is assumed, ν_t is the eddy viscosity and is defined as

$$\nu_t = C_\mu f_\mu \frac{k^2}{\varepsilon} \quad . \tag{18}$$

In (18), C_μ is a model constant taken to be 0.096 and f_μ is a damping function introduced to ensure asymptotic correctness for the behavior of the Reynolds shear stress near a wall. For the present k-ε model, f_μ is given by

$$f_\mu = \left[1 + \frac{3.45}{\sqrt{Re_t}}\right] tanh\left(\frac{y^+}{115}\right) \quad . \tag{19}$$

It should be pointed out that the turbulent diffusion coefficient in (4) should be replaced by $\nu_t / \sigma_\varepsilon$ where σ_ε is a model constant taken to be 1.45.

The two-equation model assumes gradient transport and isotropic eddy viscosity. Therefore, it is not that suitable for complex flows which are know to give rise to anisotropic turbulence behavior. In order to capture this particular feature without resorting to a full Reynolds-stress model, the anisotropic eddy viscosity proposal of Speziale (1987) could be adopted. According to Speziale (1987), the anisotropic eddy viscosity is given by

$$
\begin{aligned}
\overline{u_i u_j} &= \frac{2}{3} k\, \delta_{ij} - 2 C_\mu f_\mu \frac{k^2}{\varepsilon} S_{ij} \\
&\quad - 4\, C_D\, C_\mu^2 f_\mu^2 \frac{k^3}{\varepsilon^2} \left(S_{ik}\, S_{kj} - \frac{1}{3} S_{kl}\, S_{kl}\, \delta_{ij} + \widetilde{S}_{ij} - \frac{1}{3} \widetilde{S}_{kk}\, \delta_{ij} \right) \quad , \qquad (20)
\end{aligned}
$$

where $\widetilde{S}_{ij} = \left(\frac{\partial S_{ij}}{\partial t} + U_k \frac{\partial S_{ij}}{\partial x_k} - \frac{\partial U_i}{\partial x_k} S_{kj} - \frac{\partial U_j}{\partial x_k} S_{ki} \right)$ is the frame-indifferent Oldroyd derivative of S_{ij} and C_D is a dimensionless constant that assumes a value of 1.68. It should be pointed out that the isotropic eddy viscosity formulation is recovered in the limit of C_D goes to zero. Therefore, the above anisotropic eddy viscosity model along with the k and ε equations can be used to predict complex turbulent flows; there is no need to solve the full set of Reynolds-stress equations. The two-equation models are included here for the sake of completeness. In this report, only the calculations of the near-wall Reynolds-stress model are discussed. Two-equation assessment with respect to Couette flows has been carried out by So and Sarkar (1994); other validations will be addressed in a different report.

Modeled equations for compressible flows

The extension to compressible flows is quite straight forward if Morkovin's (1962) hypothesis is invoked and the equations are written in terms of Favre-averaging, much like what Zhang et al. (1993a, b) have done in extending the k-ε and the LRR/WR model to compressible flows. For compressible turbulence, it has been suggested by Sarkar et al. (1991) that the dissipation rate ε could be decomposed into a solenoidal part and a compressible part so that $\varepsilon = \varepsilon_s + \varepsilon_c$. The solenoidal dissipation rate is associated with the energy cascade, therefore, it approaches the incompressible limit correctly. In view of this and consistent with Morkovin's hypothesis (1962), the compressible part of ε is neglected in the present formulation and ε is taken to be given by ε_s alone. Therefore, from this point on, the symbol ε is taken to either mean the true dissipation rate in incompressible flow or the solenoidal part of the true dissipation rate in compressible flows. With these simplifications, the modeled equations are very similar to those given in (3) and (4) and the incompressible models can be directly extended to compressible flows. Therefore, the compressible modeled equations, including the mean flow equations, are given below without derivation.

A density-weighted average is used to decompose the fluctuating quantities, besides pressure and density, into a mass-weighted mean part and a mass-weighted fluctuating part. On the other hand, the pressure and density are decomposed using Reynolds average, which results in a time-averaged mean part and a time-averaged fluctuating part. For any variable F, the mass-weighted mean is denoted by $\widetilde{F}$, the mass-weighted fluctuating part by f, the time-averaged mean by $\overline{F}$ and the time-averaged fluctuating part by f'. The fluid density is taken to be ρ, the dynamic viscosity μ, the thermal conductivity k_t, the specific heat at constant pressure C_p, and the gas constant is denoted by R. In terms of these variables, the pressure p and the temperature Θ, the mean equations of motions for compressible turbulence can be written as:

$$\frac{\partial\overline{\rho}}{\partial t} + \left(\overline{\rho}\,\widetilde{U}_i\right)_{,i} = 0 \quad , \tag{21}$$

$$\frac{\partial\overline{\rho}\,\widetilde{U}_i}{\partial t} + \left(\overline{\rho}\,\widetilde{U}_i\,\widetilde{U}_j\right)_{,j} = -\overline{P}_{,i} - \frac{2}{3}\left(\overline{\mu}\,\widetilde{U}_{j,j}\right)_{,i} + \left[\overline{\mu}\left(\widetilde{U}_{i,j} + \widetilde{U}_{j,i}\right)\right]_{,j} - \left(\overline{\rho}\,\tau_{ij}\right)_{,j} \quad , \tag{22}$$

$$\begin{aligned}\frac{\partial\overline{\rho}\,\overline{C}_p\widetilde{\Theta}}{\partial t} + \left(\overline{\rho}\,\widetilde{U}_i\,\overline{C}_p\widetilde{\Theta}\right)_{,i} = {} & \frac{\partial\overline{P}}{\partial t} - \widetilde{U}_i\,\overline{P}_{,i} + \overline{u}_i\,\overline{P}_{,i} + \overline{u_i'\,p_{,i}'} + \overline{\sigma}_{ij}\,\widetilde{U}_{i,j} \\ & + \overline{\sigma}_{ij}\,\overline{u}_{i,j} + \overline{\rho}\,\varepsilon - \left(\overline{\rho}\,\overline{C}_pQ_i\right)_{,i} + \left(\overline{k}_t\,\widetilde{\Theta}_{,i}\right)_{,i} \quad ,\end{aligned} \tag{23}$$

$$\overline{P} = \overline{\rho}\,R\,\widetilde{\Theta} \quad , \tag{24}$$

where $(\cdot)_{,i}$ denotes a gradient with respect to the spatial coordinate x_i, the Einstein summation convention applies to repeated indices, and the Reynolds stress tensor, the Reynolds heat flux vector, the turbulent dissipation rate are defined as $\tau_{ij} = \widetilde{u_iu_j}$, $Q_i = \widetilde{u_i\theta}$, $\overline{\rho}\,\varepsilon = \overline{\sigma_{ij}'\,u_{ij}'}$, respectively. The mean viscous stress tensor is given by:

$$\overline{\sigma}_{ij} = -\frac{2}{3}\,\overline{\mu}\,\widetilde{U}_{k,k}\,\delta_{ij} + \overline{\mu}\left(\widetilde{U}_{i,j} + \widetilde{U}_{j,i}\right) \quad . \tag{25}$$

When deriving these equations, additional assumptions are made regarding the neglect of turbulent fluctuations of dynamic viscosity, thermal conductivity and specific heat. Also, according to Speziale and Sarkar (1991), the velocity-pressure gradient correlation term $\overline{u_i' p_{,i}'}$ can be written in the equivalent form as

$$\overline{u_i' p_{,i}'} = -\left(\bar{\rho} R \tilde{\Theta} \bar{u}_i\right)_{,i} + \left(\bar{\rho} R \widetilde{u_i\theta}\right)_{,i} - \overline{p' u_{i,i}'} \tag{26}$$

From these equations, it can be seen that, to achieve closure, models are required for the Reynolds stress tensor τ_{ij}, the Reynolds heat flux vector Q_i, the pressure dilatation correlation $\overline{p' u_{i,i}'}$, the turbulent dissipation rate ε and the mass flux vector $\bar{u}_i$. In the following, a near-wall Reynolds-stress model based on the incompressible model derived above is given for τ_{ij}, and ε, while Morkovin's hypothesis (1962) is invoked to justify the neglect of $\overline{p' u_{i,i}'}$ and $\bar{u}_i$ in the modeling of supersonic turbulent flows and a constant turbulent Prandtl number, $Pr_t = 0.9$, is assumed for the evaluation of Q_i , or $- Q_i = - \widetilde{u_i\theta} = (\nu_t / Pr_t)\left(\partial\tilde{\Theta} / \partial x_i\right)$ where ν_t is the eddy viscosity defined in (18) with the damping function given in (19).

The compressible Reynolds-stress equation written in the same form as its incompressible counterpart is given by:

$$\frac{\partial}{\partial t}(\bar{\rho}\tau_{ij}) + \left(\tilde{U}_k\bar{\rho}\tau_{ij}\right)_{,k} = \left(\overline{u_i'\sigma_{jk}'} + \overline{u_j'\sigma_{ki}'}\right)_{,k} + C_{ijk,k} + \left(-\bar{\rho}\tau_{ik}\tilde{U}_{j,k} - \bar{\rho}\tau_{jk}\tilde{U}_{i,k}\right)$$

$$+ \Pi_{ij} - \varepsilon_{ij} + \left(\frac{2}{3}\overline{p' u_{k,k}'}\,\delta_{ij}\right) - \left(\bar{u}_i P_{,j} + \bar{u}_j P_{,i}\right) + \left(\bar{u}_i\bar{\sigma}_{jk,k} + \bar{u}_j\bar{\sigma}_{ik,k}\right) \quad , \tag{27}$$

where

$$C_{ijk,k} = -\left(\bar{\rho}\widetilde{u_i u_j u_k} + \frac{2}{3}\overline{p' u_k'}\,\delta_{ij}\right)_{,k} \quad , \tag{27a}$$

$$\Pi_{ij} = -\left(\overline{u_i' p_{,j}'} + \overline{u_j' p_{,i}'}\right) + \frac{2}{3}\overline{u_k' p_{,k}'}\,\delta_{ij} \quad , \tag{27b}$$

$$\varepsilon_{ij} = \overline{\sigma_{ik}' u_{j,k}'} + \overline{\sigma_{jk}' u_{i,k}'} \quad , \tag{27c}$$

are the turbulent diffusion tensor of τ_{ij}, the velocity-pressure gradient correlation tensor and the viscous dissipation rate tensor of τ_{ij}, respectively. The last three bracketed terms in (27) arise as a result of compressibility and are identically zero for incompressible flows. Therefore, if Morkovin's hypothesis (1962) is invoked, the last three bracketed terms in (27) can be neglected and the turbulent diffusion, viscous dissipation and velocity-pressure gradient correlation terms can be modeled as in constant-density flows. Consistent with this assumption, the term $\overline{p'u'_{i,i}}$ in (26) is also neglected. Finally, the viscous diffusion term $\left(\overline{u_i'\sigma_{jk}'} + \overline{u_j'\sigma_{ik}'}\right)_{,k}$ is approximated by $\left(\bar{\mu}\tau_{ij,k}\right)_{,k}$. Thus simplified, (27) can be closed by adopting the near-wall models outlined above. It is sufficient to write down the equations based on the near-wall SSG model, the corresponding equations for the LRR/WR model can be easily deduced and are also given by Zhang (1993). Without derivation, the models for the various terms can be generalized as:

$$C_{ijk,k} = \left[C_s \bar{\rho}\frac{k}{\varepsilon}\left(\tau_{kl}\tau_{ij,l} + \tau_{jl}\tau_{ki,l} + \tau_{il}\tau_{jk,l}\right)\right]_{,k} \quad , \tag{28}$$

$$\Pi_{ij} = \Pi_{ij}^{*} + \Pi_{ij}^{w} \quad , \tag{29}$$

$$\varepsilon_{ij} = \frac{2}{3}\bar{\rho}\,\varepsilon\,\delta_{ij} + \varepsilon_{ij}^{w} \quad . \tag{30}$$

Here, Π_{ij}^{*} is given by the high-Reynolds-number model of Speziale et al. (1991), Π_{ij}^{w} and ε_{ij}^{w} are near-wall corrections. The models for these different terms can now be written for compressible flows as:

$$\begin{aligned}\Pi_{ij}^{*} = &-\left(2C_1\varepsilon + C_1^{*}\widetilde{P}\right)b_{ij} + C_2\varepsilon\left(b_{ik}b_{kj} - \frac{1}{3}\Pi\,\delta_{ij}\right) - \alpha_1\left(P_{ij} - \frac{2}{3}\widetilde{P}\,\delta_{ij}\right)\\ &- \beta_1\left(D_{ij} - \frac{2}{3}\widetilde{P}\,\delta_{ij}\right) - 2\left(\gamma_1 + \frac{C_3^{*}}{2}\Pi^{1/2}\right)k\,S_{ij} \quad ,\end{aligned} \tag{31}$$

$$\begin{aligned}\Pi_{ij}^{w} = f_{w1}&\left[\left(2C_1\varepsilon + C_1^{*}\widetilde{P}\right)b_{ij} - C_2\varepsilon\left(b_{ik}b_{kj} - \frac{1}{3}\Pi\,\delta_{ij}\right)\right.\\ &\left. + \alpha^{*}\left(P_{ij} - \frac{2}{3}\widetilde{P}\,\delta_{ij}\right) + 2\gamma^{*}k\,S_{ij}\right] + \Pi_{ij}^{P} \quad ,\end{aligned} \tag{32}$$

$$\Pi_{ij}^{P} = -\frac{1}{3}\left[\frac{\partial}{\partial x_l}\left(\bar{\mu}\frac{\partial\overline{u_i\,u_k}}{\partial x_l}\right)n_k n_j + \frac{\partial}{\partial x_l}\left(\bar{\mu}\frac{\partial\overline{u_j\,u_k}}{\partial x_l}\right)n_k n_i\right] + \frac{1}{3}\frac{\partial}{\partial x_m}\left(\bar{\mu}\frac{\partial\overline{u_k u_l}}{\partial x_m}\right)n_k n_l n_i\,n_j \quad , \tag{33}$$

$$\varepsilon_{ij}^{w} = f_{w1}\left[-\frac{2}{3}\bar{\rho}\varepsilon\,\delta_{ij} + \bar{\rho}\frac{\varepsilon}{k}\frac{\left(\tau_{ij} + \tau_{ik}n_k n_j + \tau_{jk}n_k n_i + n_i n_j\tau_{kl}n_k n_l\right)}{\left(1 + 3\tau_{kl}n_k n_l/2k\right)}\right] \quad , \tag{34}$$

where $P_{ij} = -\left(\bar{\rho}\,\tau_{ik}\tilde{U}_{j,k} + \bar{\rho}\,\tau_{jk}\tilde{U}_{i,k}\right)$ represents turbulence production of the Reynolds stresses, $k = \tau_{ii}/2$ is the turbulent kinetic energy, b_{ij} is the anisotropic tensor and is again given by (8a), $\tilde{P} = P_{ii}/2$, $S_{ij} = \left(\tilde{U}_{i,j} + \tilde{U}_{j,i}\right)/2$ and $D_{ij} = -\left(\bar{\rho}\,\tau_{ik}\tilde{U}_{k,j} + \bar{\rho}\,\tau_{jk}\tilde{U}_{k,i}\right)$. The damping function is again defined by (11a) and (11b) depending on the Reynolds number of the flow, while the turbulent Reynolds number is given by $Re_t = k^2/\bar{\nu}\,\varepsilon$.

The dissipation rate ε is assumed to be approximately equal to the solenoidal dissipation rate whose modeled equation, similar to its incompressible counterpart, can be written for compressible flows as:

$$\frac{\partial\bar{\rho}\,\varepsilon}{\partial t} + \left(\bar{\rho}\,\varepsilon\,\tilde{U}_k\right)_{,k} = \left(\bar{\mu}\,\varepsilon_{,k}\right)_{,k} + \left(C_\varepsilon\bar{\rho}\frac{k}{\varepsilon}\tau_{ki}\,\varepsilon_{,i}\right)_{,k} + C_{\varepsilon 1}\frac{\varepsilon}{k}\tilde{P} - C_{\varepsilon 2}\frac{\bar{\rho}\varepsilon\,\tilde{\varepsilon}}{k} + \xi \quad . \qquad (35)$$

The near-wall correcting function ξ can be generalized for compressible flows to give

$$\xi = f_{w2}\,\bar{\rho}\left(-L\frac{\varepsilon}{k}\tilde{P} + M\frac{\bar{\varepsilon}^2}{k} - N\frac{\varepsilon\tilde{\varepsilon}}{k}\right) \quad . \qquad (36)$$

In (36), $\hat{\varepsilon}$ and $\bar{\varepsilon}$ are defined by $\bar{\rho}\,\tilde{\varepsilon} = \bar{\rho}\,\varepsilon - 2\bar{\mu}\left(\partial\sqrt{k}/\partial x_2\right)^2$ and $\bar{\rho}\,\bar{\varepsilon} = \bar{\rho}\,\varepsilon - 2\bar{\mu}\,k/x_2^2$, respectively, and the damping function is given by $f_{w2} = exp\left[-(Re_t/40)^2\right]$. The model constants are all taken to be the same as those given above for the near-wall SSG model. Finally, the boundary conditions for the mean and turbulent velocity field are given by:

$$\tilde{U}_i = k = \tau_{ij} = 0; \quad \varepsilon = 2\,\bar{\nu}_w\left(\partial\sqrt{k}/\partial x_2\right)^2 \quad , \qquad (37)$$

where x_2 is the wall normal coordinate.

IV. Validations Against Simple Turbulent Flows

Three different types of simple turbulent flows are considered. These are fully-developed channel and Couette flows, fully-developed pipe flows and flat plate boundary-layer flows. The internal flow Reynolds numbers considered range from a low of $Re_\tau = 170$ to a high of $Re_\tau = 8758$. This corresponds to a bulk Reynolds number of about 5,600 to 500,000. As for the boundary-layer flows, the Reynolds number is calculated based on the momentum thickness and free stream velocity or $Re_\theta = U_\infty \theta / \nu$. The range covered varies from 1,410 to 7,800. The data include both measurements and DNS data obtained from numerical simulation. Most of the data in the low Reynolds number range are DNS experiments, while all of the high Reynolds number flows are selected from experimental measurements. Therefore, the simple flows invesigated vary from very low to very high Reynolds numbers and detailed near-wall DNS data are available for comparisons. All these flows are calculated using the Present model and the LRR/WR model outlined in Section III. Their ability to replicate these flows is analysed and discussed below.

Whenever possible, comparisons are made by plotting the results in the form of U^+ versus ln y^+, $k^+ = k/u_\tau^2$ versus y^+, $uv^+ = \overline{uv}/u_\tau^2$ versus y^+, $\varepsilon^+ = \nu\varepsilon/u_\tau^4$ versus y^+ and u', v' w' versus y^+. In the case of boundary-layer flows, some figures are plotted versus y/δ, where δ is the boundary layer thickness. Here, u, v and w are the fluctuating velocity components along the axial or x, the normal or y and the transverse or z directions, respectively; the prime is used to denote the rms value of these fluctuations and the overbar is used to represent time-averaged quantities. Detailed comparisons are made with the data whenever possible. Since ε^+ distributions are not always available from the data sets chosen, the plots of ε^+ are merely to show the difference between various model predictions and to illustrate the ability of the models to calculate a maximum ε^+ at the wall. In addition, the ability of the models to correctly predict the von Karman constant, κ, is assessed.

Besides comparing the mean and turbulence properties across the channel, the near-wall asymptotes of k, $\overline{uv}$, ε, u', v' and w' are calculated in order to analyze their asymptotic consistency. According to So et al. (1991), k^+, uv^+, ε^+, u', v' and w' near a wall can be expanded in terms of y^+ as

$$k^+ = a_k y^{+2} + b_k y^{+3} + \ldots\ldots, \tag{38a}$$

$$uv^+ = a_{uv} y^{+3} + b_{uv} y^{+4} + \ldots\ldots, \tag{38b}$$

$$\varepsilon^+ = 2a_k + 4b_k y^+ + \ldots\ldots, \tag{38c}$$

$$u' = a_u y^+ + b_u y^{+2} + \ldots\ldots, \tag{38d}$$

$$v' = a_v y^{+2} + b_v y^{+3} + \ldots\ldots, \tag{38e}$$

$$w' = a_w y^+ + b_w y^{+2} + \ldots\ldots, \tag{38f}$$

where the a_i's and b_i's are coefficients in the expansions for k^+, uv^+, u', v' and w'. Therefore, the ratio $k^+/\varepsilon^+ y^{+2}$ is exactly 1/2 at the wall and $\left(a_u^2 + a_v^2 + a_w^2\right)/a_k = 2$. In all previous calculations using the LRR/WR model (Zhang 1993), the ratios $k^+/\varepsilon^+ y^{+2} = 1/2$ and $\left(a_u^2 + a_v^2 + a_w^2\right)/a_k = 2$ are recovered correctly. This means that the LRR/WR model is internally consistent and asymptotically correct for incompressible internal and external flows as well as for incompressible boundary-layer flows. Therefore, any deviation from these values is an indication of the inadequacy of the near-wall model.

Channel and Couette flows

The governing equations for fully-developed channel and Couette flows can either be reduced to ordinary differential equations or time dependent one-dimensional equations, therefore, they can be solved by a number of simple numerical methods. Two standard ones are the time marching technique used by So and Sarkar (1994) and the Newton iteration method used by Lai and So (1990). These two techniques are used to solve the governing equations for channel and Couette flows and they are found to give essentially the same results. Therefore, it is immaterial as to which method is used to obtain the results shown below for channel and Couette flows. Calculations are carried out for the DNS channel flow data of Kim et al. (1987) and Kim (1991) at $Re_\tau = 180$ and 395, respectively, for the DNS Couette flow data of Lee and Kim (1991) at $Re_\tau =$

170 and for the combined channel/Couette flow experiments of El Telbany and Reynolds (1980, 1981) at Re_τ ranging from 625 to 1,463. In these latter experiments, three sample flows are selected for calculations. They are the channel flow ($\gamma = 1$), the Couette flow ($\gamma = -1$) and a mixed channel/Couette flow ($\gamma = 0.504$). Since the highest Re_τ attempted in these calculations is only 1,463, the number of grid points required for grid independent results is found to be 54. The grid points are distributed so that at least 5 points are in the region bounded by $0 < y^+ < 10$, 15 to 25 points in the region $10 < y^+ < 100$, and about 25 points in the rest of the flow region.

The calculated results are summarized in Figs. 4 - 11. Each figure gives five plots plus one table that compares the calculated κ and near-wall asymptotes with data, whenever possible. The von Karman constant is determined by following the procedure outlined by So et al. (1994). In this procedure, an overlap between the inner layer and the outer layer is first determined from the DNS data set or from measurements. A straight line is then drawn through the overlap in semi-log plot and the slope of the straight line yields κ. Once the overlap is identified for a particular flow case, an identical region is used to determine κ from the model calculations of the same flow case. This way, the von Karman constant is determined consistently and differences shown between model calculations and data are true discrepancies. However, it should be pointed out that this way of determining κ gives rise to an error of ± 0.02 for a nominal $\kappa = 0.41$. The DNS channel flow comparisons are given in Figs. 4 - 7, the DNS Couette flow results are shown in Figs. 8 and 9, while the combined channel/Couette flow calculations are plotted in Figs. 10 and 11. For each flow case, the results of the Present model are shown first. It is then followed by the results of the LRR/WR model.

The LRR/WR model assumes (15a) for C_w and this gives rise to the results shown in Figs. 5, 7, 9 and 11 for channel and Couette flows. These results are very similar to those obtained using the Present model (Figs. 4, 6, 8 and 10). The κ thus determined for all the flow cases considered varies between 0.38 and 0.4, compared to about 0.4 obtained from the data. The worst prediction of κ is given by the LRR/WR calculation for the case of channel flow with $Re_\tau = 180$ (Table 5). Even then, the error is only about 7.5% which is low compared to some of the predictions reported by So et al. (1991b) for the same flow case. The predictions of the normal stresses are also in good agreement with measurements (see the $\gamma = 1$ case in Figs. 10 and 11), even when the flow is a mixed channel/Couette flow ($\gamma = 0.504$ case in Figs. 10 and 11), except in the near-wall region where the stress anisotropy is not repropduced correctly. It seems that the LRR/WR model does a better job of predicting the stress anisotropy in the very near-wall region, $y^+ < 10$, compared to the Present model. However, its prediction of the stress anisotropy in the region $y^+ > 50$ is not as good as the Present model. This behavior is, in general, true for all the flow cases calculated in this study. As for the predictions of the near-wall asymptotes, both models give essentially the same results. The asymptotic values $k^+/\varepsilon^+ y^{+2} = 1/2$ and $\left(a_u^2 + a_v^2 + a_w^2\right) / a_k = 2$ are recovered correctly for all the cases shown here, while the calculated a_k's are in good agreement with data. In general, the channel flow calculations show that the Present model is just as good as the LRR/WR model, which relies on a C_w that varies parametrically with Re_m to give good predictions. However, it should be pointed out that the use of (15a) to calculate developing channel or Couette flow could present a problem for the LRR/WR model. More will be said about this crucial point in Section VI.

It has been argued for quite some time that conventional high-Reynolds-number turbulence models are not suitable for calculating plane Couette flows (Henry and Reynolds 1984). According to Schneider (1989), the reason for this can be attributed to the erroneous prediction of the spatial distributions of k across the channel even when second-order and third-order closures are used. A typical prediction gives a fairly uniform k across the channel; most models fail to capture the rise to a maximum near the wall. Recently, Nisizima and Yoshizawa (1987) proposed an anisotropic near-wall k-ε model while Schneider (1989) suggested the modeling of the anisotropic behavior of the pressure diffusion term in a high-Reynolds-number Reynolds-stress model for the calculation of plane Couette flows. Their argument is that the lack of anisotropy in conventional models is the main source of an incorrect k prediction in plane Couette flow calculations. However, their models are not asymptotically consistent in the near-wall region and their results again show that the model calculations of k, contrary to DNS data and measurements, still greatly under-predict the rise of k in the near-wall region. In another study on Couette flows, So and Sarkar (1994) hypothesised that, if the modeled equations behave similarly to the exact equations as a wall is approached, the predictions of the near-wall flow would be asymptotically correct and this, in turn, would give rise to a much better estimate of the outer flow. In other words, previous erroneous predictions of plane Couette flows are the result of incorrect modeling of the near-wall flow. So and Sarkar's (1994) calculations of the DNS Couette flow of Lee and Kim (1991) fully support their hypothesis. The Present model and the LRR/WR model do not attempt to mimick the pressure diffusion behavior near a wall but are asymptotically correct. Therefore, good predictions of Couette flows are expected based on the hypothesis of So and Sarkar (1994). Indeed, this is the case as can be seen in the results shown in Figs. 8 - 11. The rise of k near the wall is predicted by both models; however, the quantitative agreement is not as good. This is due to an under-prediction of u', while the predictions of v' and w' are in good agreement with measurements (see Figs 10 and 11). The true reason for the discrepancy noted in the u' prediction may not be due to model inadequacy, but rather to the existence of roll cells in the flow. In their paper, So and Sarkar (1994) gave a detailed discussion of the under-prediction of k near the channel core. In view of this, it can be said that the Present model and the LRR/WR model give equally good predictions of channel and Couette flows over a wide range of Reynolds numbers.

Pipe flows

This set of flow cases are selected to test the models' ability to replicate Reynolds number effects over a very wide range of Reynolds numbers. Four data sets are selected; they are the measurements of Durst et al. (1993) at $Re_\tau = 250$, the experiment of Schildknecht et al. (1979) at $Re_\tau = 489$, and the measurements of Laufer (1954) at $Re_\tau = 1052$ and 8758. In terms of the bulk Reynolds numbers, they vary from a low of 7,500 to a high of 500,000. Thus, the Reynolds number attempted is the highest among the many test cases investigated by various researchers. In view of the high Reynolds numbers attempted, the number of grid points required for grid independent results is found to be 108. For the two lowest Reynolds numbers, only a grid with 54 points is sufficient while at $Re_\tau = 8758$, a grid with 250 points is required. These results are essentially identical to those obtained using 108 grid points. Therefore, in the following presentation, the results for the three lower Reynolds numbers are obtained with 108 grid points, while the results for the highest Reynolds number case is obtained using 250 grid points. Again, the plots are presented in a manner similar to those shown in Figs. 4 - 11. The calculations of the Present model are shown first and this is followed by the comparisons of the LRR/WR model. Comparisons of the model calculations with the four different pipe flow measurements are presented in Figs. 12 - 19.

As the Reynolds number increases, the viscous layer becomes thinner and thinner. Therefore, the viscous dissipation rate approaches zero faster. If the Reynolds number effects are modeled correctly, the calculations should reflect this trend both qualitatively and quantitatively. An examination of the results shown in Figs. 12 - 19 reveal that this trend is being reproduced correctly by both models. At $Re_\tau = 250$, ε^+ approaches zero at the pipe center. As the Reynolds number increases, the location where Re_τ goes to zero moves towards the pipe wall and, at $Re_\tau = 8758$, ε^+ vanishes at a distance very close to the pipe wall, or at $(1 - r/R) = 0.15$. The comparisons show that the predictions of ε^+ is in good agreement with measurements whenever they are available from the experiments. Again, the asymptotic values of $k^+/\varepsilon^+ y^{+2}$ and $\left(a_u^2 + a_v^2 + a_w^2\right) / a_k$ are calculated correctly; thus indicating that the models are asymmptotically correct for pipe flows as well as for channel and Couette flows.

In general, the log-law is reproduced by the two models for the four flow cases examined. The models also give a very good prediction for κ (see Tables 12 to 19) Again, the largest error is given by the LRR/WR prediction of the $Re_\tau = 250$ case. Besides this, there are other slight differences in the model predictions. One of which is the prediction of the k distribution. Both models over-estimate the value of k in the pipe core and under-predict k in the near-wall region for the $Re_\tau = 8758$ case (see Figs. 18 and 19). However, the LRR/WR model consistently gives a larger error than the Present model. Also, the LRR/WR prediction of k is very much in error at

$Re_\tau = 250$ (compared Fig 12 with Fig. 13). Both models replicate the maximum k and the location where the maximum occurs correctly. Together, these results show that the two models examined are quite comparable in their predictive capabilities. However, in the case of the Present model, none of the model constants has to be altered over this wide range of Reynolds numbers investigated. On the other hand, C_w has to take on different values depending on the flow Reynolds numbers for the LRR/WR model. More will be said about this in Sections V and VI.

Flat plate boundary-layer flows

Three different boundary-layer flows covering a Re_θ range of 1,410 to 7,800 are selected to test the models' ability to replicate simple external flows. These consist of the DNS data of Spalart (1988) at $Re_\theta = 1{,}410$, the detailed measurements of Karlsson and Johansson (1988) at $Re_\theta = 2{,}420$ and the measurements of Klebanoff (1954) at $Re_\theta = 7{,}800$. The boundary layer calculations are carried out using the computer code of Anderson and Lewis (1971). Suitable modifications are made to the code and to the grid distributions in order to accommodate the two near-wall Reynolds-stress models. All calculations are found to be grid independent when they are carried out with 101 grid points or more. The comparisons are made in the region where the flow has achieved fully-developed turbulence. Thus, inlet boundary condition effects are essentially absent in all the results presented in Figs. 20 - 25. Unlike internal fully-developed flow calculations where Re_τ is specified, the boundary-layer calculations are carried out by inputting U_e, the free stream velocity. Consequently, the wall shear stress, τ_w, is a calculated result rather than an input. The accuracy in which this quantity, or the skin friction coefficient $C_f = 2\tau_w / \rho U_e^2$, can be calculated is an indication of the predictive capability of the models. Therefore, in addition to comparing κ, the calculated and measured C_f's are also compared. These quantities together with the near-wall asymptotes are given in Tables 20 - 25.

In this range of Reynolds numbers, the use of (11a) for f_{w1} is applicable for the Present model and there is no need to switch over to (11b) even at the lowest Reynolds number examined. On the other hand, C_w changes from case to case according to (15b) for the LRR/WR model.

Even then, there are quite a number of differences between the two model predictions of these three boundary-layer flows. The differences are summaried below. At low Reynolds numbers, the Present model gives a better prediction of the flow than the LRR/WR model. This is obvious by comparing Figs. 20 and 21. LRR/WR under-predicts the k distribution in the near-wall region and yields a κ with about 17% error compared to the DNS data (compared values in Tables 20 and 21). Also, LRR/WR gives a lower value for ε^+ at the wall compared to the Present model prediction and DNS data. On the other hand, the Present model under-estimates the stress anisotropy in the near-wall region compared to the LRR/WR model. The predictions of the LRR/WR model are much closer to the DNS data. As the Reynolds number increases, the predictions of k by the LRR/WR model improve and essentially become identical with those given by the Present model. It is not clear why LRR/WR over-predicts the shear stress distribution across the boundary layer for the $Re_\theta = 2{,}420$ case (Fig. 23). Other than that, the overall predictions of the LRR/WR model are the same as the Present model. For the highest Reynolds number case, $Re_\theta = 7{,}800$, both models under-estimate k in the near-wall region (Figs. 24 and 25), much like the predicted behavior shown in the pipe flow case where the bulk Reynolds number is 500, 000. In general, the prediction of κ improves as the Reynolds number increases and the associated progressive thinning of the viscous layer is being reproduced correctly by the two models. Based on these results, it can be said that the Present model is every bit as good as the LRR/WR model, except that there is no adjustable constant like C_w used in the LRR/WR model.

V. Validations Against Simple Compressible Turbulent Flows

The next set of validations are carried out with simple compressible turbulent flows and is intended to test the ability of the models to replicate the effects of compressibility under the assumption of Morkovin's hypothesis. With this assumption, compressibility effects are accounted for by the variation of mean density alone and the governing mean flow and Reynolds-stress equations can be reduced to forms similar to their incompressible counterparts. Consequently, the incompressible models can be extended to compressible flows without modifications. In the process, the effects of compressible dissipation and dilatation are neglected. Again, the boundary-layer code of Anderson and Lewis (1971) is modified for the present calculations. The boundary layer is calculated to the same Re_θ as the experiments where comparisons with measurements are carried out. Therefore, the results are relatively free of the effects of inlet conditions, except for the case with the lowest Re_θ. Since there are few turbulence data in these experiments, the comparisons are made with the measured mean velocity, mean temperature and C_f only. It should be pointed out that, in compressible boundary layers over adiabatic walls, the mean temperature profiles are not measured separately. Rather, they are interpreted from the mean velocity profiles by assuming the total enthalpy across the boundary layer to be constant. As a result, the temperature comparisons are not very meaningful for the flow cases with an adiabatic wall. From the measured mean velocity profiles, the von Karman constant can be determined depending on whether the mean velocities are reduced in the standard way (So et al. 1994) or by invoking the van Driest (1951) transformation. Two von Karman constant are deduced and they shall be denoted as κ and κ_c for the standard way and the van Driest transformation, respectively.

According to So et al. (1994), the standard law of the wall for compressible boundary layers can be deduced by invoking Morkovin's (1962) hypothesis, the dimensional arguments of Millikan (1939) and the assumption of an overlap between the inner and outer layers. The result is given by

$$U^+ = \frac{1}{\kappa(M_\tau, B_q, \gamma)} \ln y_w^+ + B(B_q, M_\tau, \gamma, Pr_w) \quad , \tag{39}$$

where $u_\tau = (\tau_w / \rho_w)^{1/2}$, $y_w^+ = y\, u_\tau / \nu_w$, $B_q = Q_{tot} / \left(\rho_w C_p u_\tau \tilde{\Theta}_w\right)$, $M_\tau = u_\tau / a_w$, $Pr_w = (C_p \mu_w) / k_w$, a_w is the sound speed evaluated at the wall, and $\gamma = C_p / C_v$ is the ratio of the specific heats evaluated at the wall. Here, the suscript w is used to denote values evaluated at the wall, Q_{tot} is the total heat transfer rate and k_w is the fluid thermal conductivity evaluated at the wall. The von Karman constant κ is parametric in M_τ, B_q and γ while the intercept is not only parametric in these variables but also the Prandtl number evaluated at the wall, Pr_w. On the other hand, according to van Driest (1951), the law of the wall for compressible boundary layers can be written as

$$\frac{U_c}{u_\tau} = \frac{1}{\kappa_o} \ln y_w^+ + B \quad , \tag{40a}$$

where

$$U_c = \int_0^U \left(\frac{\rho}{\rho_w}\right)^{1/2} d\,U \quad . \tag{40b}$$

Here, κ_c is the corresponding von Karman constant and U_c is the transformed mean velocity according to (40b). In (40a), again B is the intercept; however, unlike B in (39), its parametric dependence is not entirely clear. The determination of κ and κ_c are compared in Table 26 where, in addition, the measured and calculated C_f's are compared.

Altogether six different flow cases are selected to test the models. These are the heated wall case of Spina and Smits (1987) where $M_\infty = 2.87$ and $\tilde{\Theta}_w / \Theta_{aw} = 1.10$, the adiabatic wall cases collected in Fernholz and Finley (1977) where $M_\infty = 2.24, 4.54, 10.31$ and $\tilde{\Theta}_w / \Theta_{aw} = 1.0$, the slightly cooled wall case documented in Fernholz and Finley (1977) where $M_\infty = 5.29$ and $\tilde{\Theta}_w / \Theta_{aw} = 0.92$ and the high Mach number, highly cooled wall case of Kussoy and Horstman (1991) where $M_\infty = 8.18$ and $\tilde{\Theta}_w / \Theta_{aw} = 0.30$. Here, Θ_{aw} is the adiabatic wall temperature. The results of the model calculations and comparisons are shown in Figs. 26 - 37, while a summary of the measured and calculated C_f, κ and κ_c are given in Table 26. Only four plots are given in each figure. They are the standard law of the wall plot, the linear plot of the mean velocity, the van Driest law of the wall plot and the linear plot of the mean temperature. In the linear plots, the mean velocity or mean temperature is plotted versus y / δ_r, where δ_r is the boundary-layer thickness determined either from the measurements or from the calculations. Again, the Present model calculations are given first and this is followed by the LRR/WR predictions of the same flow case. In the following, the heated wall, adiabatic wall and cooled wall cases are discussed separately.

Boundary layers over a heated wall

The measured and calculated profiles are shown in Figs. 26 and 27, while the C_f, κ and κ_c are compared in Table 26. It can be seen that both models give essentially the same results when plotted in semi-log plots even though the Present model slightly over-estimate the mean velocity in the outer part of the boundary layer. As far as the prediction of C_f is concerned, both models give results that are within 5% of the measured C_f. The Present model's prediction of the mean temperature is in error. This could be due to the fact that a constant Pr_t is assumed. The same is not true of the LRR/WR model because of the used of C_w which was empirically made to be parametric in both Re_θ and M_∞ according to (15c). This empirical input could partially compensate for the constant Pr_t assumption. According to Sommer et al. (1992), the turbulent Prandtl number is not constant even for incomopressible flow with heat transfer where the temperature difference is of the order of 20°C. Therefore, there is no good reason to expect the constant Pr_t assumption to be completely valid in this case. Sommer et al. (1993, 1994) have applied their incompressible variable turbulent Prandtl number model (Sommer et al. 1992) to calculate compressible flows using a two-equation model as well as a Reynolds-stress model and slightly improved agreement with measurements were obtained compared to those given by the constant Pr_t assumption. Perhaps, improved results could also be obtained if the model of Sommer et al. (1992) is used to model the turbulent heat flux. In terms of κ and κ_c, the agreement between calculations and measurements is fairly good and, for this low Mach number, κ and κ_c are determined to be essentially the same. Their values are different from 0.41 though; κ is more like 0.51 while κ_c is approximately 0.37 (Table 26). This means that van Driest law of the wall is not quite applicable even for a compressible flow over a slightly heated wall at fairly low free stream Mach numbers.

Furthermore, the asymptotic values of k^+/ε^+y^{+2} and $\left(a_u^2 + a_v^2 + a_w^2\right)/a_k$ are calculated correctly; again indicating that the models are asymptotically correct even for compressible flows.

Boundary layers over an adiabatic wall

Three cases, ranging in M_∞ from 2.24 to 10.31, are calculated using the Present model and the LRR/WR model. Unlike the heated wall case, where $Re_\theta = 83{,}899$, the Reynolds numbers at the location where measurements are available vary from a low of 5,320 to a high of 20,797. These values are listed in Table 26. Therefore, there might be some Reynolds number effects in the model calculations for the case where $Re_\theta = 5{,}320$. The comparisons between model calculations and measurements are given in Figs. 28 - 33, where Figs. 28 and 29 show the comparisons for the $M_\infty = 2.24$ case, Figs. 30 and 31 those of the $M_\infty = 4.54$ case, and finally Figs. 32 and 33 the comparisons for the $M_\infty = 10.31$ case. Calculated C_f, κ and κ_c are again listed in Table 26 for comparisons with measurements.

At low Mach number ($M_\infty = 2.24$), the model calculations are essentially identical and the κ and κ_c thus determined are about the same. The calculated C_f is slightly different; the LRR/WR model result being 4.3% higher than measurement while the Present model only over-estimates by 1.8%. As a result, the semi-log plots of the Present model calculations of the mean velocity are in slightly better agreement with measurements. Since the mean temperature is deduced from the mean velocity, good agreement in the mean velocity comparison also implies the same for the mean temperature (Figs. 28 and 29). Also, the wall temperature is calculated correctly by both models (Figs. 28d and 29d). The LRR/WR model over-predicts C_f by about 4.7% while the Present model under-estimates by the same percentage in the $M_\infty = 4.54$ case. Therefore, in the semi-log plots of the mean velocities, the calculations of the Present model lie above the measurements while those of the LRR/WR model lie below the measurements (Figs. 30 and 31). When the velocities are shown in the linear plot form, good agreement with data is obtained. At this Mach number, there is some difference between the standard law of the wall plot and the van Driest law of the wall plot. The κ_c determined from measurements deviates from 0.41 significantly once the Mach number reaches 4.54. Its value for the high Mach number cases is more like 0.29 rather than 0.41. On the other hand, a $\kappa = 0.41$ is obtained from the standard law of the wall plot of the same measurements up to a Mach number of 4.54. At the highest Mach number tested, $\kappa = 0.54$ is obtained, thus showing its dependence on the Mach number. The calculated von Karman constants are in good agreement with these values (Table 26).

At the highest Mach number tested, the semi-log plots of the Present model calculations are not in good agreement with measurements compared with the LRR/WR results (Figs. 32 and 33). This is due mainly to an under-estimation of C_f which is in error by about 17%, while there is no error in the LRR/WR prediction. When the comparisons are made in the linear plots, the calculations correlate very well with measurements. These errors could be attributed to the neglect of compressible terms in the modeled equations and the assumptions of Morkovin's hypothesis and constant turbulent Prandtl number. Since the turbulent Prandtl number is known to increase sharply as a wall is approached (Sommer et al. 1993), the incorrect estimate of C_f by the Present model could be partially attributed to the constant Pr_t assumption. Therefore, an improvement to the prediction of C_f could be obtained by relaxing this assumption. The reason why the LRR/WR model gives a good prediction of C_f could be due to the empirical input in the form of C_w which decreases as M_∞ increases. In other words, the contributions of the term kS_{ij} to Π_{ij}^{w} in (14) are being minimized. At this Mach number, κ_c is significantly different from 0.41. Consequently, the data points do not follow the van Driest law of the wall. On the other hand, the standard law of the wall with a κ parametric in M_τ can still be used to correlate the mean velocity. The κ thus determined is substantially larger than 0.41 (Table 26). Based on these comparisons, it can be said that the van Driest law of the wall is perhaps most valid for compressible flows over an adiabatic wall with low to medium Mach numbers.

Boundary layers over a cooled wall

Two flow cases are selected to test the models and they are the slightly cooled wall case documented in Fernholz and Finley (1977) with $M_\infty = 5.29$ and $\tilde{\Theta}_w / \Theta_{aw} = 0.92$ and the highly cooled wall case of Kussoy and Horstman (1991) with $M_\infty = 8.18$ and $\tilde{\Theta}_w / \Theta_{aw} = 0.30$. The two cases cover medium to high Mach numbers and near adiabatic wall to highly cooled wall boundary conditions. In general, the model calculations of LRR/WR are more accurate in terms of the calculated C_f. LRR/WR under-estimates C_f slightly while the Present model under-predicts C_f as much as 14% in the $M_\infty = 5.29$ case. In view of this, the semi-log plots of the mean velocity lie above the measured data for the $M_\infty = 5.29$ case (Fig. 34) and below the measured data for the $M_\infty = 8.18$ case (Fig. 36). Again, the mean velocities in linear plots are in good agreement with measurements. Perhaps, relaxing the assumption of a constant turbulent Prandtl number could improve the prediction of C_f. The good agreement shown between LRR/WR model results and measurements could be attributed to the empirical function (15c) used to evaluate C_w.

Again, the κ_c determined from the measurements deviate significantly from 0.41 (Table 26). Even at $\tilde{\Theta}_w / \Theta_{aw} = 0.92$, κ_c is found to be about 0.34. In other words, the van Driest law of the wall cannot suitably describe the log-law region if κ_c is taken to be 0.41. The standard law of the wall shows that κ is also dependent on the total heat flux, hence it should vary as the wall temperature ratio decreases. Both the data and the calculations show that κ is indeed decreasing as the Mach number increases and the wall temperature ratio decreases. The errors in the predicted κ is larger than the other cases but this could be due to the assumption of a constant turbulent Prandtl number which is more applicable to flows over an adiabatic wall than to flows over a cooled wall.

Concluding remarks

Altogether, these results show that van Driest law of the wall is essentially valid for compressible flows over an adiabatic wall with fairly low free stream Mach numbers. Even then, κ_c is found to be about 0.38 rather than 0.41. Only a slight wall cooling is sufficient to change κ_c to a value that is substantially smaller than 0.41. On the other hand, κ is determined to be 0.41 from the standard law of the wall plots for compressible flows over an adiabatic wall up to a free stream Mach number of 4.54. Therefore, it would seem that the standard law of the wall would be just as valid when used to describe compressible flows. As predicted by (38), κ is parametric in

M_τ, B_q and γ. The present analysis shows that this is indeed the case. This is also true for κ_c. The behavior of κ and κ_c with M_∞ and $\widetilde{\Theta}_w / \Theta_{aw}$ is reproduced fairly well by both models. For the LRR/WR model, this is accomplished at the expense of making C_w a function of Re_θ and M_∞; thus rendering the model rather ad hoc. On the other hand, the predictive capability of the Present model is achieved without having to alter any of the model constants, but rather by choosing an alternate high-Reynolds-number pressure strain model where the reflected-wall effects are accounted for properly in the model. Therefore, the Present model is less ad hoc and more physical. Finally, it should be pointed out that the LRR/WR model has also been applied to calculate flows over compression ramp with and without shocks by Morrison et al. (1993) and fair agreement with measurements were obtained. Since there are no structural differences between the LRR/WR and the Present model, one would expect the Present model could just as easily implemented into the code of Morrison et al. (1993) to calculate compression ramp flows with and without shocks.

VI. Validations Against Complex Turbulent Flows

In the previous two sections, simple flows are calculated. As a result, standard numerical algorithms such as the Newton iteration scheme (Lai and So 1990) and the two-dimensional parabolic finite-difference code (Anderson and Lewis 1971) can be used to solve the governing equations and the models present little or no numerical stability problems for the calculations of these flows. On the other hand, complex flow calculations require the use of more advanced numerical algorithms and the implementation of these models into the codes could cause numerical instability in the computation. Therefore, the objectives of this section are two fold; one to validate the models for complex flows and another to test the ease with which the models can be implemented into advanced numerical algorithms without giving rise to undue numerical instability.

Three different types of complex flows are selected to test the model's ability to predict them. The first is a flow with an adverse pressure gradient that leads to incipient separation (Samuel and Joubert 1974). Therefore, the ability of the models to mimick near separating flow correctly is assessed by this comparison. A second case is a fully-developed flow in a square duct at a bulk Reynolds number of 50,000 (Lund 1977; Eppich 1982). This flow tests the models' ability to replicate the turbulence driven secondary cells in the cross-stream plane of the duct. The third case is an axially rotating pipe flow (Kikuyama et al. 1983). In this flow, a superimposed vortex that eventually develops into a solid-body rotation is present and alters the developing nature of the pipe flow. Therefore, the models' ability to reproduce the rotational behavior of complex turbulent flows is borne out by this assessment.

Near separating flows

The adverse pressure gradient flow is carried out using the boundary-layer program of Anderson and Lewis (1971). Calculations start in the region where the pressure gradient is zero and carry forward until Re_θ reaches a value equal to that reported by Samuel and Joubert (1974) at the start of the adverse pressure gradient. This location is then taken to be the origin of the axial, or x, location of the experiment. The measured free stream velocity distribution, $U_e(x)$, is prescribed as the external boundary condition for U while the zero gradient condition is specified for all other variables. At the wall, the boundary conditions are as discussed in Section III. As before, 101 grid points are found to be sufficient to give grid independent results. Furthermore, slight mismatch in Re_θ at the entrance to the adverse pressure gradient region has been investigated and the results show that there are insignificant or no differences in the calculated development of C_f and Re_θ. Consequently, the model calculations are not carried out at exactly the same Re_θ.

Three different calculations are carried out; one using the Present model, another the LRR/WR model while a third invokes the LRR/WR model but with β_c or the constant associated with β_c set equal to zero in (16). The results of these calculations at two x locations are summarized in Figs. 38 - 40 with the mean velocity and shear stress comparisons of the Present model shown first (Fig. 38) and this is followed by the LRR/WR comparisons (Fig. 39). Finally, the calculated development of C_f and Re_θ are compared in Figs. 40a and 40b while a sample mean velocity result of the LRR/WR model with β_c set equal to zero in (16) is shown in Fig. 40c. The two x-locations, x = 2.87m and 3.4m, are chosen to be very near separation in order to evaluate the models' ability to replicate near separating flows.

At x = 2.87m, both the Present model and the LRR/WR model give essentially the same predictions (compared Figs 38 and 39) with the von Karman constant κ determined to be 0.43 and 0.42, respectively. This compares with $\kappa = 0.42$ determined from the measurements. The agreement between the Present model and data deteriorates as the flow moves near separation and, at x = 3.4m, the Present model under-predicts the mean velocity in the region near the wall while the C_f is calculated correctly (Fig. 40a). As a result, the velocity calculations of the Present model in semi-log plot lie below those of measurements (Fig. 38c) and $\kappa = 0.46$ is obtained compared to an experimental value of 0.43. Taking the error bound in the determination of κ into consideration, it can be said that the Present model calculations of κ are in fair agreement with measurements. On the other hand, there is no such deterioration in agreement for the LRR/WR model (Fig. 39c) and the von Karman constant is evaluated to be $\kappa = 0.41$. As for the prediction of the shear stress distributions at the two x locations, both models give essentially the same results

(Figs 38e, f and 39e, f). The Present model under-predicts the shear stress in the outer region and this under-prediction deteriorates as separation is approached; the behavior is consistent with the mean velocity prediction shown in Figs. 38c and 38d. The deterioration noted in the prediction of the LRR/WR model is not as severe, even though the LRR/WR model calculation of C_f is slightly under the measured value starting at x = 2.87m and continues to deteriorate as the flow moves near separation. Therefore, the modification specified in (16) seems to improve the prediction of U but not that of C_f. Without the modification in (16), the LRR/WR model under-predicts U and over-estimates C_f substantially (Fig. 40a) and this leads to a wrong calculation of the velocity profile across the boundary layer and a $\kappa = 0.48$ (Fig. 40c). Finally, the Present model under-predicts the development of Re_θ compared to that given by the LRR/WR model (Fig. 40b). However, this slight under-prediction does not seem to have much of an effect on the calculation of C_f though (Fig. 40a).

It is obvious that (16) helps to improve the predictive capabilities of the LRR/WR model. Therefore, if a similar expression is also implemented into the Present model, better predictions than those shown in Fig. 38 could be expected. It can be easily shown that the coefficient of the y^{+2} term in the mean velocity expansion near a wall is dependent on the streamwise pressure gradient. Therefore, one could argue that the modeled equations should some how depend on the streamwise pressure gradient and hence justify the use of (16). A plot of the damping function (16) from the LRR/WR calculations indicates that f_{w1} vanishes in the range, $55 < y^+ < 100$ depending on the streamwise pressure gradient. On the other hand, (16) without the β_c term from the third model calculations yields a f_{w1} that goes to zero very near the wall. When (11a) from the Present model calculations is plotted, it gives a curve that approaches zero somewhere between the two former curves. This suggests that near-wall damping has a significant effect on the prediction of the mean velocity. In other words, the damping functions proposed in (11) are not quite general eneough. The proper approach is to seek another damping function where it will again approach zero in the proper range of y^+ for flows with and without severe adverse pressure gradient effects. The ad hoc modifications suggested in (16) may not be appropriate because it explicitly depends on

β_c. In conclusion, the deficiency is not in the SSG model, but rather in the proposed damping function for the near-wall corrections.

Square duct flows

Fully-developed turbulent flow in a square duct is two-dimensional, therefore, it can be solved by iterating in the cross-stream plane alone. However, in anticipation of the need to calculate developing flows later, a three-dimensional TEACH-type code is used to solve the governing equations in the square duct. Since the flow is symmetrical about the wall bisectors, only a quadrant of the flow needs to be considered. A non-uniform grid is used to calculate the flow in this quadrant. An iterative forward marching solution procedure is used to solve the parabolized equations. In particular, the three-dimensional parabolic finite difference procedure of Patankar and Spalding (1972) is employed. The convergence rate is improved by implementing the SIMPLEC algorithm (van Doormal and Raithby 1984) into the code rather than using the original SIMPLE algorithm (Patankar 1980). The boundary conditions are specified as follows. Symmetry conditions are specified along the wall bisectors. At the walls, all the mean velocity components and the Reynolds stresses are set equal to zero , while the dissipation rate is specified as $\varepsilon_w = 2\nu\left(\partial\sqrt{k} / \partial x_2\right)^2$. At the inlet, essentially all variables are specified to be uniform except near the wall. Near the wall, all variables are given as obtained from the results of a boundary layer code at a specified boundary layer thickness of approximately 1 percent of the duct width.

Special attention is given to the placement of grids near the wall. A minimum of 5 grids are placed within $y^+ < 5$ with the first grid point at approximately $y^+ = 1$, and 15-25 grids are located in the region $5 < y^+ < 100$, depending on the total number of grids used. Calculations with 81x81, 121x121 and 161x161 grids have been carried out. The reason that such fine grids are required is due to the presence of secondary cells which are absent in the case of pipe flows with and without rotation. There are no significant differences between the calculations obtained with the 121x121 and 161x161 grids. Therefore, only the results from the 121x121 grids are presented here. The forward step size is varied progressively from 0.4 percent of the hydraulic diameter near the inlet to

4 percent until the flow becomes fully developed. The iterations are carried out to normalized residual sources of 10^{-5} for each variable. Finally, it should be pointed out that the use of (15a) for C_w failed to yield a convergent solution for the square duct flow. Instead, (15b) has to be specified and Re_θ at each x location has to be evaluated to determine if $Re_\theta < 5{,}500$. Once Re_θ has reached 5,500, $C_w = 0.0153$ is assumed. This procedure is found to work for flow Reynolds number as high as 250,000.

The comparisons of the Present model calculations with measurements are shown in Figs. 41 and 42 while those of the LRR/WR model are given in Figs. 43 and 44. Whenever possible, the results are compared with measurements along the wall bisector as well as along the angle bisector. Along the wall bisector, the normalized ordinate is given by y/a, where a is the half-width of the square duct. The normalized ordinate along the angle bisector is denoted by y'/a', where $a' = a\sqrt{2}$. All velocity results are made dimensionless by the mean bulk velocity U_b. The axial velocity is given by U while the secondary velocity by W. Among the results presented are the mean velocities, the shear stress, $\overline{uv}$, the normal stresses, the turbulent kinetic energy and the wall shear along the horizontal wall, z. On comparisons, it can be seen that both models give about the same predictions of the square duct flow. The mean U along both the wall and angle bisectors correlates well with measurements while the calculated Reynolds stresses are in error. In general, the calculations along the wall bisector are in better agreement with the measurements compared to those along the angle bisector, where the turbulence statistics are over-predicted. Both models cannot replicate the secondary velocity very well even though the LRR/WR model gives a slightly better prediction than the Present model. This under-prediction of the secondary motion has also been observed by Gessner and Emery (1981) and Demuren and Rodi (1984) and is found to be quite common among the high-Reynolds number Reyolds-stress models tested.

Rotating pipe flows

The two-dimensional elliptic code of Yoo et al. (1991) is used to calculate the rotating pipe flow experiments of Kikuyama et al. (1983). Three cases are reported and they are designated by

$Ro = 0, 0.5$ and 0.83, where Ro is the rotation number defined as the ratio of the pipe circumferential velocity to the bulk mean velocity. In this report, only the case where $Ro = 0.5$ is calculated and discussed. As a check on the code, the $Ro = 0$ case is calculated first and this is equivalent to calculating developing pipe flow without swirl. Two different boundary conditions at 100 diameters downstream of the inlet are specified; one is fully-developed flow at the outlet and another is to assume the neglect of axial diffusion compared to radial diffusion. The appropriateness of each specification is examined and the right choice made for the rotating pipe flow calculations. Furthermore, the calculation of this simple case allows the question of grid distribution to be investigated, the number of grid points required to be studied, and the best way to implement the near-wall Reynolds-stress model to be explored. Since the fully-developed flow calculations have been reported in detail above, there is no need to present this set of results again. It is sufficient to point out that the iterations are carried out until the normalized residual sources reduce to 10^{-5} for each variable. Therefore, the calculations obtained from both outlet boundary conditions are in very good agreement with measurements and the results are essentially grid independent when there are 56 grids in the r-direction and 51 grids in the x-direction. The grid distribution in the r-direction follows closely that used to perform the fully-developed flow calculations presented above. That is, 25 grids are placed within the region, $0 < y^+ < 100$. In the x-direction, the grids are closely spaced near the pipe entrance. As the flow develops, the grids are spaced further and further apart. When the flow is approaching the fully-developed state, a spacing of several pipe diameters is not unusual. The same experiment has also been attempted by Yoo et al. (1991) using a different near-wall Reynolds-stress model. Their conclusions on grid spacing and grid distribution are consistent with the present findings.

Since only measurements in the developing region were reported and the locations where they were made were far apart, only sample comparisons of the present model calculations at one x/D location are presented in Figs. 45 and 46. When the LRR/WR model is applied to calculate the $Ro = 0.5$ case, the use of (15a) for C_w failed to yield a solution but the use of (15b) yielded a convergent solution. In this calculation, C_w is estimated according to (15b) up to $C_w = 0.0153$;

thereafter $C_w = 0.0153$ is assumed. Therefore, this implies that (15a), which was developed based on two-dimensional internal flows, is not suitable for developing internal flows because (15b) also has to be assumed in the square duct flow calculation. This is an indication that the LRR/WR model is not as general as the Present model.

The comparisons shown in Figs. 45 and 46 are between the Present model, the LRR/WR model and measurements. Mean velocities are given first, followed by the shear stresses and then the normal stresses in these figures. As before, the prime (') is used to denote root mean square quantities. The mean velocities are normalized by U_0, the pipe centerline velocity, and $W_0 = R\Omega$, the pipe circumferential velocity, respectively, while the Reynolds stresses are made dimensionless by U_0. Here, Ω is the speed of rotation of the pipe and R is the pipe radius. The results show that the mean velocities are very well predicted by the Present model. This means that the boundary layer thickness and the boundary layer development along the pipe are well replicated. On the other hand, the LRR/WR model under-predicts the boundary-layer development. This is also evident from the comparisons shown for the Reynolds stresses. The normal stresses are reasonably well calculated; however, the shear stresses, particularly the $\overline{uw}$ component, are poorly predicted. In general, the shear stresses are significantly over-predicted. There are many reasons for these discrepancies. One of which could be that the accuracy of the shear stress measurements is not as good as that for the normal stresses, because the shear stresses are at least one order of magnitude smaller than the normal stresses. On the other hand, the good agreement between calculations and measurements of the normal stresses indicates that the models are replicating the anisotropic behavior of the turbulence statistics quite well for the rotating pipe flow investigated. In view of these results, both models can be said to be quite valid for rotating turbulent flows. However, the good agreement of the LRR/WR model is achieved by the added empiricism introduced in the form of (15b) for C_w, while the Present model needs no modifications for any of the model constants.

Concluding remarks

In general, the Present model replicates the complex flows quite well and these include flow complexities introduced by adverse pressure gradients, turbulence driven secondary motions and flow rotation in the form of an imposed vortex. Even though the results are not as good as the LRR/WR model in the case of near separating flow, it can be said that the LRR/WR model achieves the good correlation by introducing added empiricism in the forms of (15b) and (16). Furthermore, the Present model does not need modifications for any of the complex flows and all model constants and damping functions specified in Section III remain unchanged. In calculating developing internal flows, it is not at all clear whether (15a) or (15b) should be specified for C_W in the LRR/WR model. For example, the results shown in Figs. 43 - 46 are obtained by specifying (15b) for C_W, which is meant for external flows. There is no such ambiguity for the Present model though. Therefore, there is less empiricism introduced into the Present model and, as a result, it is more general. Also, the Present model does not introduce any undue complexity in the numerical computation and no added numerical instabilities are noted in any of the flow cases examined.

VII. Conclusions

An asymptotic analysis is carried out on the modeled and the exact Reynolds-stress and dissipation rate equations. Near-wall correcting functions are proposed for these equations so that they can be integrated directly to the wall. Thus, the physical boundary conditions can be satisfied exactly and there is no need to invoke wall functions to link the properties at the first grid point to those at the wall. Specifically, the near-wall corrections are made to the pressure strain model in the Reynolds-stress equation and to the complete equation in the case of the dissipation rate equation. The near-wall corrections differ depending on the pressure strain model invoked. In the present study, the SSG model proposed by Speziale et al. (1991) for the pressure strain is adopted and near-wall corrections to this model are deduced. This near-wall Reynolds-stress model is used to calculate a wide variety of flows, including incompressible and compressible flows, simple flows, complex flows and near-separating flows. The flows selected for validation include fully-developed turbulent flows in channel and pipes, Couette flows, simple boundary-layer flows, compressible boundary-layer flows up to Mach 10, three-dimensional flow in a square duct, axially rotating pipe flow and boundary-layer flow subject to a near-separating adverse pressure gradient. Besides comparing the model calculations with measurements and DNS data, they are also compared to another set of calculations using the LRR/WR model of Zhang (1993) derived from the LRR pressure strain model of Launder et al. (1975). In this latter model, it was found necessary to make one of the model constant to be dependent on the flow Reynolds number and the free stream Mach number. Furthermore, the damping function used in the model has to be modified to depend on β_c for the calculations of flows with pressure gradient effects. However, all model constants used in the Present model are true constants and no modifications need be made to any damping function to account for pressure gradient effects. The following conclusions can be drawn based on this detailed study of the two models.

(1) This study shows that a rather general near-wall Reynolds-stress closure can be derived through the application of asymptotic analysis to the exact and modeled governing equations in the region near a wall. The resultant near-wall closure depends on the choice

of the pressure strain model. The Present model chooses the SSG model of Speziale et al. (1991) because of its demonstrated capability to correctly predict rotating homogeneous turbulent flows compared to a number of pressure strain models.

(2) The Present model and the LRR/WR model are asymptotically consistent and yield the correct values for the near-wall asymptotes; namely, $k^+/\varepsilon^+ y^{+2} = 1/2$ and $\left(a_u^2 + a_v^2 + a_w^2\right)/\,a_k = 2$. Furthermore, both models give a fairly correct prediction of the von Karman constant κ for the flows studied.

(3) The two models give equally good results in their predictions of a wide variety of incompressible flows, ranging from simple fully-developed turbulent flows to flows through square ducts and axially rotating pipes. The flow Reynolds number covered varies from a low of about 5,600 to a high of 500,000. For the Present model, this result is achieved through the use of the SSG pressure strain model only. As for the LRR/WR model, the LRR pressure strain model is used and the good predictions are obtained by changing one of the model constant and making it parametric in the flow Reynolds number. While this dependence presents little or no difficulty to the calculations of fully-developed and parabolic flows, its applications to elliptic flow calculations could become progressively difficult as the complexities of the flow increase. On the other hand, no such difficulties are encountered with the Present model.

(4) For incompressible flows with adverse pressure gradients, the Present model gives a correct prediction of C_f but not so accurate a prediction of the mean velocity. The mean velocity is under-estimated in the near-wall region. On the other hand, the LRR/WR model calculations are in good agreement with measurements. Again, this was achieved by making f_{w1} to depend on β_c. When this dependence on the pressure gradient parameter is eliminated, the LRR/WR model predictions are decidedly worse compared to the calculations of the Present model. The reason is traced to the behavior of the damping functions rather than the near-wall corrections derived based on these models. Therefore, there is a need to improve on the damping function assumed for the Present model.

(5) For compressible turbulent flow calculations, the Present model again gives correct predictions of the mean velocity and temperature over the range of Mach numbers and wall temperature ratios considered. The calculations of C_f are also correct in the low Mach number range, except for the case where the free stream Mach number is 10.31 and for the two cases where the wall is cooled. This could be attributed to the assumption of a constant turbulent Prandtl number in the formulation. On the other hand, the LRR/WR model yields uniformly good predictions for all compressible flow cases considered. This is achieved through the empirical input of one model constant which is made parametric in the flow Reynolds number and the free stream Mach number.

(6) The Present model has been used in five different numerical algorithms in the course of calculating all the test cases. They include time marching technique for the solution of hyperbolic equations, Newton iteration technique for the solution of split boundary-value problems, parabolic codes for the calculations of boundary-layer flows, two-dimensional elliptic code for the solution of axisymmetric flow problems and partially parabolic three-dimensional code for the calculations of complex internal flows. No numerical difficulties have been encountered in any one of these calculations. Therefore, the model is quite adaptable irrespective of the numerical scheme used.

(7) The Present model is less ad hoc and more general compared to the LRR/WR model because there are no adjustable constants and/or damping functions in the Present model. Since it also gives good results in all the flow cases considered, it appears to be the near-wall model of choice. As for the noted deficiencies in the calculations of compressible flows, they could be partially remedied by relaxing the constant turbulent Prandtl number assumption in the problem formulation.

(8) The Present model can account for Reynolds number effects correctly spanning a range from about 5,600 to 500,000 for internal flows as well as for external flows.

References

Anderson, E. C. and Lewis, C. H. 1971 Laminar or turbulent boundary-layer flows of perfect gases or reacting gas mixtures in chemical equilibrium. NASA CR-1893.

Demuren, A. O. and Rodi, W. 1984 Calculation of turbulence-driven secondary motion in non-circular ducts. Journal of Fluid Mechanics **140**, 189-222.

Demuren, A. O. and Sarkar, S. 1992 Perspective: systematic study of Reynolds stress closure models in the computations of plane channel flows. Journal of Fluids Engineering **115**, 5-12, 1993.

Durst, F., Jovanovic, J. and Sender, J. 1993 Detailed measurements of the near wall region of turbulent pipe flows. Proceedings of the 9th Symposium on Turbulent Shear Flows, Kyoto, Japan, Paper No. 2.2.

El Telbany, M. M. M. and Reynolds, A. J. 1980 Velocity distribution in plane turbulent channel flows. Journal of Fluid Mechanics **100**, 1-29.

El Telbany, M. M. M. and Reynolds, A. J. 1981 Turbulence in plane channel flows. Journal of Fluid Mechanics **111**, 283-318.

Eppich, H. M. 1982 An experimental investigation of the turbulence structure in the inner region of a three-dimensional streamwise corner flow. MS thesis, Department of Mechanical Engineering, University of Washington, Seattle, WA.

Fernholz, H. H. and Finley, P. J. 1977 A critical compilation of compressible turbulent boundary layer data. AGARDograph No. 223.

Fu, S., Launder, B. E. and Tselepidakis, D. P. 1987 Accomodating the effects of high strain rates in modeling the pressure-strain correlation. Mechanical Engineering Department, UMIST, Manchester, England, Rept. TFD/87/5.

Gessner, F. B. and Emery, A. F. 1981 The numerical prediction of developing turbulent flow in rectangular ducts. Journal of Fluids Engineering **103**, 445-455.

Hanjalic, K. and Launder, B. E. 1976 Contribution towards a Reynolds-stress closure for low-Reynolds-number turbulence. Journal of Fluid Mechanics **74**, 593-610.

Henry, F. S. and Reynolds, A. J. 1984 Analytical solution of two gradient-diffusion models applied to turbulent Couette flow. Journal of Fluids Engineering **106**, 211-216.

Karlsson, R. I. and Johansson, T. G. 1988 LDV measurements of higher order moments of velocity fluctuations in a turbulent boundary layer. Laser Anemometry in Fluid Mechanics, edited by D. F. G. Durao et al., published by Ladoan - Instituto Superior Tecnico, Portugal, 273-289.

Kebede, W., Launder, B. E. and Younis, B. A. 1984 Large amplitude periodic pipe flow: a second-moment closure study. Proceedings of the 5th Symposium on Turbulent Shear Flows, Ithaca, NY, Paper No. 16.5.

Klebanoff, P. S. 1954 Characteristics of turbulence in a boundary layer with zero pressure gradient. NACA TN-1247.

Kikuyama, K., Murakami, M. and Nishibori, K. 1983 Development of three-dimensional turbulent boundary layer in an axially rotating pipe. Journal of Fluids Engineering **105**, 154-160.

Kim, J., Moin, P. and Moser, R. D. 1987 Turbulence statistics in fully developed channel flow at low Reynolds number. Journal of Fluid Mechanics **177**, 133-186.

Kim, J. 1991 Private communication.

Kussoy, M. I. and Horstman, K. C. 1991 Documentation of two- and three-dimensional shock-wave/turbulent boundary-layer interaction flows at Mach 8.18. NASA TM-103838.

Lai, Y. G. and So, R. M. C. 1990 On near-wall turbulent flow modeling. Journal of Fluid Mechanics **221**, 641-673.

Lai, Y. G., So, R. M. C., Anwer, M. and Hwang, B. C. 1991a Calculations of a Curved-Pipe Flow Using Reynolds-Stress Closures. Proceedings of the Institution of Mechanical Engineers Part C: Journal of Mechanical Engineering Science **205**, 231-244.

Lai, Y. G., So, R. M. C. and Zhang, H. S. 1991b Turbulence-Driven Secondary Flows in a Curved Pipe. Theoretical and Computational Fluid Dynamics **3**, 163-180.

Laufer, J. 1954 The structure of turbulence in fully-developed pipe flow. NACA Report 1174.

Launder, B.C., Reece, G.J. and Rodi, W. 1975 Progress in the development of a Reynolds-stress turbulence closure. Journal of Fluid Mechanics **68**, 537-566.

Launder, B. E. and Reynolds, W. C. 1983 Asymptotic near-wall stress dissipation rates in a turbulent flow. Physics of Fluids **26**, 1157-1158.

Launder, B. E. and Tselepidakis, D. P. 1988 Contribution to the second-moment modeling of sublayer turbulent transport. Zaric Memorial International Seminar on Near-Wall Turbulence, Yugoslavia, May 16-20.

Launder, B. E. and Shima, N. 1989 Second-moment closure for the near-wall sublayer: development and application. AIAA Journal **27**, 1319-1325.

Launder, B. E. and Tselepidakis, D. P. 1991 Progress and paradoxes in modeling near-wall turbulence. Proceedings of the 8th Symposium on Turbulent Shear Flows, Munich, Germany, Paper No. 29.1.

Lee, M. J. and Kim, J. 1991 The structure of turbulence in a simulated plane Couette flow. Proceedings of the 8th Turbulent Shear Flows, Technical University of Munich, Munich, Germany, Paper No. 5.3.

Lund, E. G. 1977 Mean flow and turbulence characteristics in the near corner region of a square duct. MS thesis, Department of Mechanical Engineering, University of Washington, Seattle, WA.

Lumley, J. L. 1978 Computational modeling of turbulent flows. Advances in Applied Mechanics **18**, 124-176.

Mansour, N. N., Kim, J. and Moin, P. 1988 Reynolds-stress and dissipation-rate budgets in a turbulent channel flow. Journal of Fluid Mechanics **194**, 15-44.

Millikan, C. B. 1939 A critical discussion of turbulent flow in channels and circular pipes. Proceedings of the Fifth International Congress on Applied Mechanics, Wiley, New York, pp. 386-392.

Morkovin, M. 1962 Effects of compressibility on turbulent flows. Mecanique de la Turbulence, CNRS, edited by A. Favre, published by Gordon and Breach, 367-380.

Morrison, J. H., Gatski, T. B., Sommer, T. P., Zhang, H. S. and So, R. M. C. 1993 Evaluation of a near-wall turbulent closure model in predicting compressible ramp flows. Near-Wall Turbulent Flows, edited by R. M. C. So, C. G. Speziale and B. E. Launder, published by ELSEVIER, Amsterdam, The Netherlands, 239-250.

Moser, R. D. and Moin, P. 1987 The effects of curvature in wall-bounded turbulent flows. Journal of Fluid Mechanics **175**, 479-510.

Nisizima, S. and Yoshizawa, A. 1987 Turbulent channel and Couette flows using an anisotropic k-ε model. AIAA Journal **25**, 414-420.

Patankar, S. V. and Spalding, D. B. 1972 A calculation procedure for heat, mass and momentum transfer in 3-D parabolic flows. International Journal of Heat and Mass Transfer **15**, 1787-1806.

Patankar, S. V. 1980 Numerical Heat Transfer and Fluid Flow. Published by Hemisphere, New York.

Prud'homme, M. and Elghobashi, S. 1983 Prediction of wall-bounded turbulent flows with an improved version of a Reynolds-stress model. Proceedings of the 4th Symposium on Turbulent Shear Flows, Karlsruhe, Germany, Paper No. 1.2.

Rotta, R. C. 1951 Statistische Theorie nichthomogener Turbulenz. Zeitschrift fur Physik **129**, 547-572.

Rotta, J. C. 1960 Turbulent boundary layers with heat transfer in compressible flow. AGARDograph No. 281.

Samuel, A. E. and Joubert, P. N. 1974 A Boundary layer developing in an increasingly adverse pressure gradient. Journal of Fluid Mechanics **66**, 481-505.

Sarkar, S., Erlebacher, G., Hussaini, M. Y. and Kreiss, H. O. 1991 The analysis and modeling of dilatational terms in compressible turbulence. Journal of Fluid Mechanics **227**, 473-493.

Schildknecht, M., Miller, J. A. and Meier, G. E. A. 1979 The influence of suction on the structure of turbulence in fully-developed pipe flow. Journal of Fluid Mechanics **90**, 67-107.

Schneider, W. 1989 On Reynolds stress transport in turbulent Couette flow. Z. Flugwiss. Weltraumforsch. **13**, 315-319.

Shih, T-H. and Lumley, J. L. 1985 Modeling of pressure correlation terms in Reynolds stress and scalar flux equations. Technical Report No. FDA-85-3, Cornell University, Ithaca, NY.

Shima, N. 1988 A Reynolds-stress model for near-wall and low-Reynolds-number regions. Journal of Fluids Engineering **110**, 38-44.

So, R. M. C. and Yoo, G. J. 1986 On the modeling of low-Reynolds-number turbulence. NASA CR-3994.

So, R. M. C., Lai, Y. G. and Hwang, B. C. 1991a Near-Wall turbulence closure for curved flows. AIAA Journal **29**, 1202-1213.

So, R. M. C., Lai, Y. G., Zhang, H. S. and Hwang, B. C. 1991b Second-order near-wall turbulence closures: a review. AIAA Journal **29**, 1819-1835.

So, R. M. C., Zhang, H. S. and Speziale, C. G. 1991c Near-Wall modeling of the dissipation-rate equation. AIAA Journal **29**, 2069-2076.

So, R. M. C., Zhang, H. S., Gatski, T. B. and Speziale, C. G. 1994 On logarithmic laws for compressible turbulent boundary layers. AIAA Journal, to appear.

So, R. M. C. and Sarkar, A. 1994 Turbulent Couette flows - an assessment of ten near-wall two-equation models, AIAA Journal, submitted for publication.

Sommer, T. P., So, R. M. C. and Lai, Y. G. 1992 A near-wall two-equation model for turbulent heat fluxes. International Journal of Heat and Mass Transfer **35**, 3375-3387.

Sommer, T. P., So, R. M. C. and Zhang, H. S. 1993 A near-wall variable-Prandtl-number turbulence model for compressible flows. AIAA Journal **31**, 27-35.

Sommer, T. P., So, R. M. C. and Zhang, H. S. 1994 Supersonic flow calculations using a Reynolds-stress and a thermal eddy diffusivity turbulence model. Journal of Fluids Engineering, to appear.

Spalart, P. R. 1988 Direct simulation of a turbulent boundary layer up to $R_\theta = 1410$. Journal of Fluid Mechanics **187**, 61-98.

Speziale, C. G. 1987 On nonlinear K-l and K-ε models of turbulence. Journal of Fluid Mechanics **178**, 459-475.

Speziale, C. G. and Sarkar, S. 1991 Second-order closure models for supersonic turbulent flows. AIAA Paper No. AIAA 91-0217.

Speziale, C. G., Sarkar, S. and Gatski, T. B. 1991 Modeling the pressure-strain correlation of turbulence: an invariant dynamical systems approach. Journal of Fluid Mechanics **227**, 245-272.

Speziale, C. G., Gatski, T. B. and Sarkar, S. 1992 On testing models for the pressure-strain correlation of turbulence using direct simulations. Physics of Fluids A **4**, 2887-2899.

Spina, E. F. and Smits, A. J. 1987 Organized structures in a compressible, turbulent boundary layer. Journal of Fluid Mechanics **182**, 85-109.

Tselepidakis, D. P. 1991 Development and application of a new second-moment closure for turbulent flows near walls. PhD thesis, Mechanical Engineering Department, UMIST, Manchester, England.

van Doormal, J. P. and Raithby, G. D. 1984 Enhancements of the SIMPLE method for predicting incompressible fluid flows. Numerical Heat Transfer **7**, 147-163.

van Driest, E. R. 1951 Turbulent boundary layer in compressible fluids. Journal of Aeronautical Sciences **18**, 145-160.

Yoo, G. J., So, R. M. C. and Hwang, B. C. 1991 Calculation of developing turbulent flows in a rotating pipe. Journal of Turbomachinery **113**, 34-41.

Zhang, H. S., So, R. M. C., Speziale, C. G. and Lai, Y. G. 1993a A near-wall two-equation model for compressible turbulent flows. AIAA Journal **31**, 196-199.

Zhang, H. S., So, R. M. C., Speziale, C. G. and Gatski, T. B. 1993b A near-wall second-order closure for compressible turbulent flows. Near-Wall Turbulent Flows, edited by R. M. C. So, C. G. Speziale and B. E. Launder, published by ELSEVIER, Amsterdam, The Netherlands, 209-218.

Zhang, H. S. 1993 Near-wall Reynolds-stress models for compressible flows. PhD thesis, Mechanical and Aerospace Engineering, Arizona State University, Tempe, AZ.

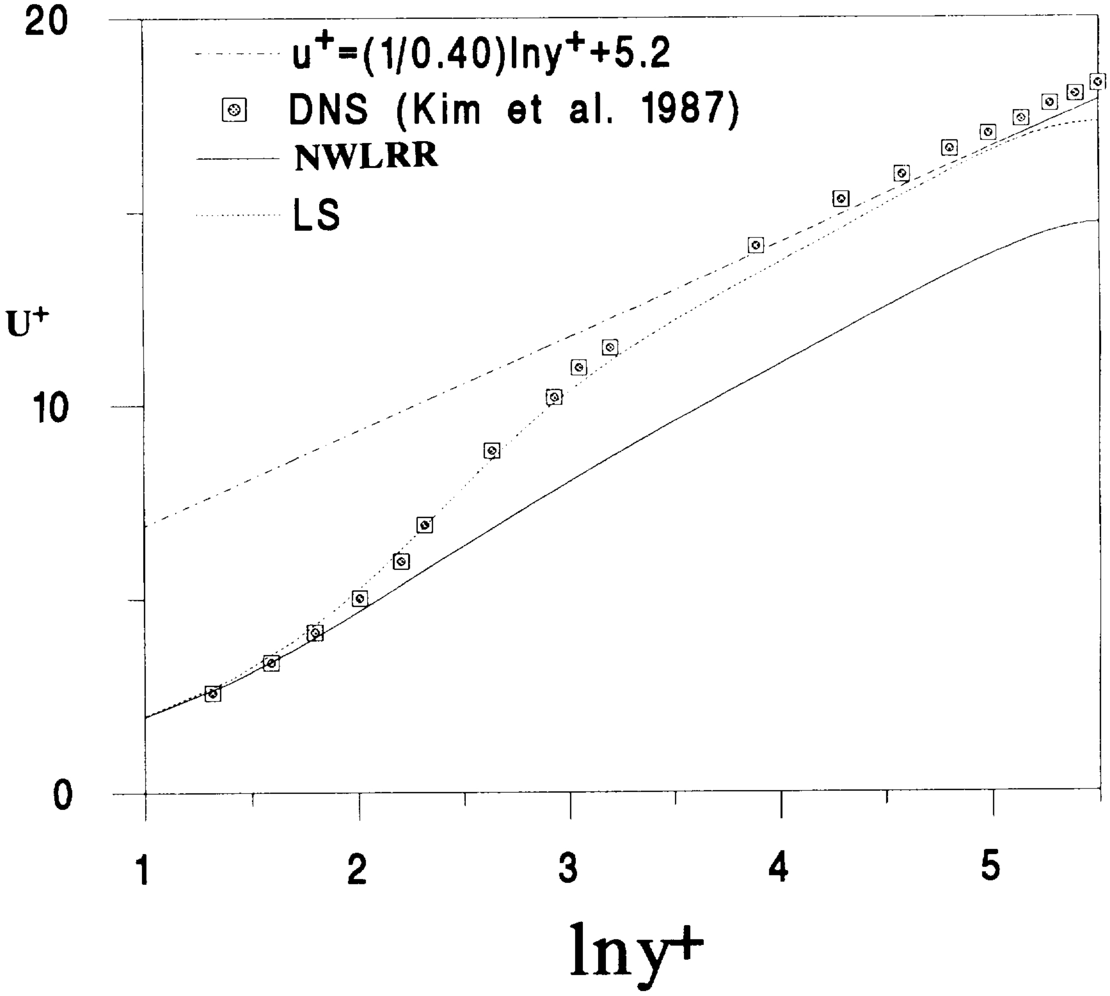

Fig. 1 Comparisons of Reynolds-stress model calculations of the mean veolcity with DNS channel flow data ($Re_\tau = 180$).

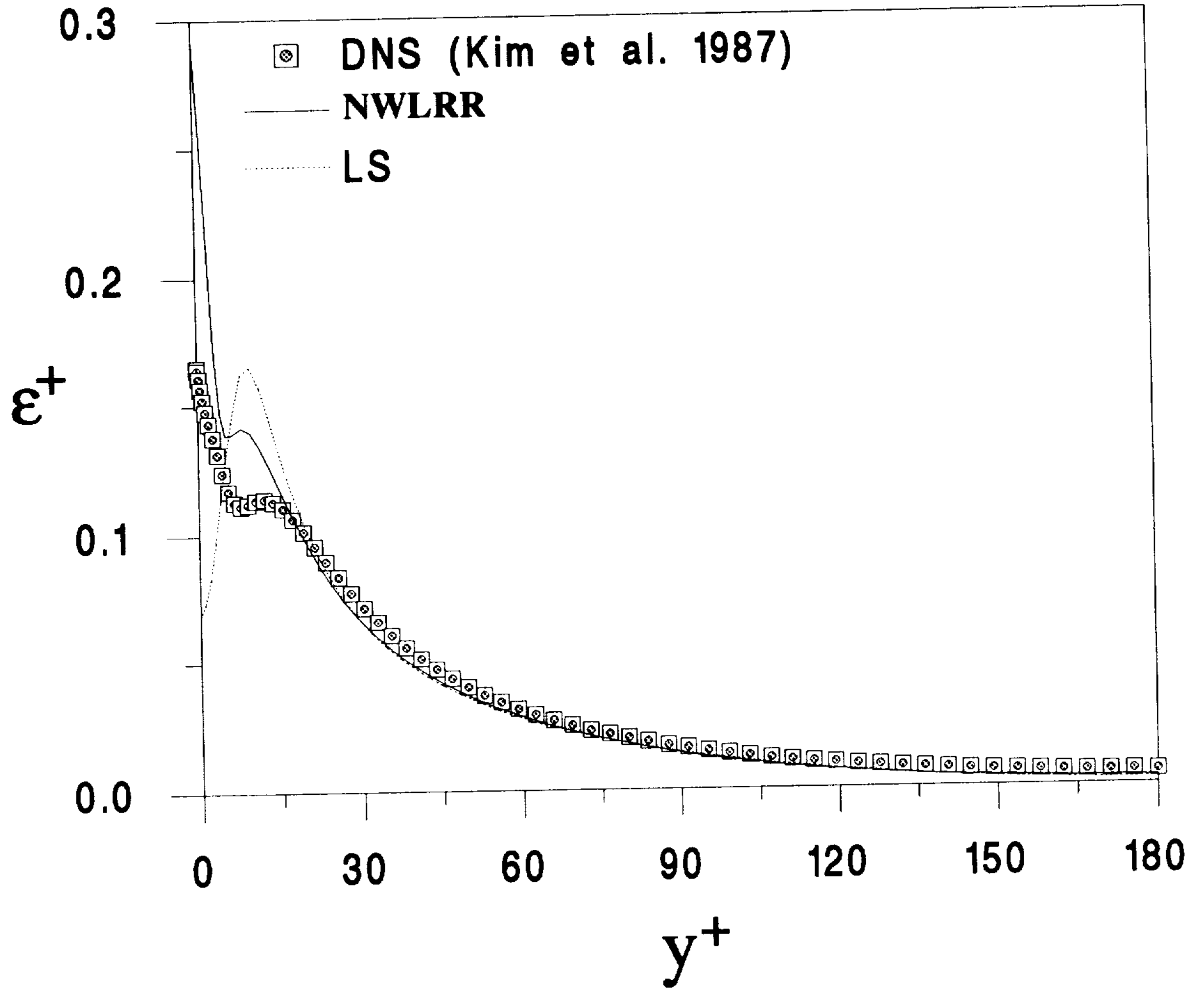

Fig. 2 Comparisons of Reynolds-stress model calculations of the dissipation rate with DNS channel flow data ($Re_\tau = 180$).

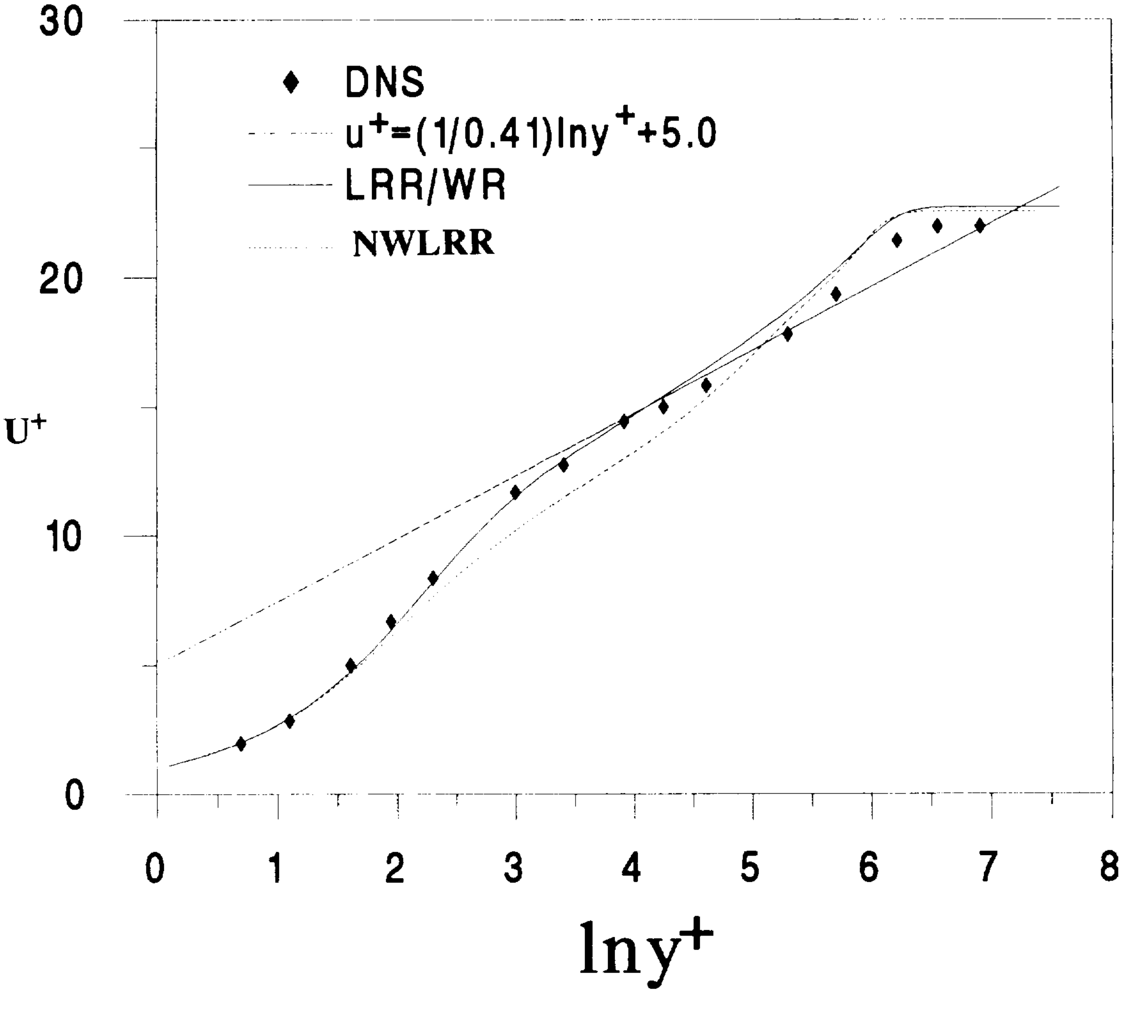

Fig. 3 Comparisons of Reynolds-stress model calculations of the mean veolcity with DNS boundary layer data ($Re_\theta = 1,410$).

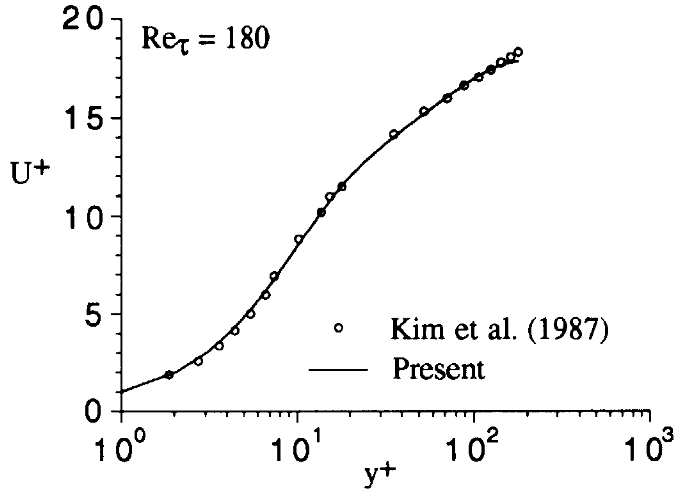

Fig. 4a Comparison of calculated U^+ with DNS data.

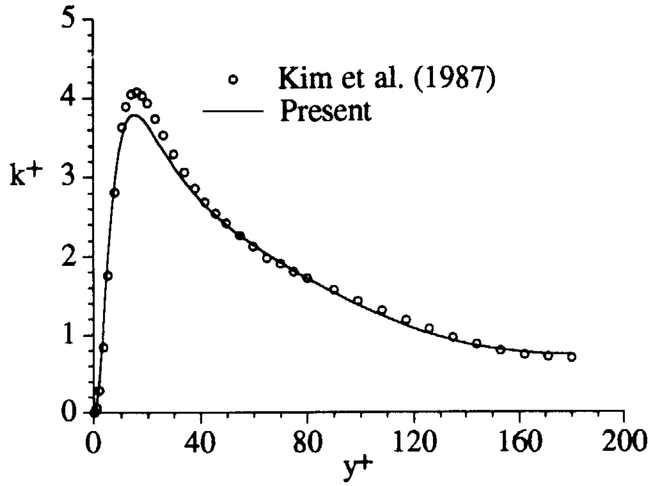

Fig. 4b Comparison of calculated k^+ with DNS data.

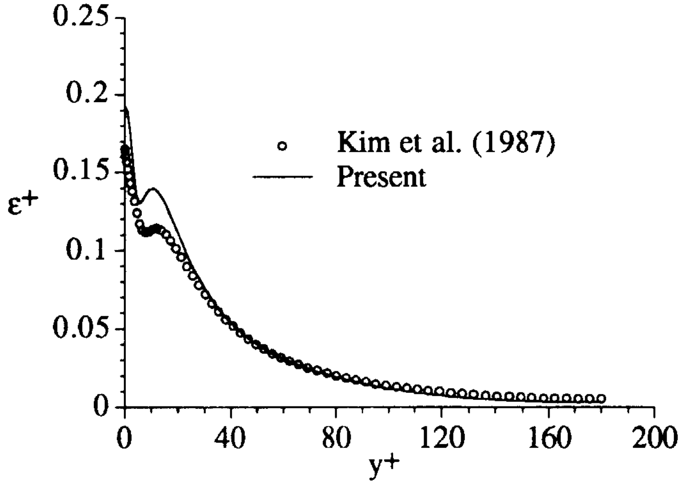

Fig. 4c Comparison of calculated ε^+ with DNS data.

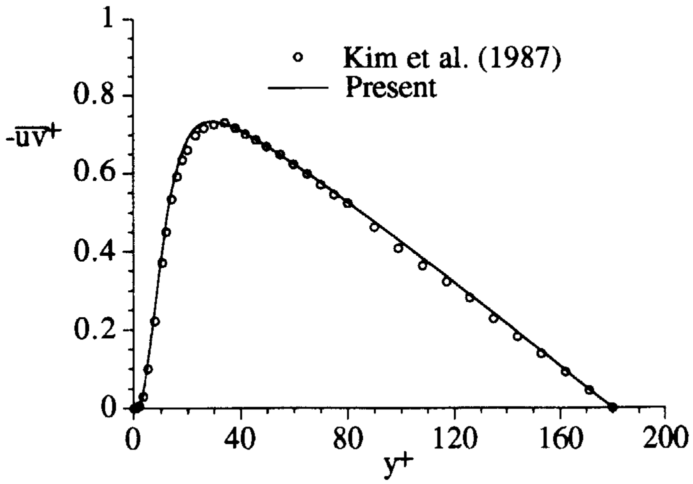

Fig. 4d Comparison of calculated $\overline{uv}^+$ with DNS data.

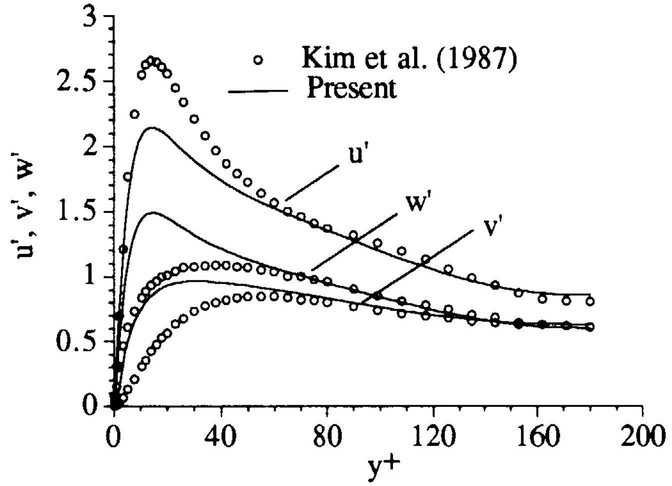

Fig. 4e Simulated and calculated turbulence intensities.

	Kim et al. (1987)	Present
κ	0.40	0.40
a_k	0.0829	0.096
a_u^2/a_k	1.563	1.329
$a_v^2/a_k \times 10^3$	0.977	11.57
a_w^2/a_k	0.435	0.651
$a_{uv}/(a_u\, a_v)$	0.222	0.037
$(a_u^2+a_v^2+a_w^2)/a_k$	2.00	1.99

Table 4. Simulated and calculated asymptotic behavior.

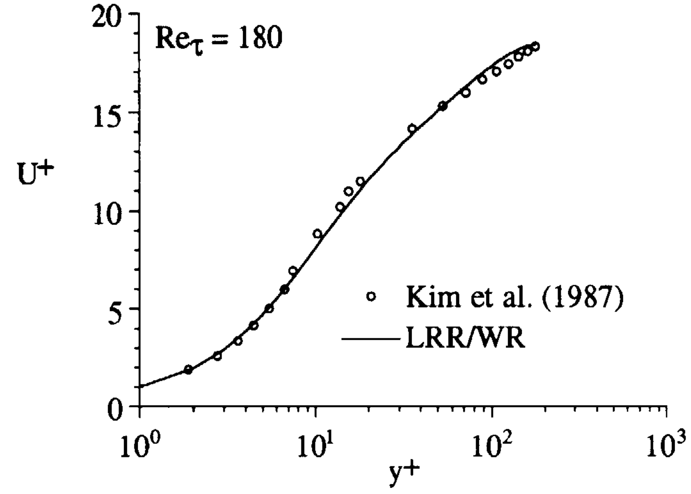

Fig. 5a Comparison of calculated U^+ with DNS data.

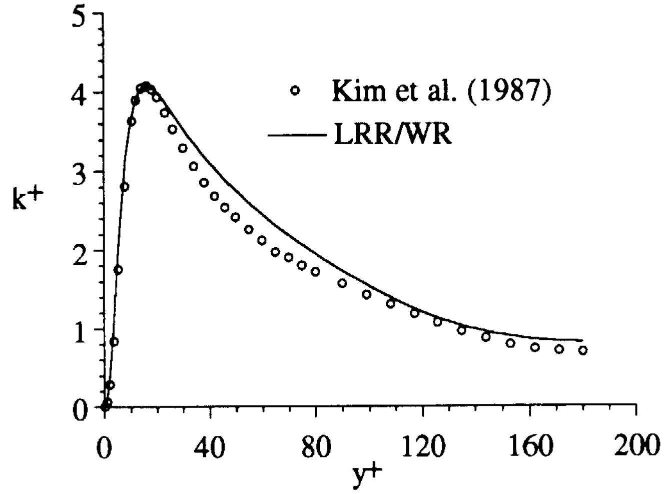

Fig. 5b Comparison of calculated k^+ with DNS data.

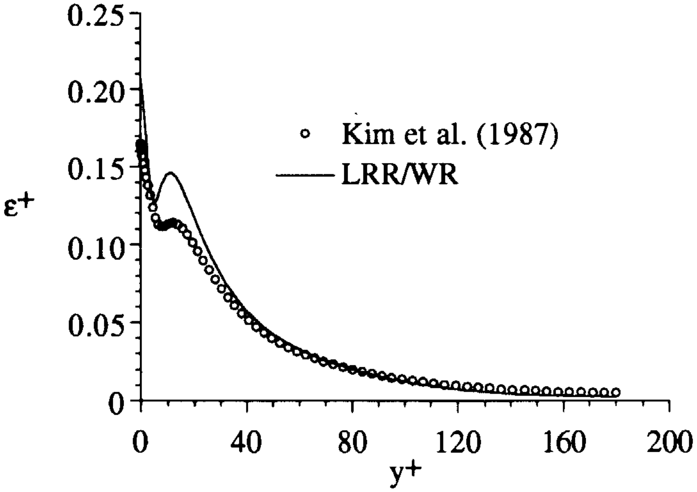

Fig. 5c Comparison of calculated ε^+ with DNS data.

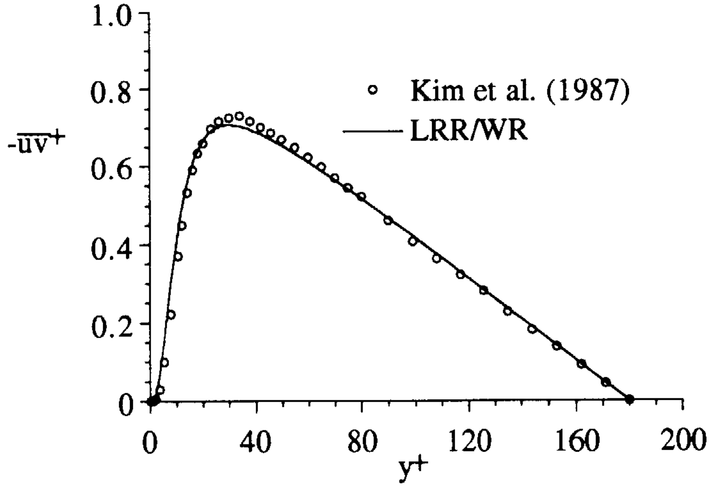

Fig. 5d Comparison of calculated $\overline{uv}^+$ with DNS data.

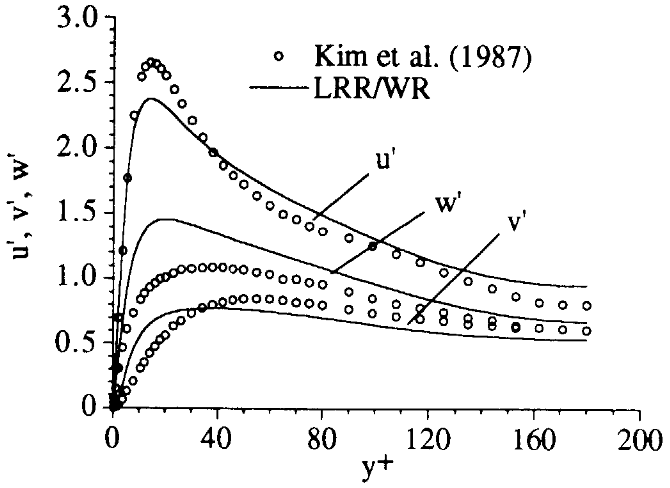

Fig. 5e Simulated and calculated turbulence intensities.

	Kim et al. (1987)	LRR/WR
κ	0.40	0.37
a_k	0.0829	0.1038
a_u^2/a_k	1.563	1.619
$a_v^2/a_k \times 10^3$	0.977	0.0755
a_w^2/a_k	0.435	0.385
$a_{uv}/(a_u\, a_v)$	0.222	1.298
$(a_u^2+a_v^2+a_w^2)/a_k$	2.00	2.00

Table 5. Simulated and calculated asymptotic behavior.

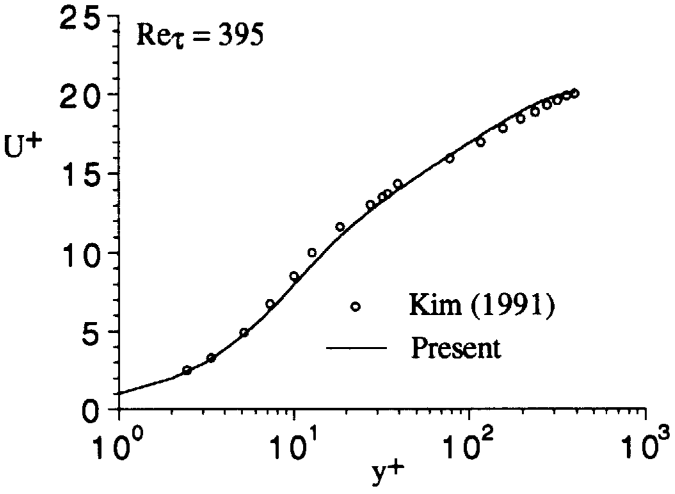

Fig. 6a Comparison of calculated U+ with DNS data.

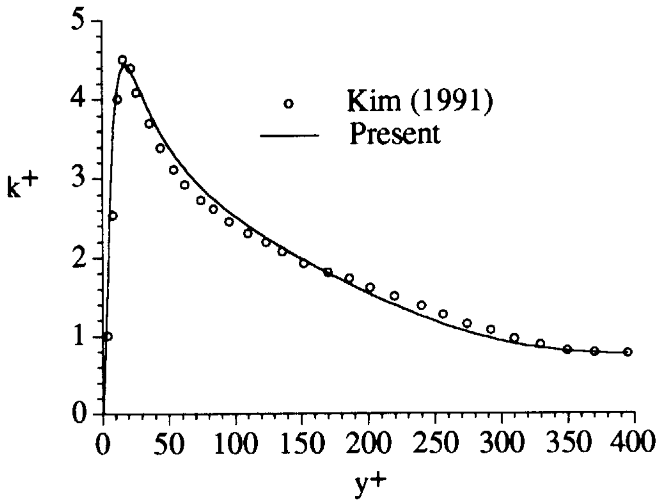

Fig. 6b Comparison of calculated k+ with DNS data.

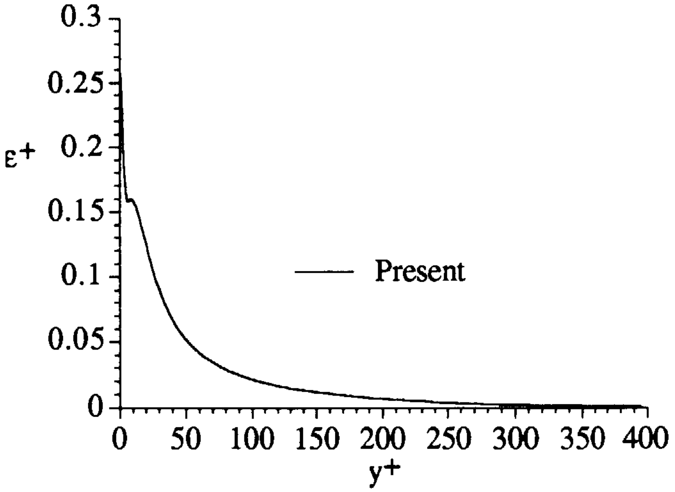

Fig. 6c Calculated ε+.

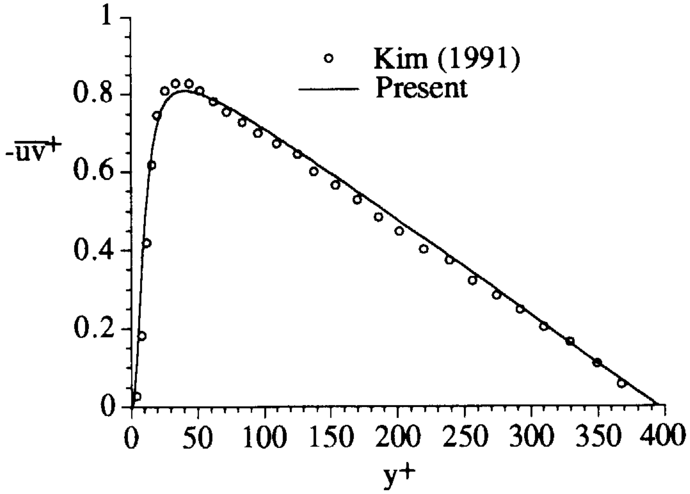

Fig. 6d Comparison of calculated $\overline{uv}^{+}$ with DNS data.

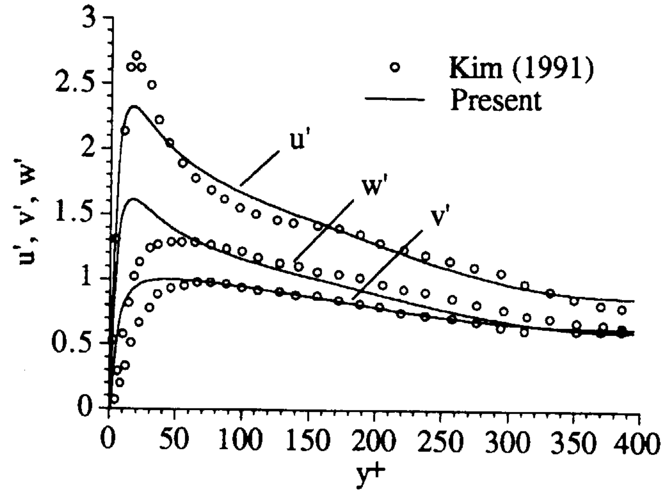

Fig. 6e Simulated and calculated turbulence intensities.

	Kim (1991)	Present
κ	0.40	0.39
a_k	-	0.130
a_u^2/a_k	-	1.349
$a_v^2/a_k \times 10^3$	-	12.97
a_w^2/a_k	-	0.638
$a_{uv}/(a_u\, a_v)$	-	0.095
$(a_u^2+a_v^2+a_w^2)/a_k$	-	2.00

Table 6. Simulated and calculated asymptotic behavior.

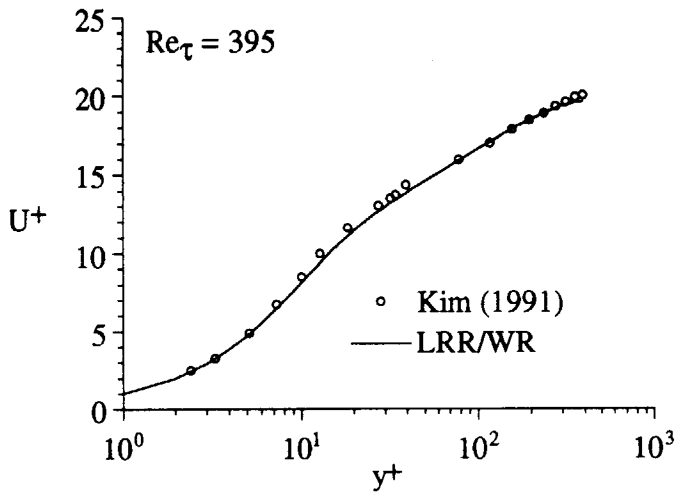

Fig. 7a Comparison of calculated U^+ with DNS data.

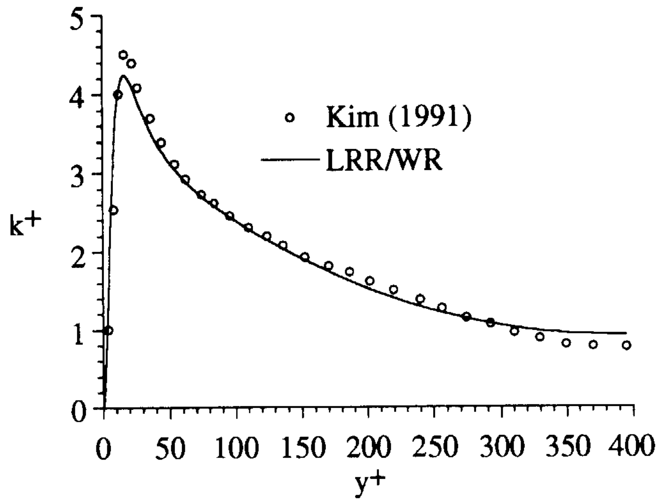

Fig. 7b Comparison of calculated k^+ with DNS data.

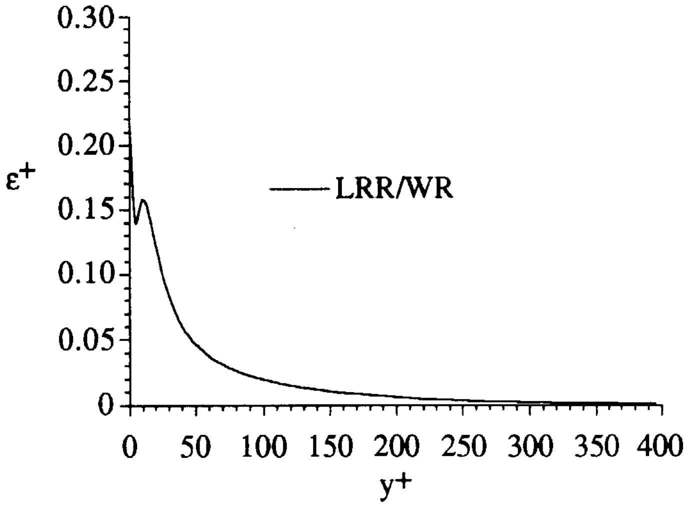

Fig. 7c Calculated ε^+.

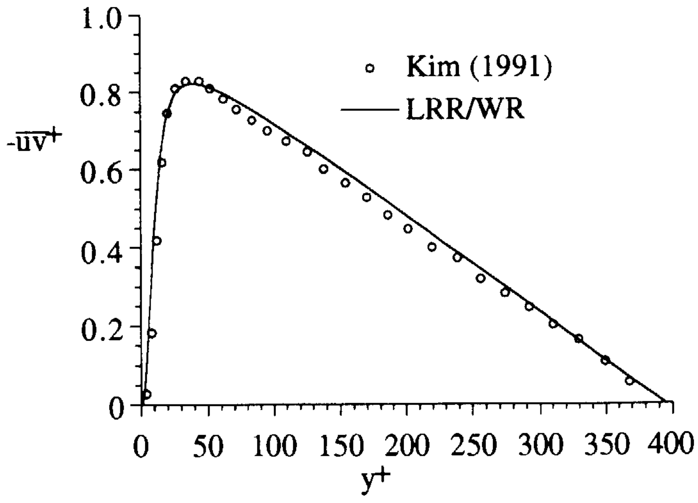

Fig. 7d Comparison of calculated $\overline{uv}^+$ with DNS data.

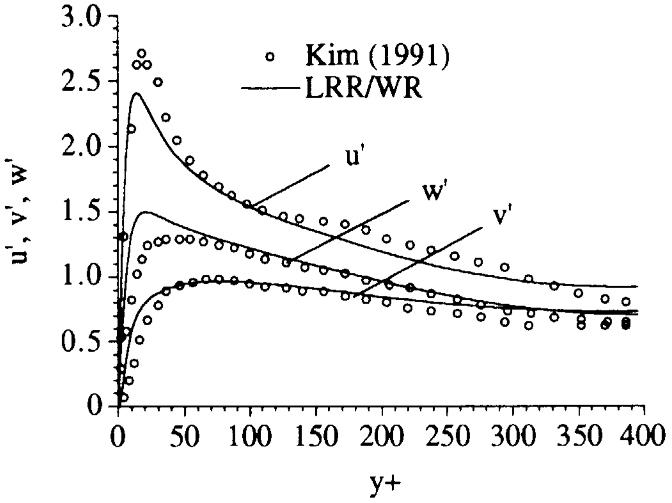

Fig. 7e Simulated and calculated turbulence intensities.

	Kim (1991)	LRR/WR
κ	0.40	0.40
a_k	-	0.1089
a_u^2/a_k	-	1.544
$a_v^2/a_k \times 10^3$	-	0.053
a_w^2/a_k	-	0.444
$a_{uv}/(a_u\, a_v)$	-	1.575
$(a_u^2+a_v^2+a_w^2)/a_k$	-	1.99

Table 7. Simulated and calculated asymptotic behavior.

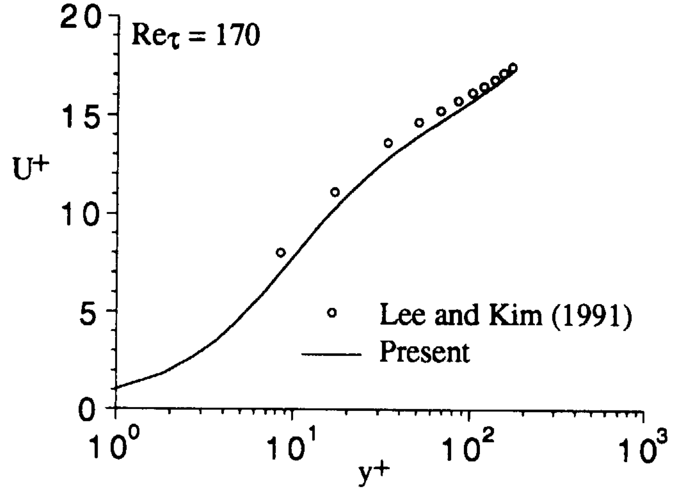

Fig. 8a Comparison of calculated U^+ with DNS data.

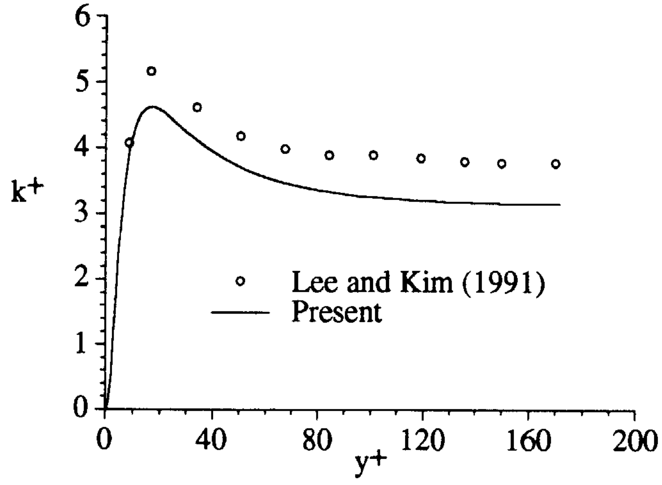

Fig. 8b Comparison of calculated k^+ with DNS data.

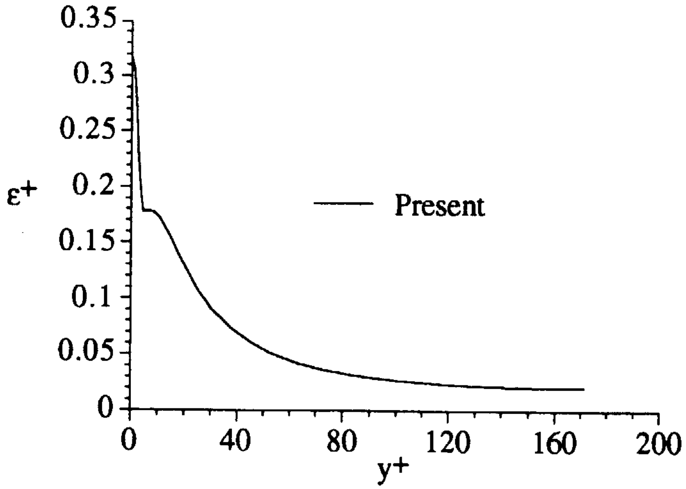

Fig. 8c Calculated ε^+.

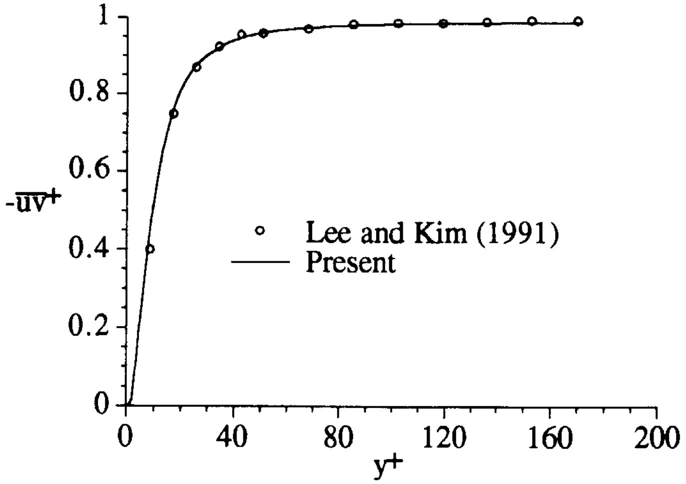

Fig. 8d Comparison of calculated $\overline{uv}^+$ with DNS data.

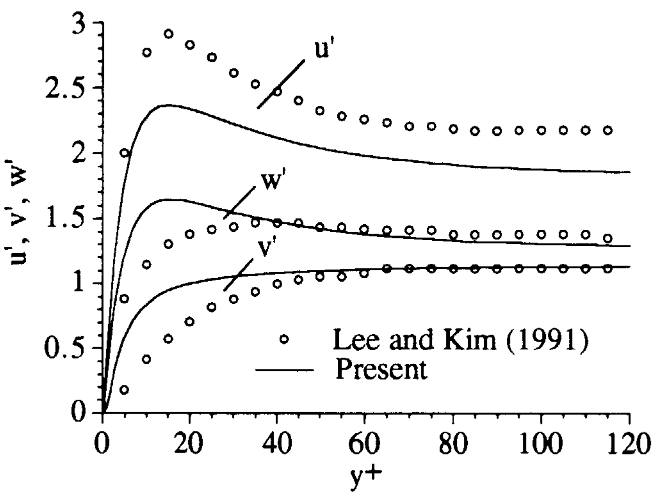

Fig. 8e Simulated and calculated turbulence intensities.

	Lee and Kim (1991)	Present
κ	0.40	0.38
a_k	-	0.158
a_u^2/a_k	-	1.369
$a_v^2/a_k \times 10^3$	-	15.82
a_w^2/a_k	-	0.608
$a_{uv}/(a_u a_v)$	-	0.133
$(a_u^2+a_v^2+a_w^2)/a_k$	-	1.99

Table 8. Simulated and calculated asymptotic behavior.

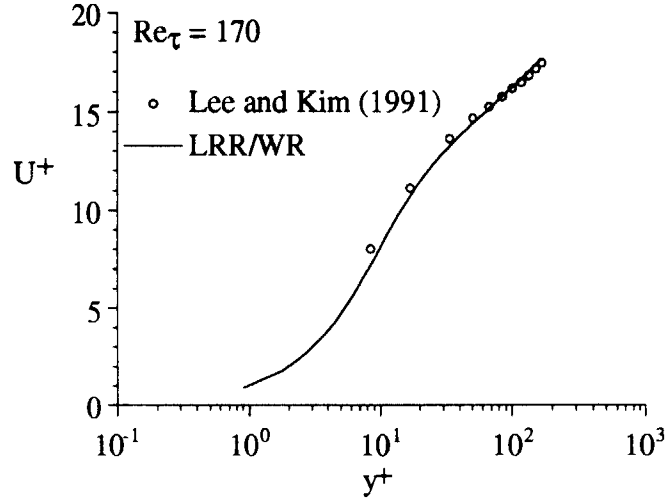

Fig. 9a Comparison of calculated U+ with DNS data.

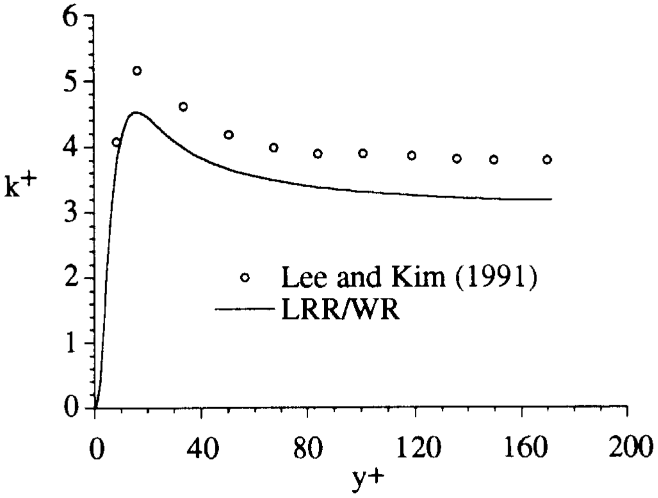

Fig. 9b Comparison of calculated k+ with DNS data.

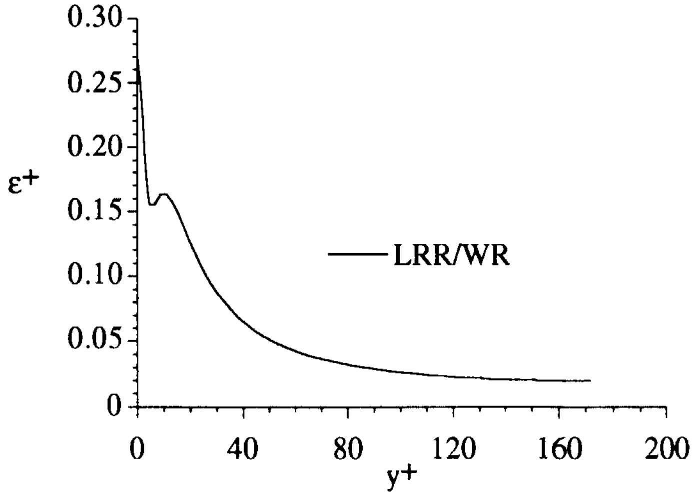

Fig. 9c Calculated ε+.

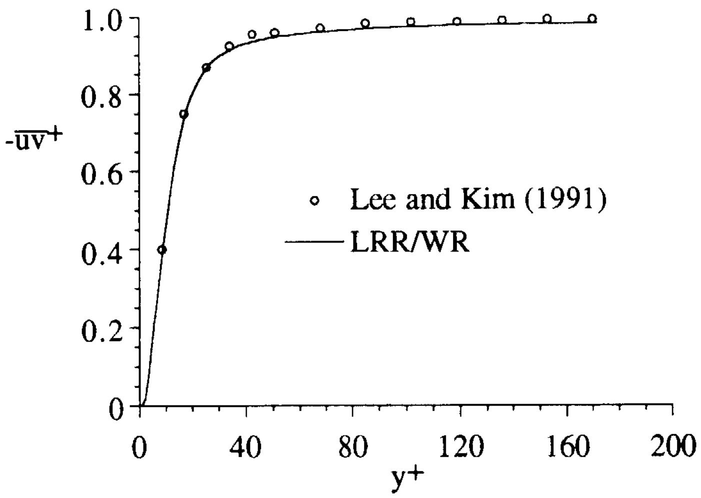

Fig. 9d Comparison of calculated $\overline{uv}^+$ with DNS data.

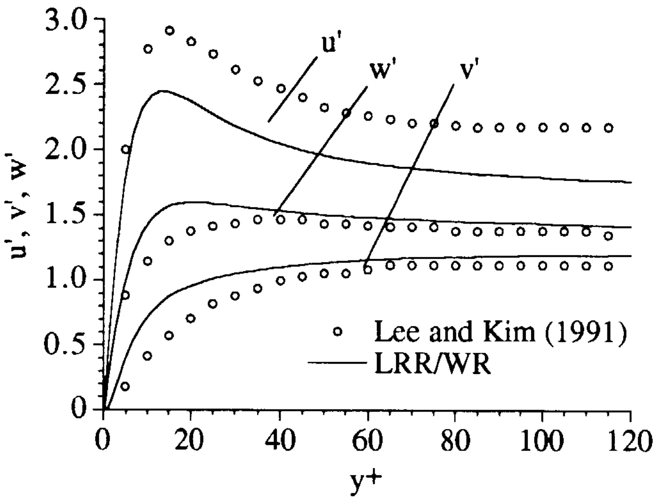

Fig. 9e Simulated and calculated turbulence intensities.

	Lee and Kim (1991)	LRR/WR
κ	0.40	0.40
a_k	-	0.1305
a_u^2/a_k	-	1.552
a_v^2/a_k x 10^3	-	0.386
a_w^2/a_k	-	0.441
$a_{uv}/(a_u\ a_v)$	-	0.692
$(a_u^2+a_v^2+a_w^2)/a_k$	-	1.99

Table 9. Simulated and calculated asymptotic behavior.

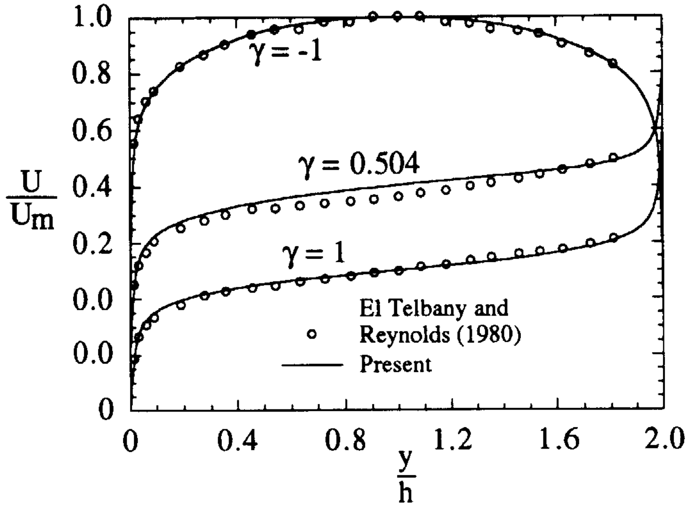

Fig. 10a Comparison of calculated U with experimental data.

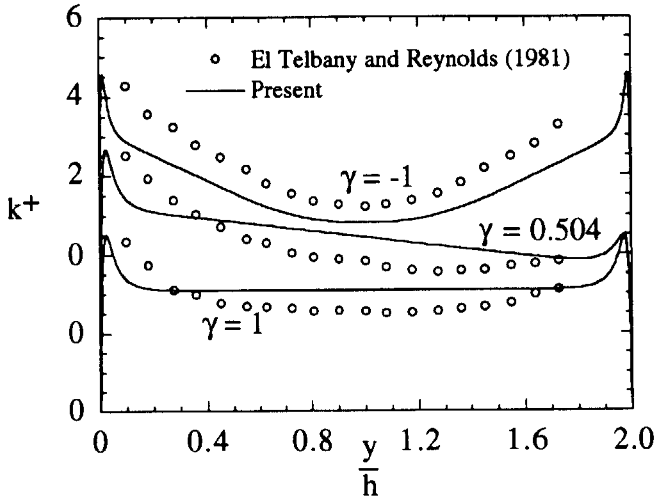

Fig. 10b Comparison of calculated k^+ with experimental data.

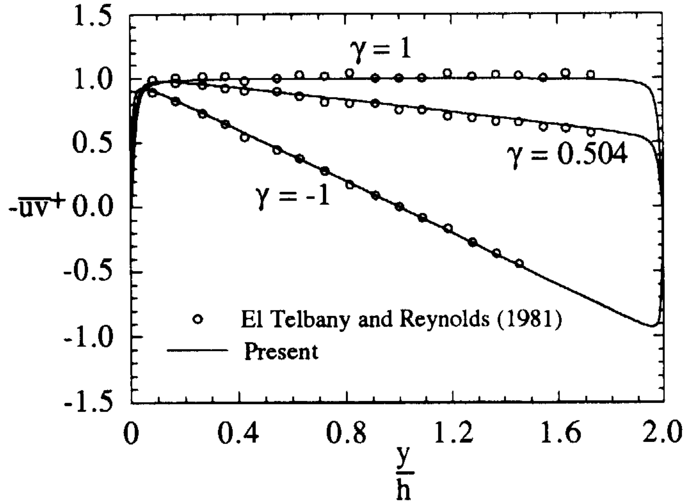

Fig. 10c Comparison of calculated $\overline{uv}^+$ with experimental data.

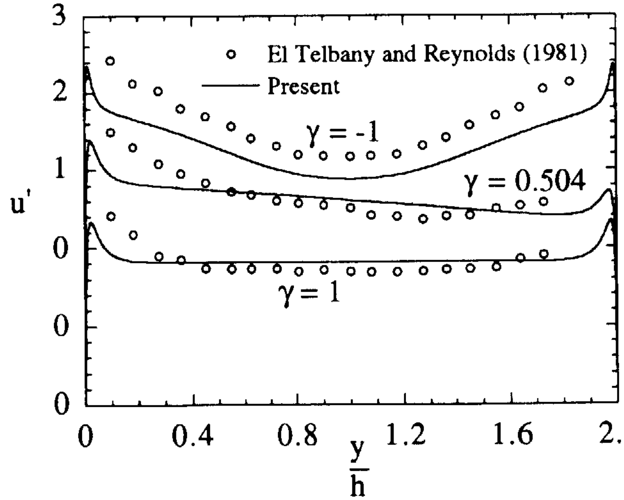

Fig. 10d Comparison of calculated u' with experimental data.

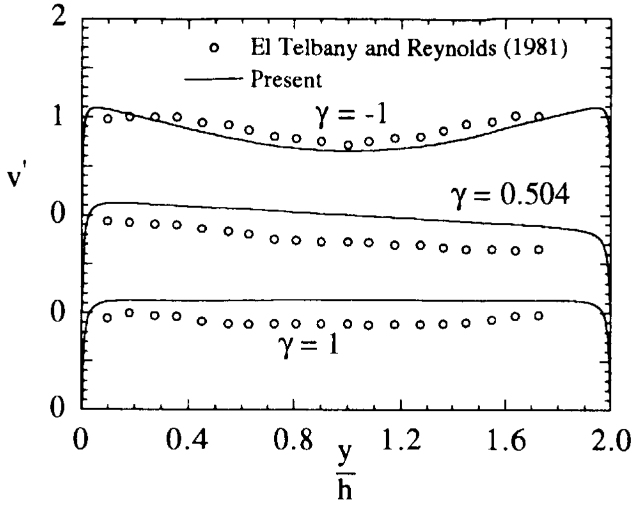

Fig. 10e Comparison of calculated v' with experimental data.

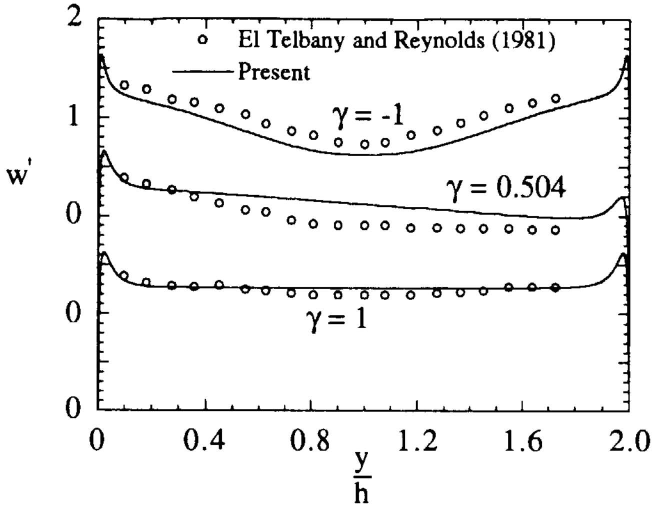

Fig. 10f Comparison of calculated w' with experimental data.

	Present		
	$\gamma = 1$ $Re_\tau = 625$	$\gamma = -1$ $Re_\tau = 1463$	$\gamma = 0.504$ $Re_\tau = 1456$
κ	0.40	0.39	0.40
a_k	0.151	0.150	0.159
a_u^2/a_k	1.337	1.318	1.342
$a_v^2/a_k \times 10^3$	15.22	15.77	17.71
a_w^2/a_k	0.637	0.652	0.645
$a_{uv}/(a_u a_v)$	0.136	0.126	0.102
$(a_u^2+a_v^2+a_w^2)/a_k$	1.99	1.99	2.00

Table 4. Experimental and calculated asymptotic behavior (Experimentally determined von Karman constant is approximately 0.39 for all three cases).

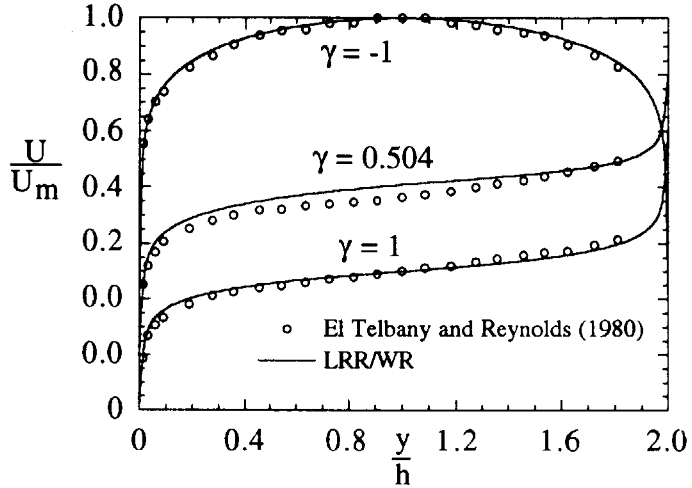

Fig. 11a Comparison of calculated U with experimental data.

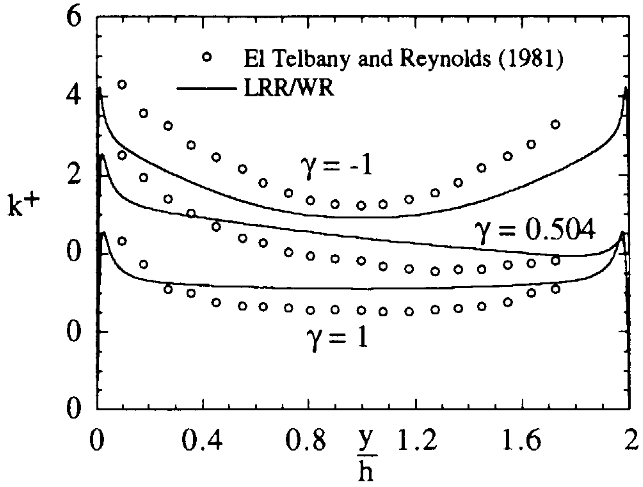

Fig. 11b Comparison of calculated k^+ with experimental data.

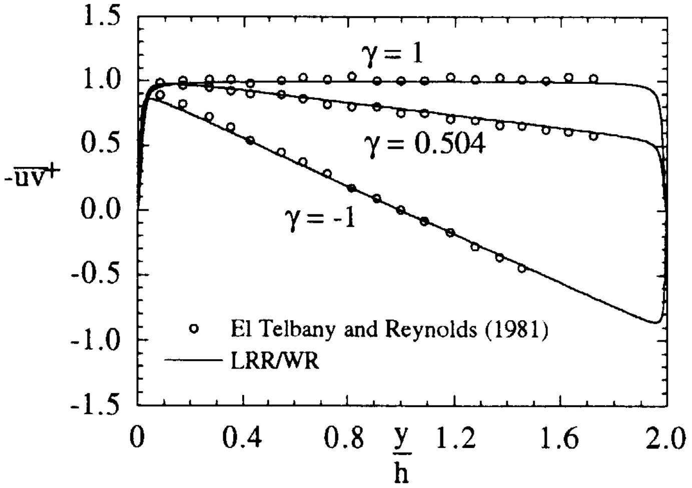

Fig. 11c Comparison of calculated $\overline{uv}^+$ with experimental data.

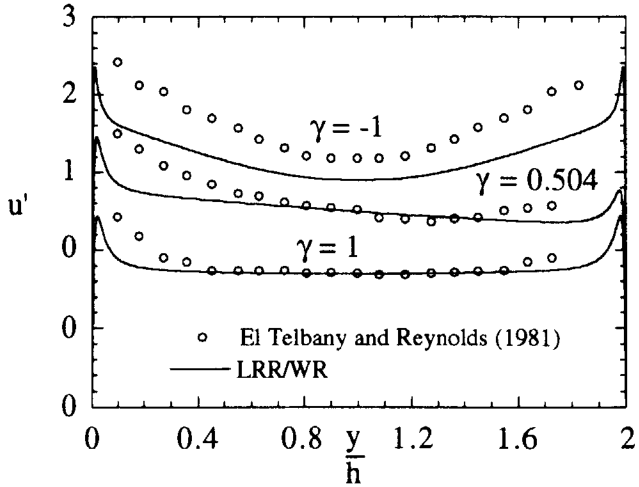

Fig. 11d Comparison of calculated u' with experimental data.

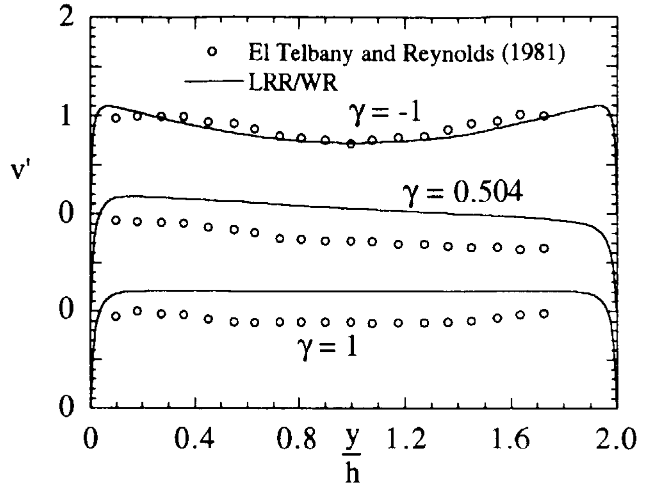

Fig. 11e Comparison of calculated v' with experimental data.

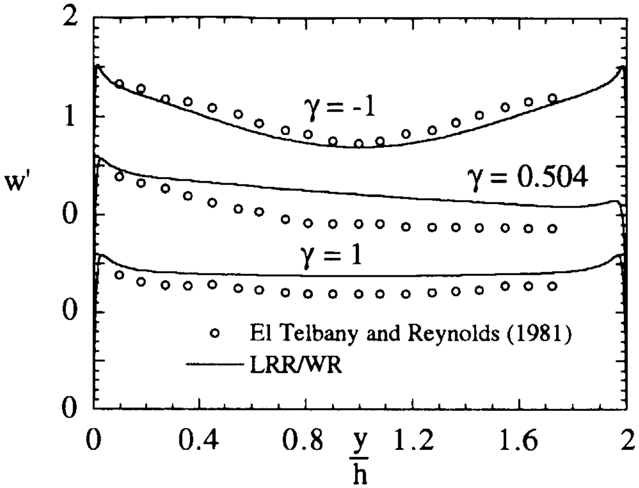

Fig. 11f Comparison of calculated w' with experimental data.

	LRR/WR		
	$\gamma = 1$ $Re_\tau = 625$	$\gamma = -1$ $Re_\tau = 1463$	$\gamma = 0.504$ $Re_\tau = 1456$
κ	0.40	0.39	0.39
a_k	0.125	0.140	0.143
a_u^2/a_k	1.516	1.418	1.333
$a_v^2/a_k \times 10^3$	0.371	0.420	0.521
a_w^2/a_k	0.462	0.533	0.471
$a_{uv}/(a_u\, a_v)$	0.708	0.605	0.803
$(a_u^2+a_v^2+a_w^2)/a_k$	1.99	2.00	1.99

Table 11. Experimental and calculated asymptotic behavior (Experimentally determined von Karman constant is approximately 0.39 for all three cases).

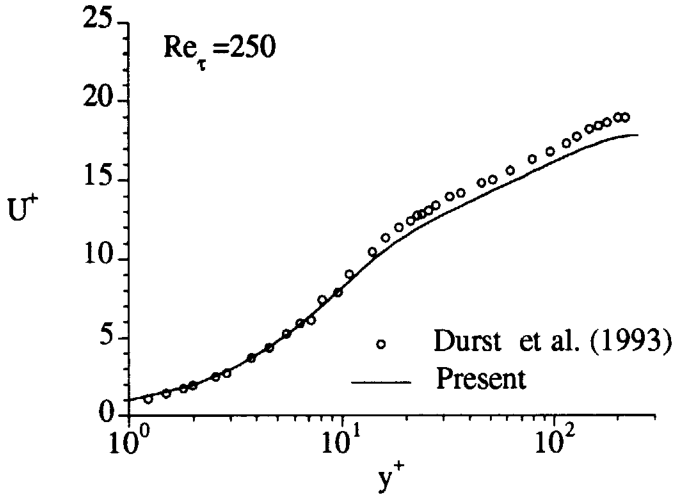

Fig. 12a Comparison of calculated U^+ with data.

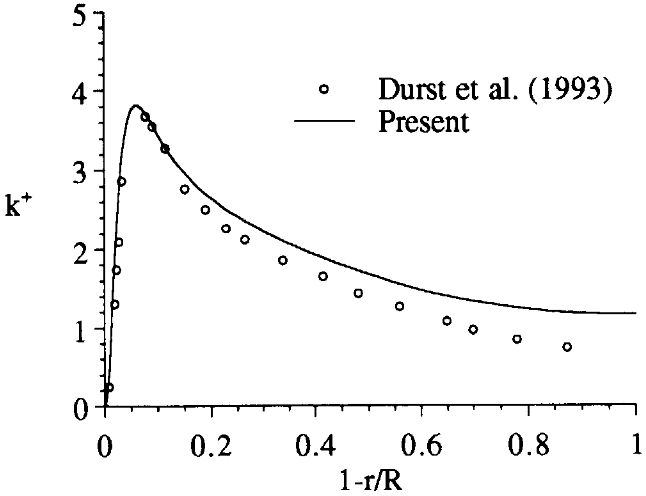

Fig. 12b Comparison of calculated k^+ with data.

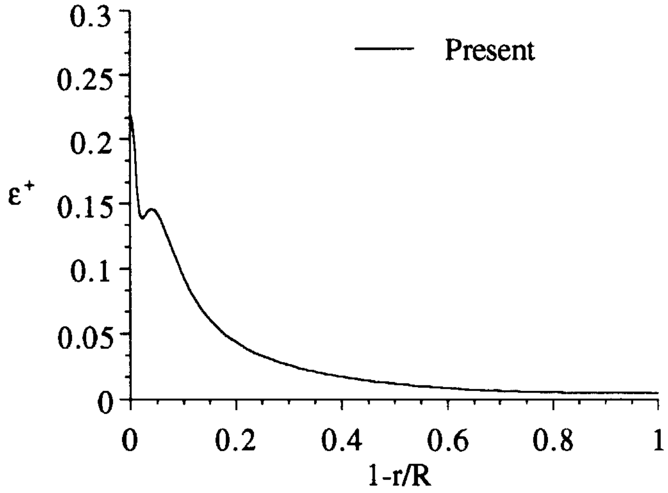

Fig. 12c Calculated distribution of ε^+.

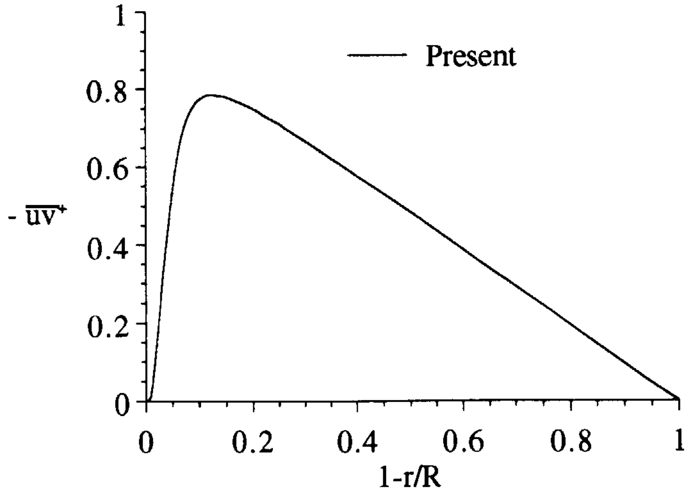

Fig. 12d Calculated distribution of $\overline{uv}^+$.

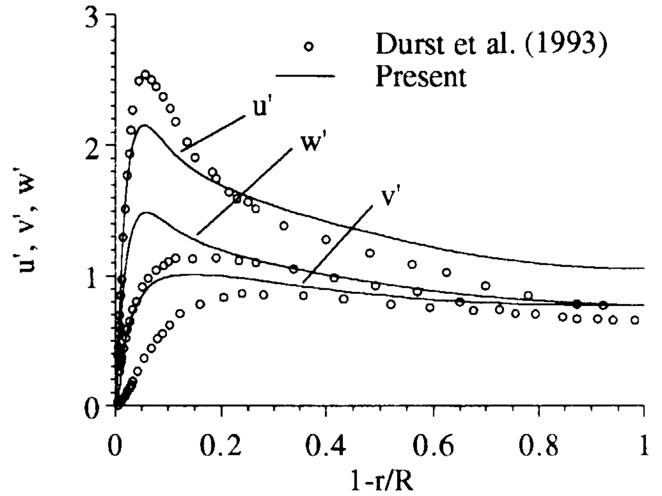

Fig. 12e Comparison of calculated normal stresses with data.

	Durst et al. (1993)	Present
κ	0.40	0.39
a_k	---	0.11
a_u^2/a_k	---	1.43
$a_v^2/a_k \times 10^3$	---	12.4
a_w^2/a_k	---	0.63
$a_{uv}/(a_u\, a_v)$	---	0.11
$(a_u^2+a_v^2+a_w^2)/a_k$	---	2.07

Table 12 Comparison of near-wall asymptotes with data.

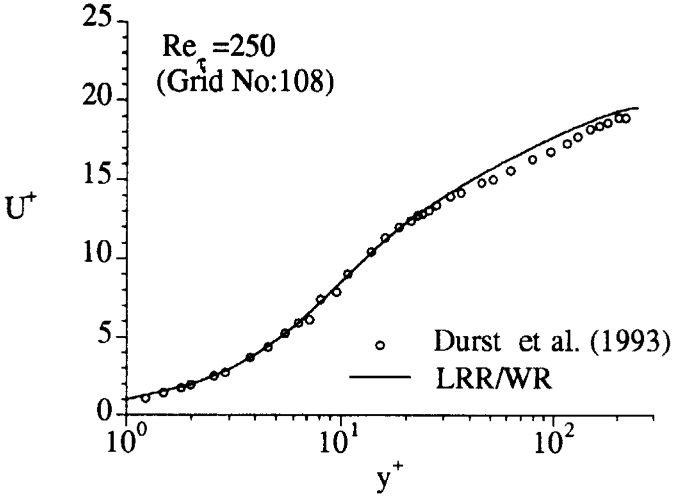

Fig. 13a Comparison of calculated U+ with data.

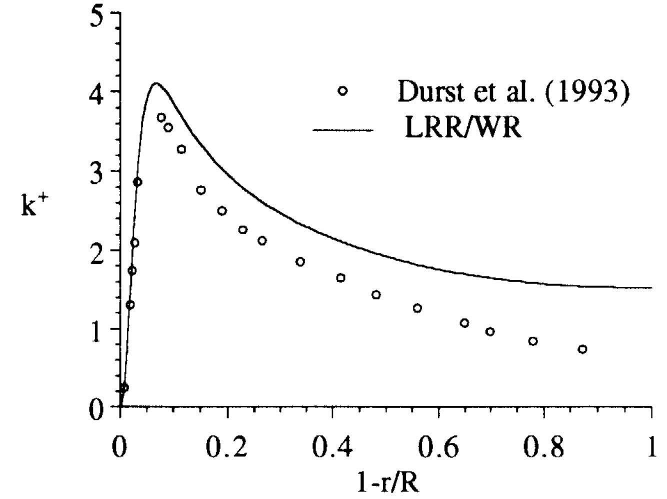

Fig. 13b Comparison of calculated k+ with data.

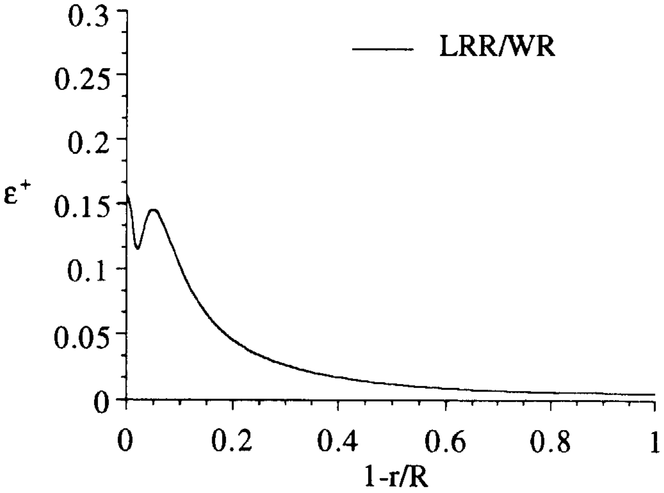

Fig. 13c Calculated distribution of ε+.

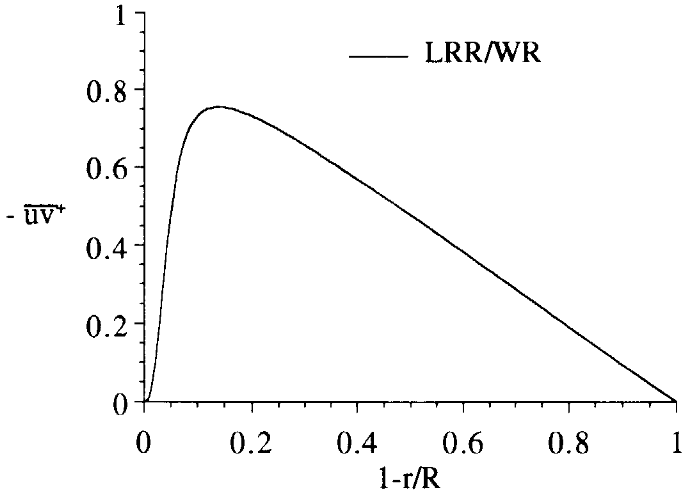

Fig. 13d Calculated distribution of $\overline{uv}^+$.

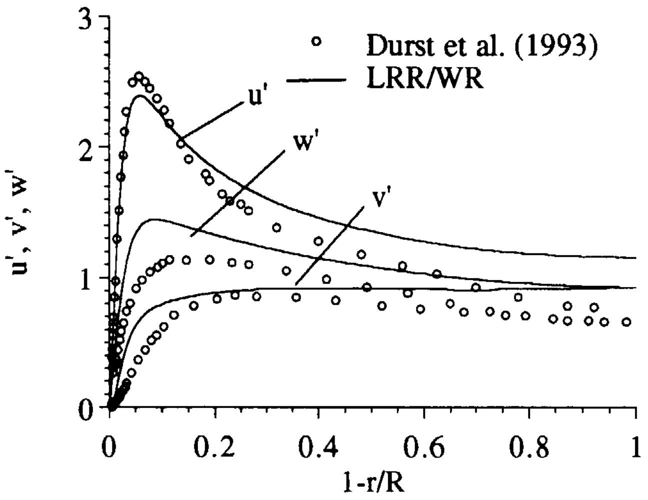

Fig. 13e Comparison of calculated normal stresses with data.

	Durst et al. (1993)	LRR/WR
κ	0.40	0.37
a_k	---	0.08
a_u^2/a_k	---	1.56
$a_v^2/a_k \text{ x } 10^3$	---	2.49
a_w^2/a_k	---	0.38
$a_{uv}/(a_u\ a_v)$	---	0.23
$(a_u^2+a_v^2+a_w^2)/a_k$	---	1.94

Table 13 Comparison of near-wall asymptotes with data.

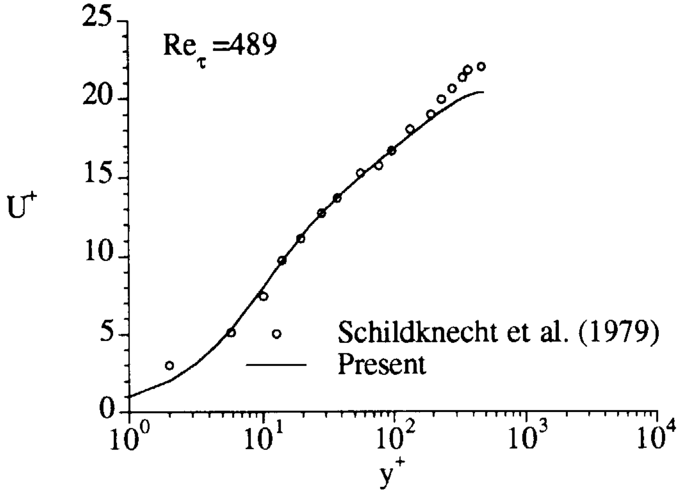

Fig. 14a Comparison of calculated U^+ with data.

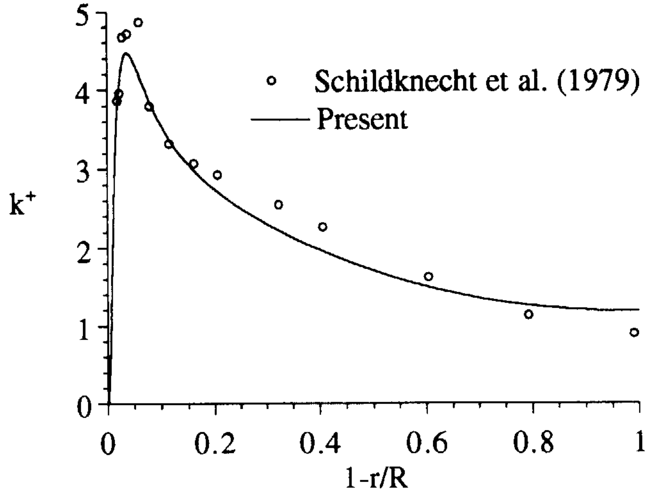

Fig. 14b Comparison of calculated k^+ with data.

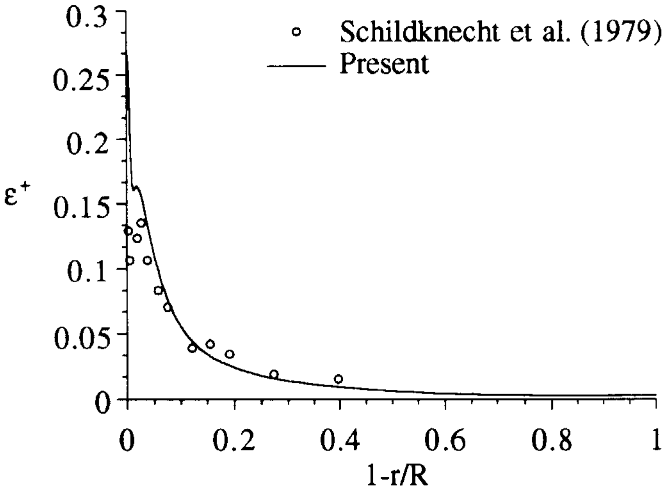

Fig. 14c Comparison of calculated ε^+ with data.

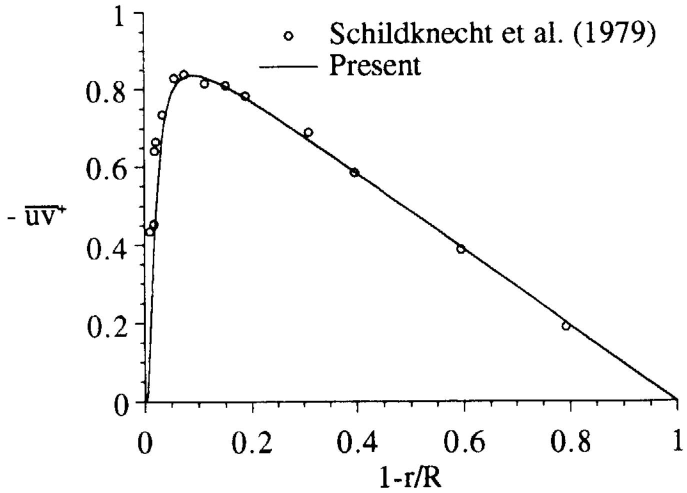

Fig. 14d Comparison of calculated $\overline{uv}^+$ with data.

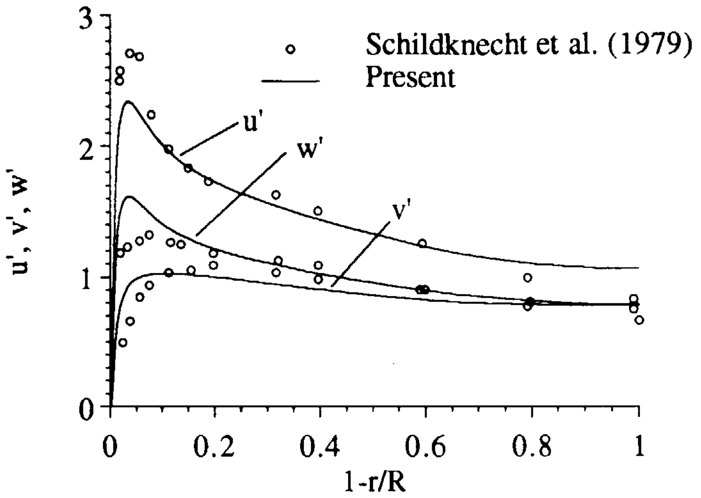

Fig. 14e Comparison of calculated normal stresses with data.

	Schildknecht (1979)	Present
κ	0.41	0.40
a_k	---	0.13
a_u^2/a_k	---	1.38
$a_v^2/a_k \times 10^3$	---	14.9
a_w^2/a_k	---	0.64
$a_{uv}/(a_u\, a_v)$	---	0.12
$(a_u^2+a_v^2+a_w^2)/a_k$	---	2.03

Table 14 Comparison of near-wall asymptotes with data.

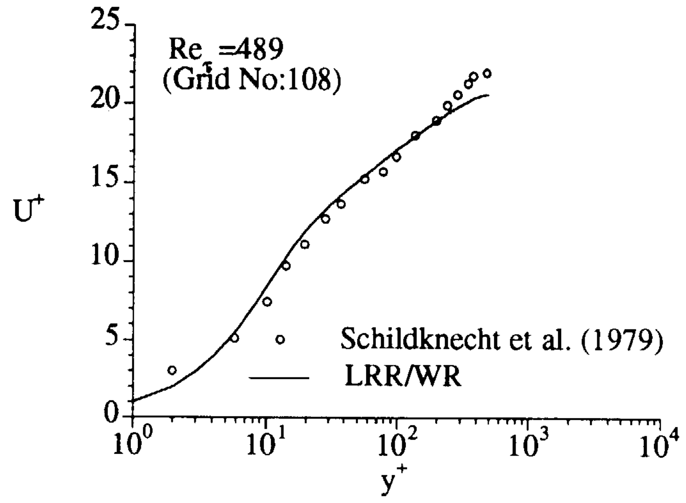

Fig. 15a Comparison of calculated U+ with data.

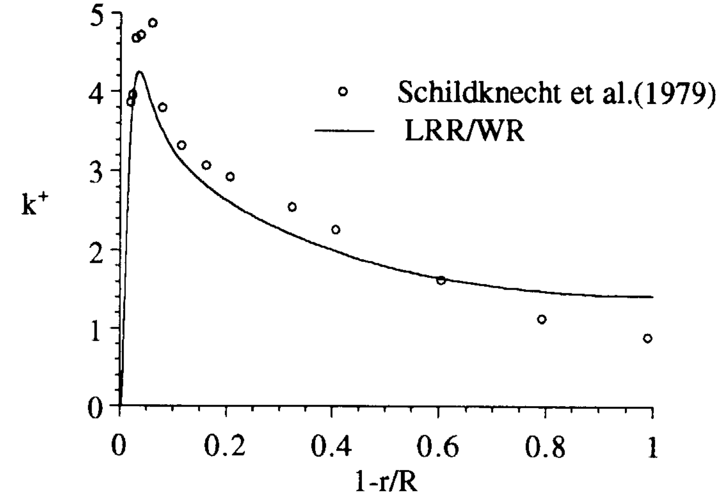

Fig. 15b Comparison of calculated k+ with data.

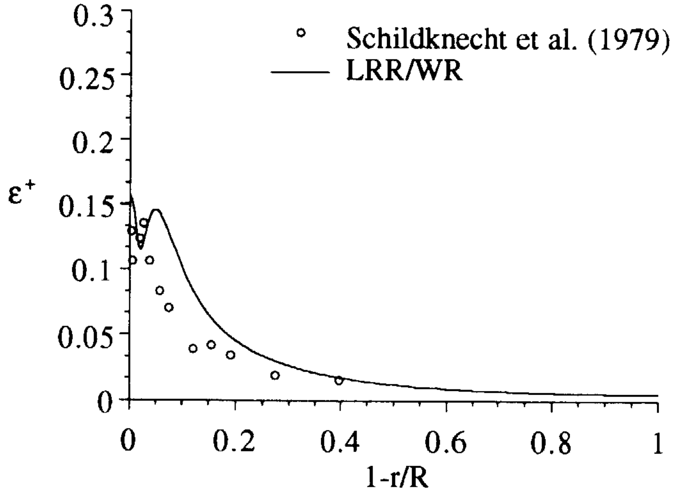

Fig. 15c Comparison of calculated ε+ with data.

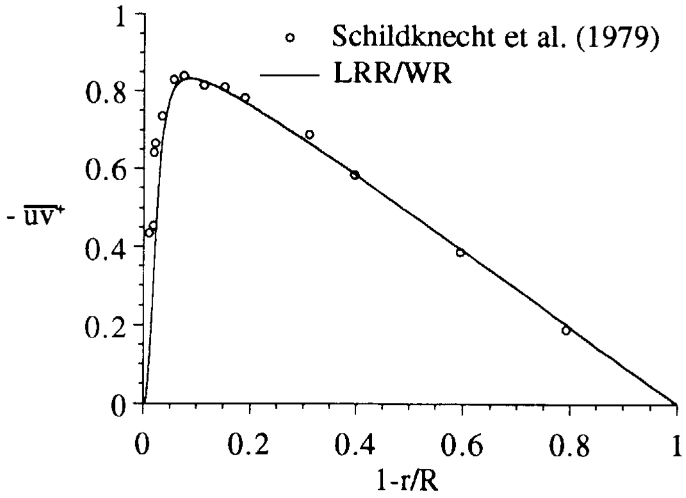

Fig. 15d Comparison of calculated $\overline{uv}^+$ with data.

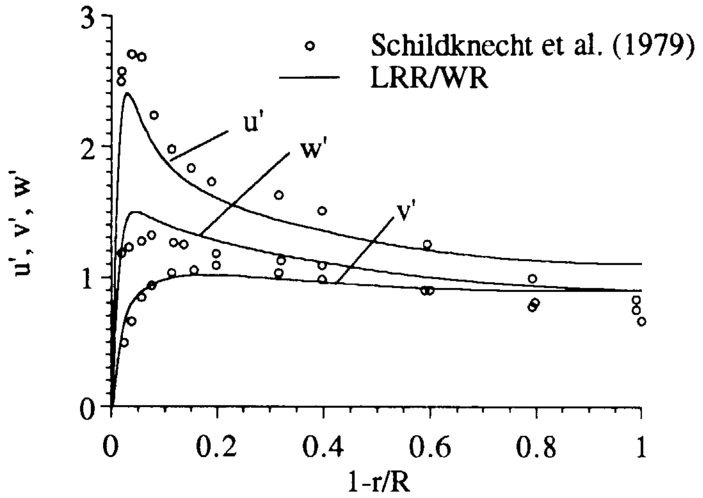

Fig. 15e Comparison of calculated normal stresses with data.

	Schildknecht (1979)	LRR/WR
κ	0.41	0.40
a_k	---	0.08
a_u^2/a_k	---	1.69
a_v^2/a_k x 10^3	---	3.48
a_w^2/a_k	---	0.42
$a_{uv}/(a_u\ a_v)$	---	0.21
$(a_u^2+a_v^2+a_w^2)/a_k$	---	2.12

Table 15 Comparison of near-wall asymptotes with data.

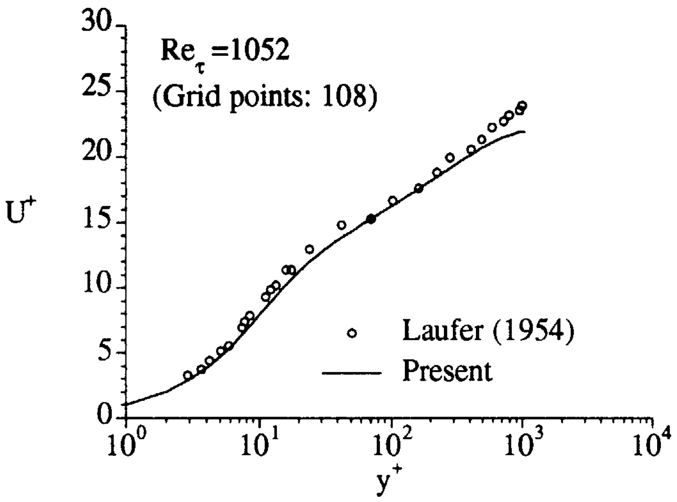

Fig. 16a Comparison of calculated U+ with data.

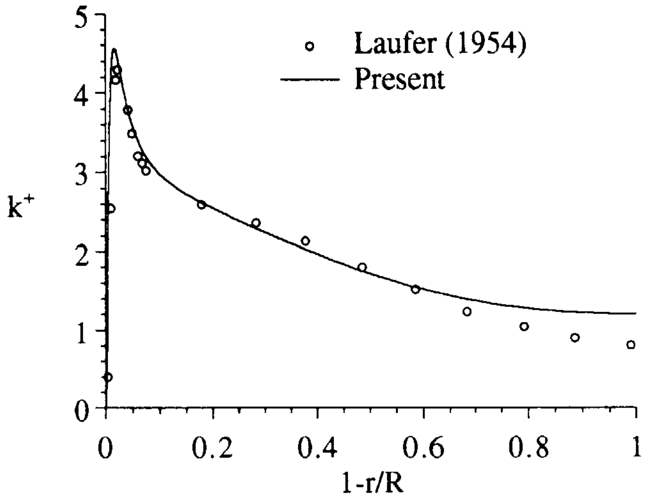

Fig. 16b Comparison of calculated k+ with data.

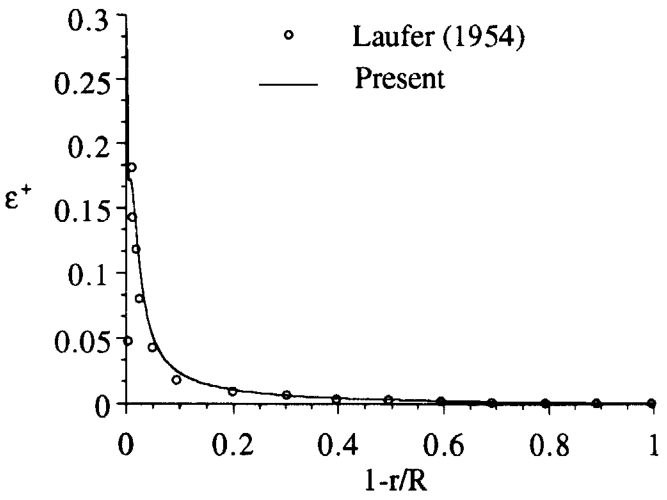

Fig. 16c Comparison of calculated ε+ with data.

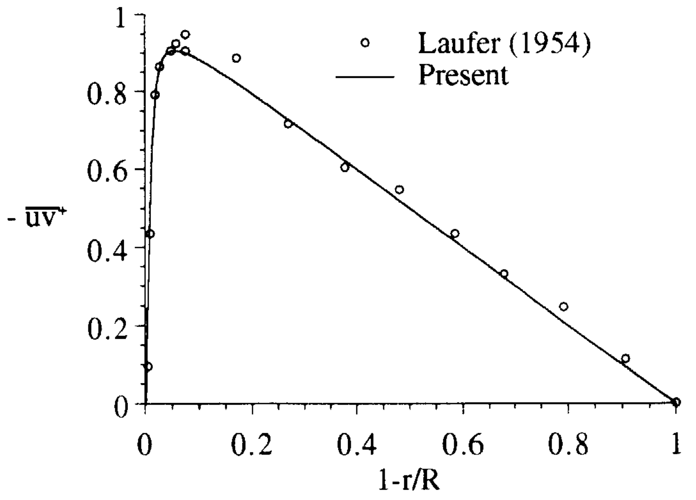

Fig. 16d Comparison of calculated $\overline{uv}^+$ with data.

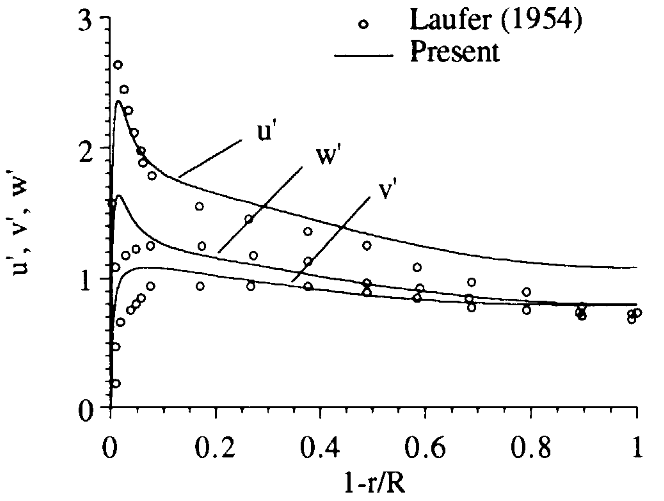

Fig. 16e Comparison of calculated normal stresses with data.

	Laufer (1954)	Present
κ	0.40	0.40
a_k	---	0.15
a_u^2/a_k	---	1.33
$a_v^2/a_k \times 10^3$	---	17.9
a_w^2/a_k	---	0.64
$a_{uv}/(a_u a_v)$	---	0.12
$(a_u^2+a_v^2+a_w^2)/a_k$	---	1.99

Table 16 Comparison of near-wall asymptotes with data.

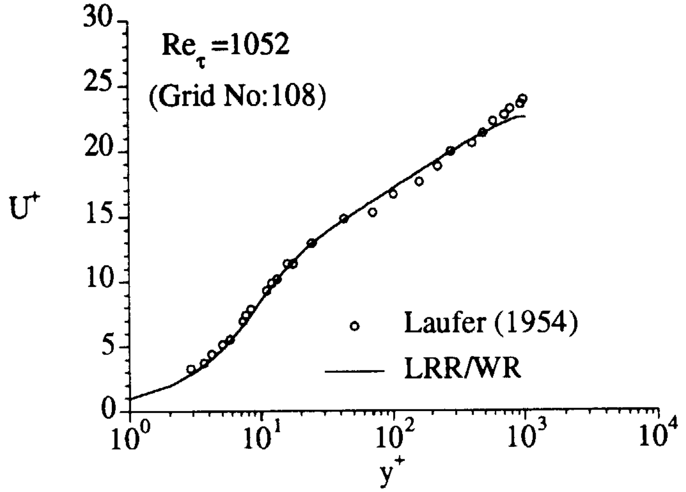

Fig. 17a Comparison of calculated U^+ with data.

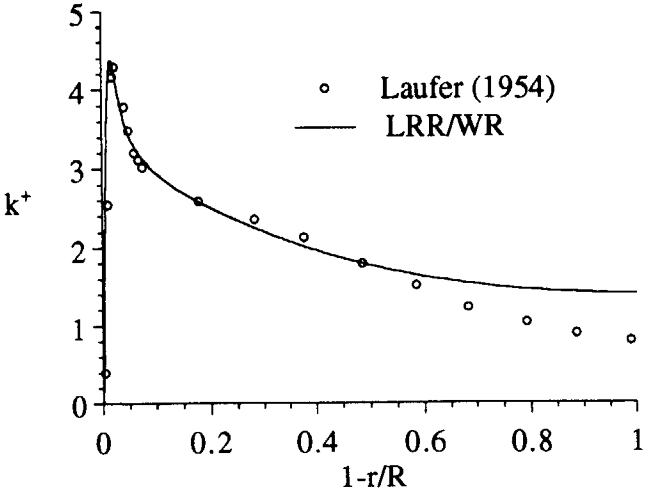

Fig. 17b Comparison of calculated k^+ with data.

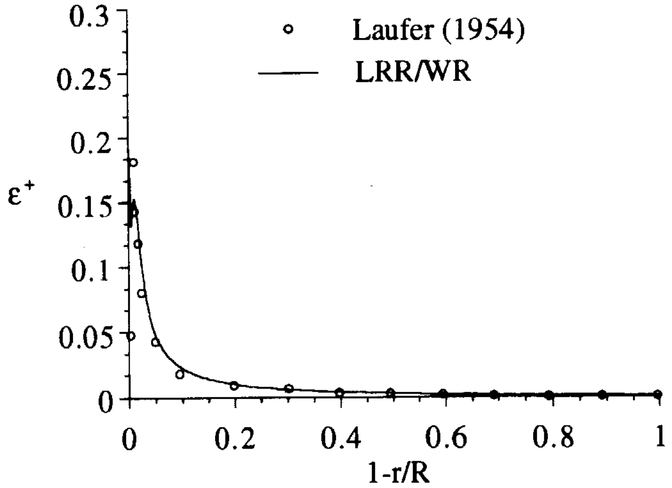

Fig. 17c Comparison of calculated ε^+ with data.

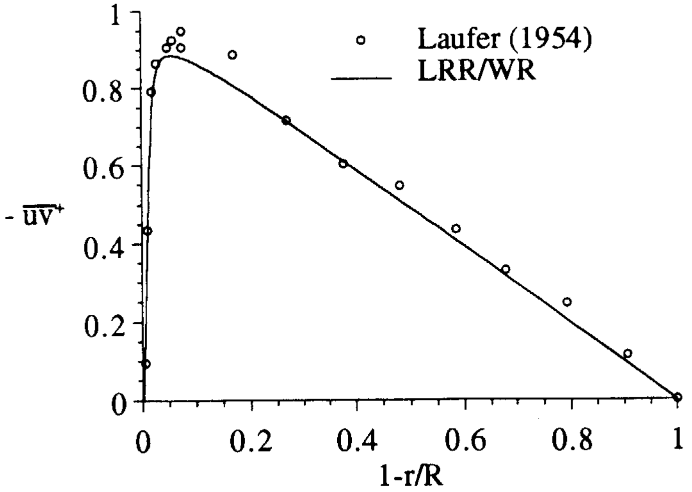

Fig. 17d Comparison of calculated $\overline{uv}^+$ with data.

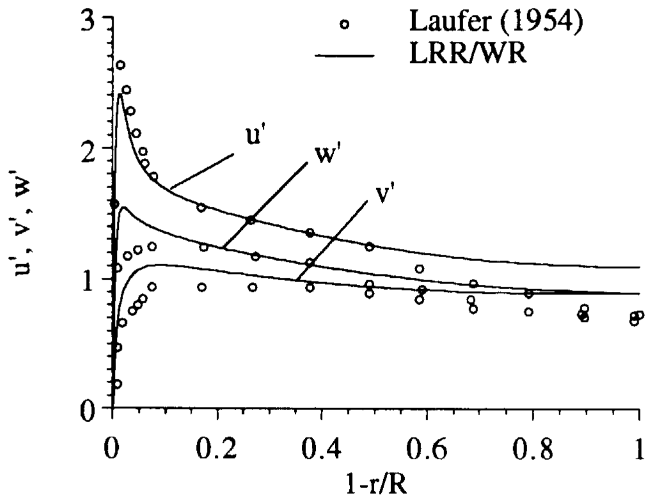

Fig. 17e Comparison of calculated normal stresses with data.

	Laufer (1954)	LRR/WR
κ	0.40	0.40
a_k	---	0.09
a_u^2/a_k	---	1.60
a_v^2/a_k x 10^3	---	3.91
a_w^2/a_k	---	0.44
$a_{uv}/(a_u\, a_v)$	---	0.24
$(a_u^2+a_v^2+a_w^2)/a_k$	---	2.05

Table 17 Comparison of near-wall asymptotes with data.

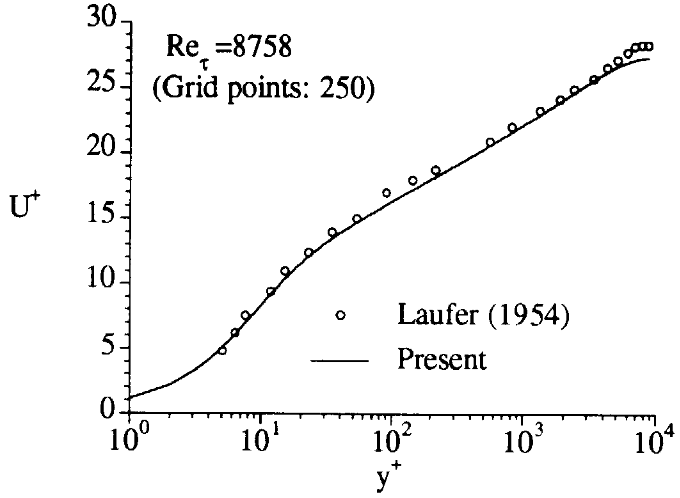

Fig. 18a Comparison of calculated U^+ with data.

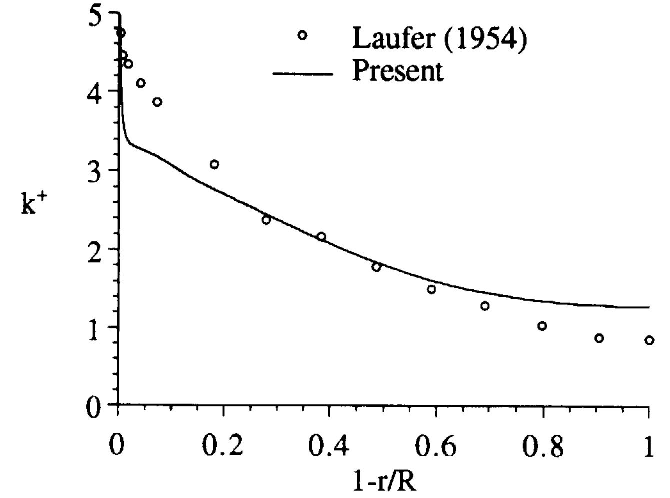

Fig. 18b Comparison of calculated k^+ with data.

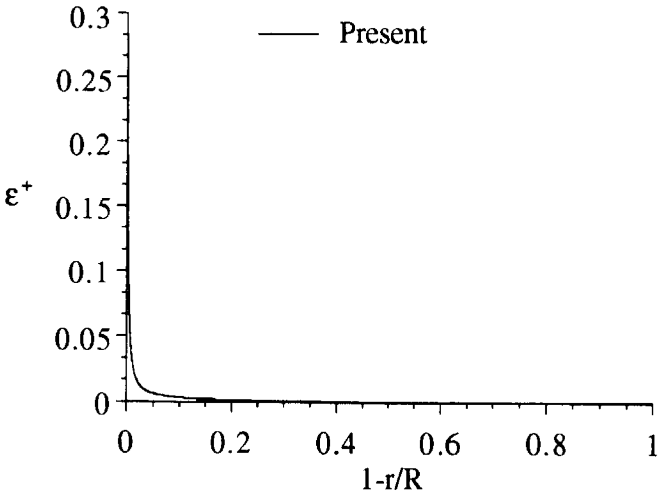

Fig. 18c Calculated distribution of ε^+.

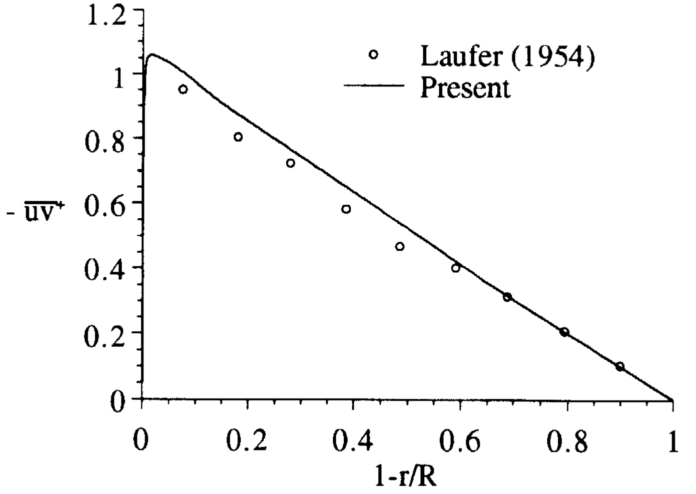

Fig. 18d Comparison of calculated $\overline{uv}^+$ with data.

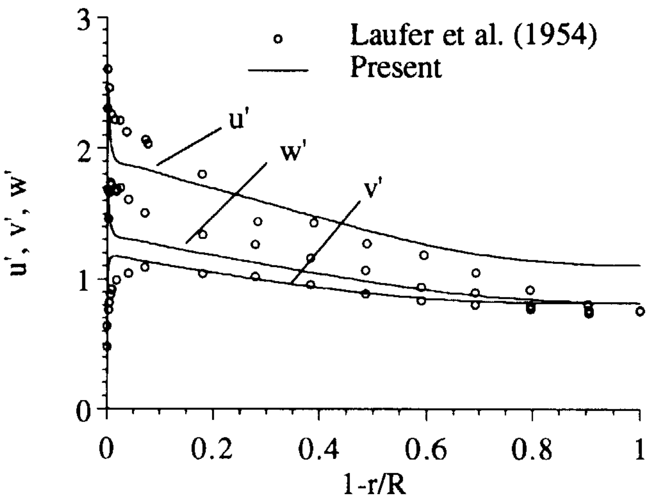

Fig. 18e Comparison of calculated normal stresses with data.

	Laufer (1954)	Present
κ	0.40	0.40
a_k	---	0.18
a_u^2/a_k	---	1.55
$a_v^2/a_k \times 10^3$	---	29.3
a_w^2/a_k	---	0.71
$a_{uv}/(a_u a_v)$	---	0.15
$(a_u^2+a_v^2+a_w^2)/a_k$	---	2.29

Table 18 Comparison of near-wall asymptotes with data.

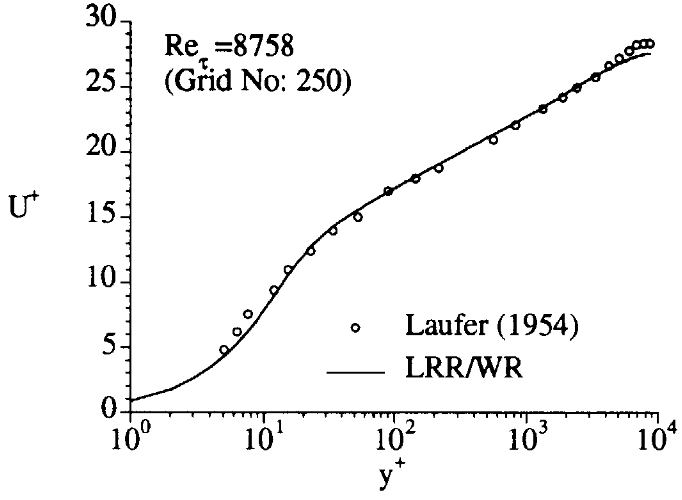

Fig. 19a Comparison of calculated U^+ with data.

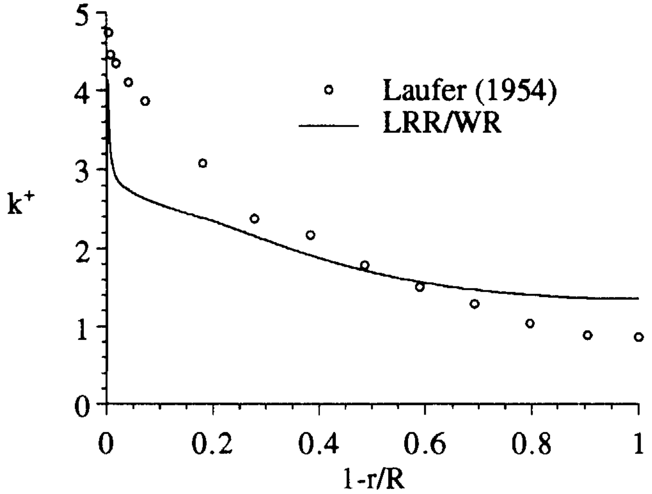

Fig. 19b Comparison of calculated k^+ with data.

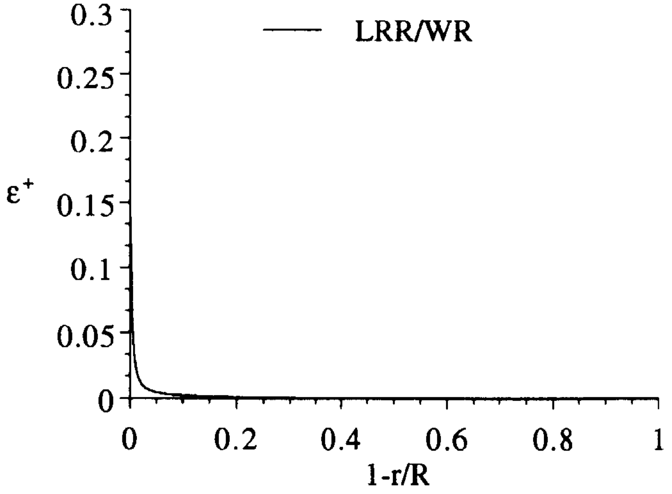

Fig. 19c Calculated distribution of ε^+.

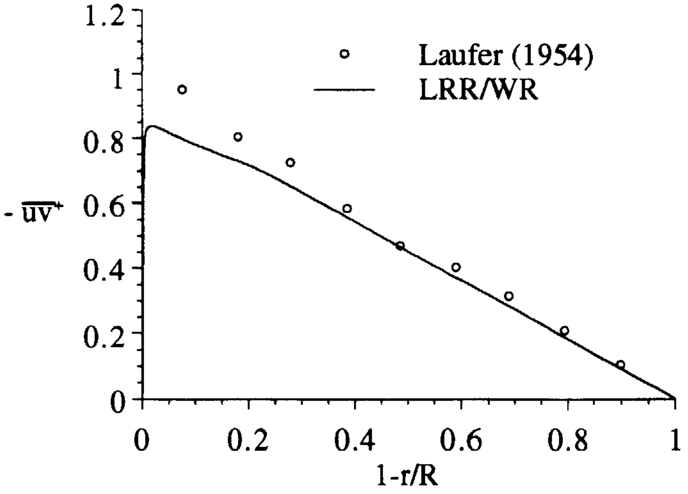

Fig. 19d Comparison of calculated $\overline{uv}^+$ with data.

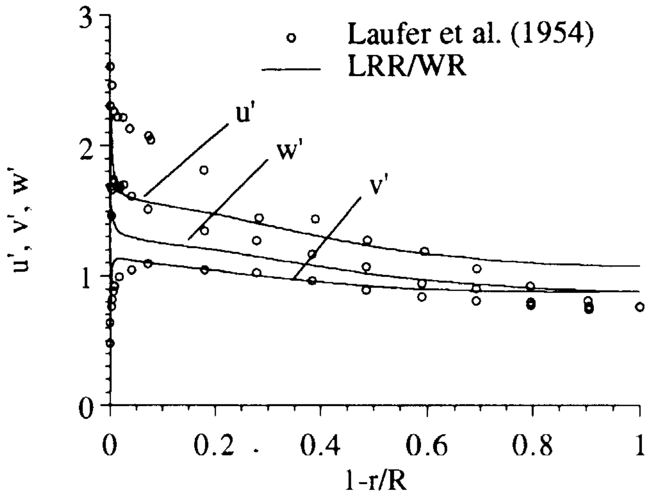

Fig. 19e Comparison of calculated normal stresses with data.

	Laufer (1954)	LRR/WR
κ	0.40	0.40
a_k	---	0.07
a_u^2/a_k	---	1.94
$a_v^2/a_k \times 10^3$	---	8.20
a_w^2/a_k	---	0.68
$a_{uv}/(a_u\ a_v)$	---	0.21
$(a_u^2+a_v^2+a_w^2)/a_k$	---	2.62

Table 19 Comparison of near-wall asymptotes with data.

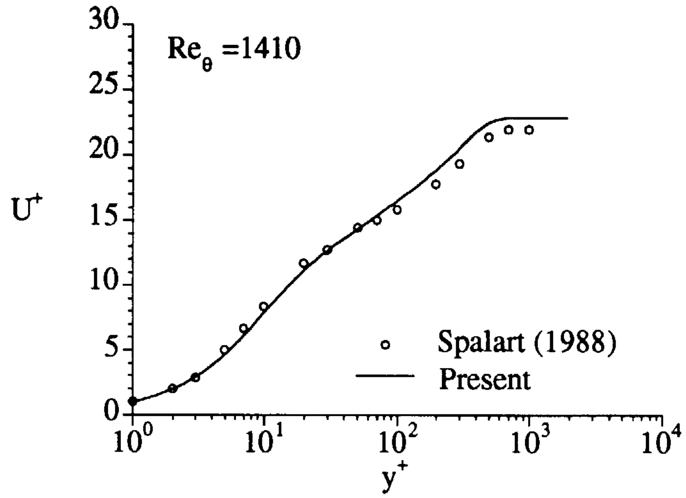

Fig. 20a Comparison of calculated U^+ with data.

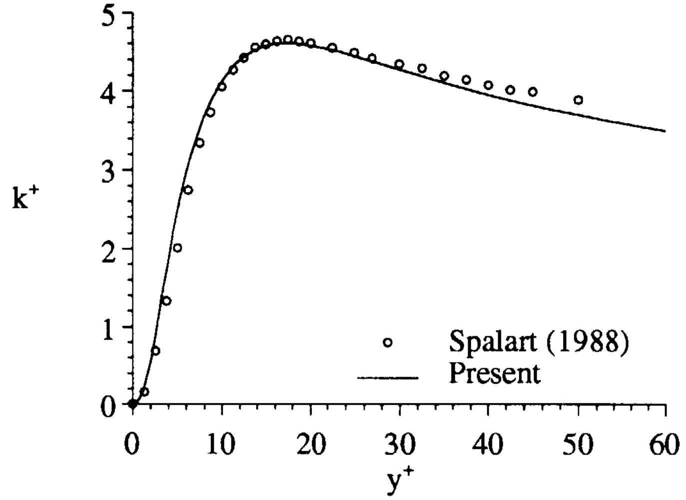

Fig. 20b Comparison of calculated k^+ with data.

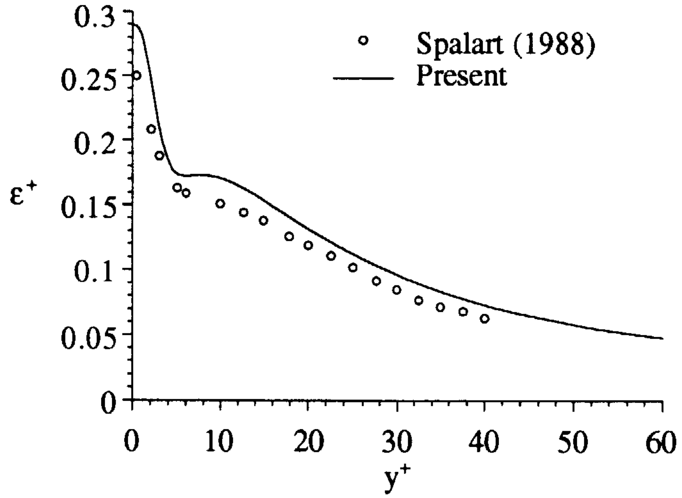

Fig. 20c Comparison of calculated ε^+ with data.

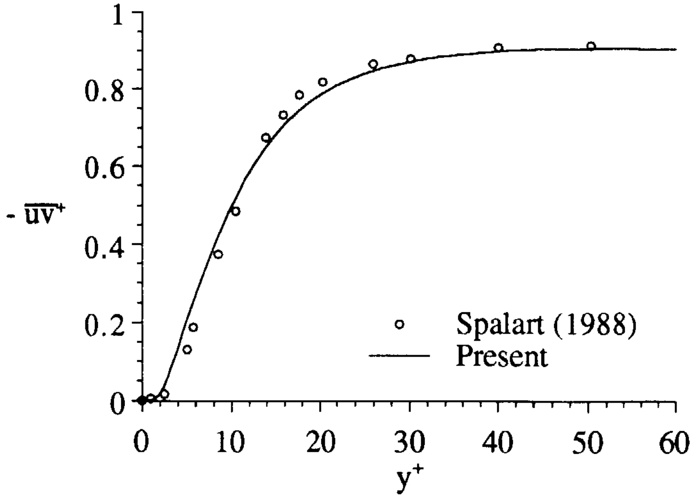

Fig. 20d Comparison of calculated $\overline{uv}^+$.

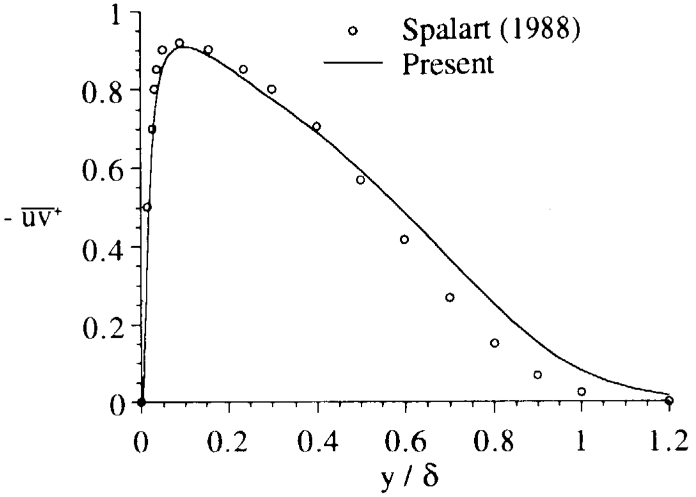

Fig. 20e Comparison of calculated $\overline{uv}^+$.

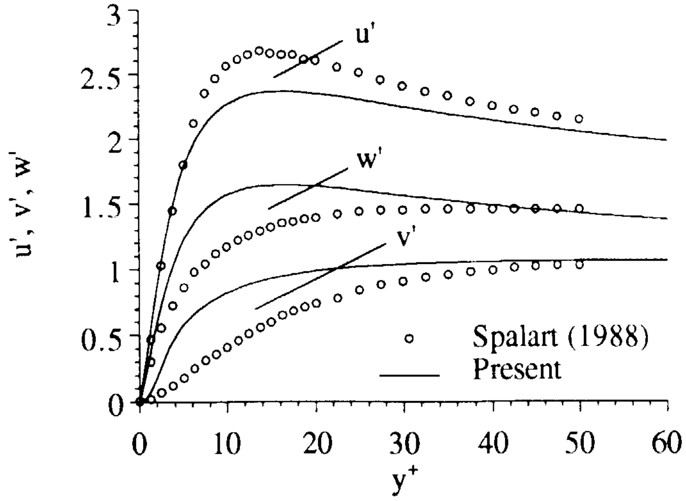

Fig. 20f Comparison of normal stresses with data - inner region.

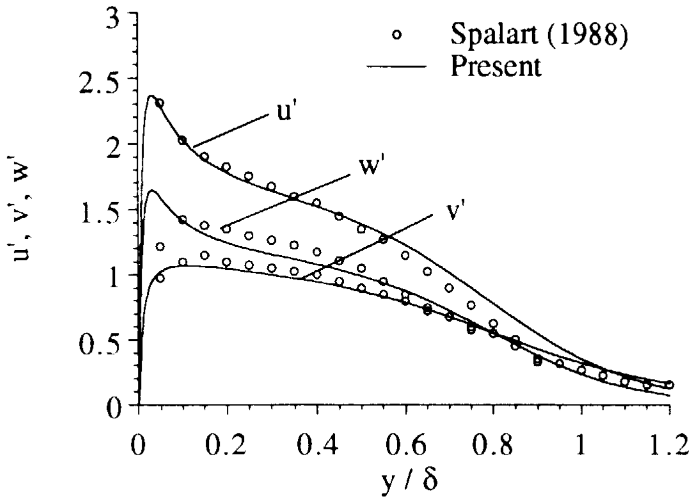

Fig. 20g Comparison of normal stresses with data - outer region.

	Spalart (1988)	Present
κ	0.41	0.38
$C_f \times 10^3$	4.1	3.84
a_k	0.13	0.144
a_u^2/a_k	1.43	1.36
$a_v^2/a_k \times 10^3$	0.8	21.4
a_w^2/a_k	0.58	0.64
$a_{uv}/(a_u\, a_v)$	0.27	0.057
$(a_u^2+a_v^2+a_w^2)/a_k$	2.01	2.02

Table 20 Comparison of near-wall asymptotes with data.

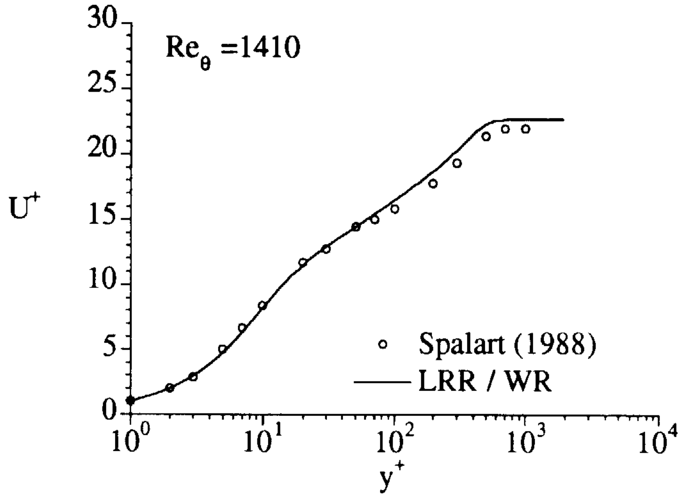

Fig. 21a Comparison of calculated U+ with data.

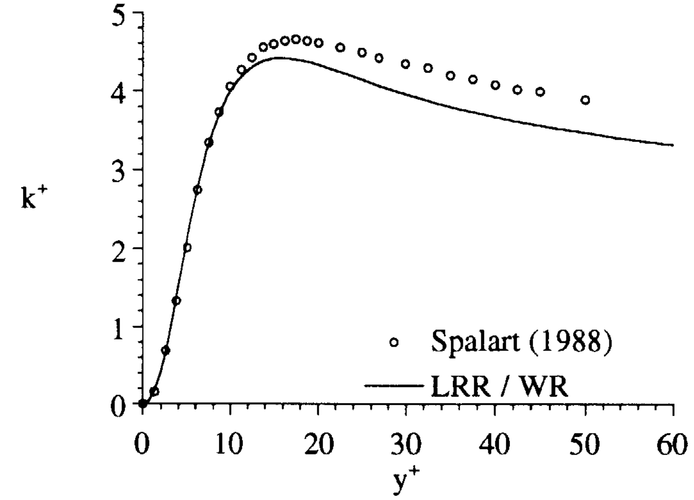

Fig. 21b Comparison of calculated k+ with data.

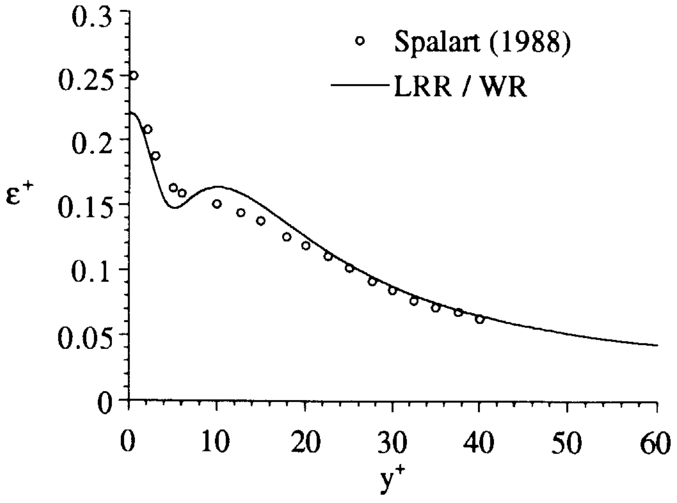

Fig. 21c Comparison of calculated ε+ with data.

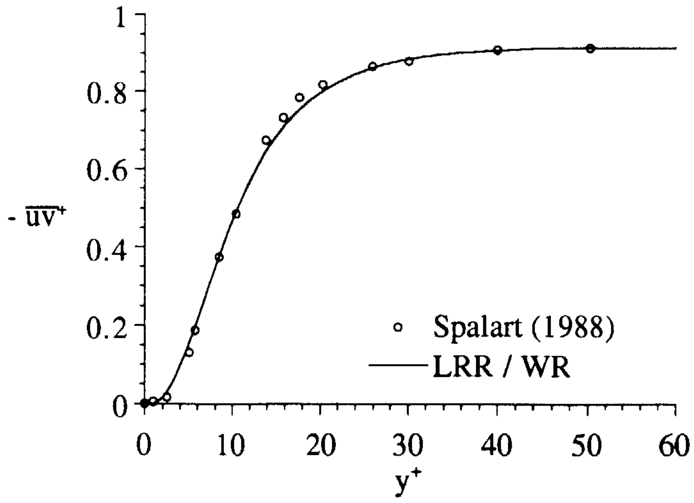

Fig. 21d Comparison of calculated $\overline{uv}^+$ with data.

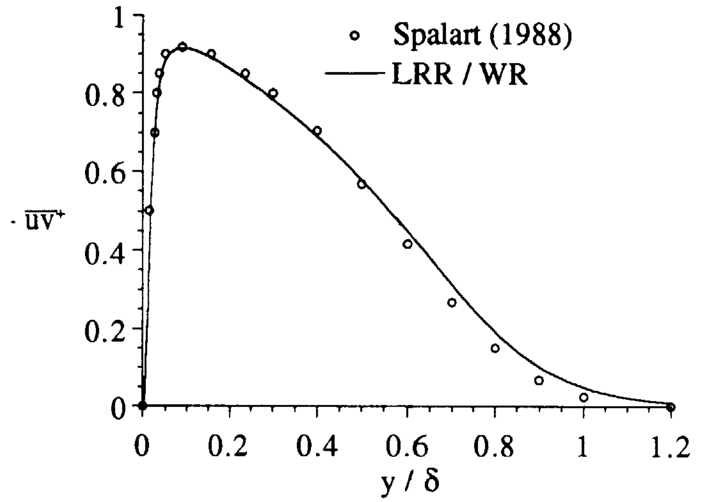

Fig. 21e Comparison of calculated $\overline{uv}^+$ with data.

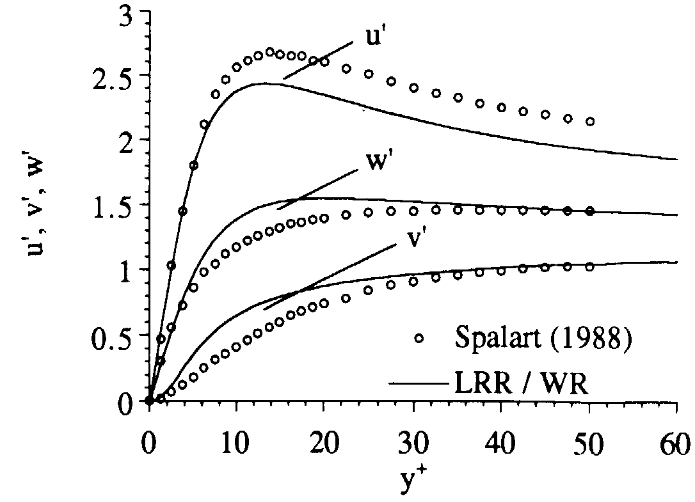

Fig. 21f Comparison of calculated normal stresses with data - outer region.

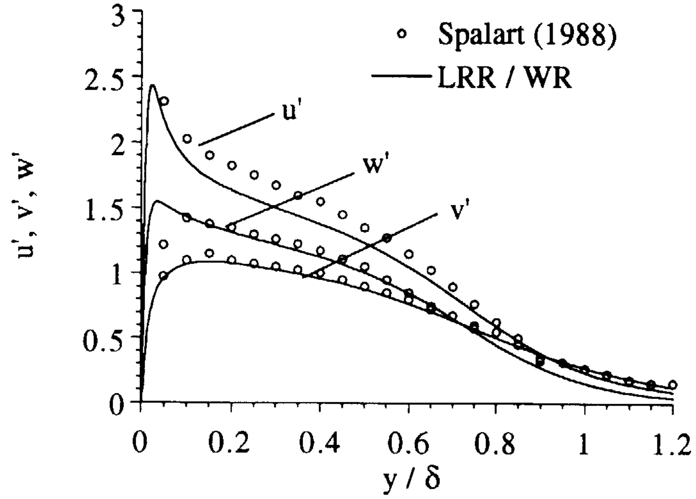

Fig. 21g Comparison of calculated normal stresses with data - outer region.

	Spalart (1988)	LRR / WR
κ	0.41	0.34
$C_f \times 10^3$	4.1	3.96
a_k	0.13	0.144
a_u^2/a_k	1.43	1.59
$a_v^2/a_k \times 10^3$	0.8	5.04
a_w^2/a_k	0.58	0.40
$a_{uv}/(a_u\, a_v)$	0.27	0.27
$(a_u^2+a_v^2+a_w^2)/a_k$	2.01	2.00

Table 21 Comparison of near-wall asymptotes with data.

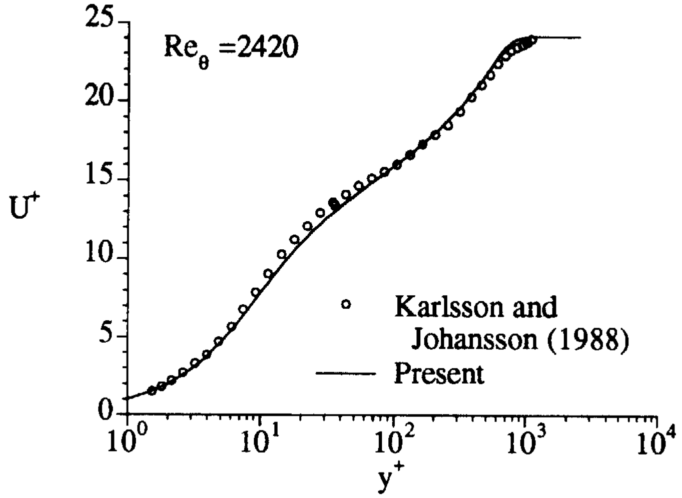

Fig. 22a Comparison of calculated U^+ with data.

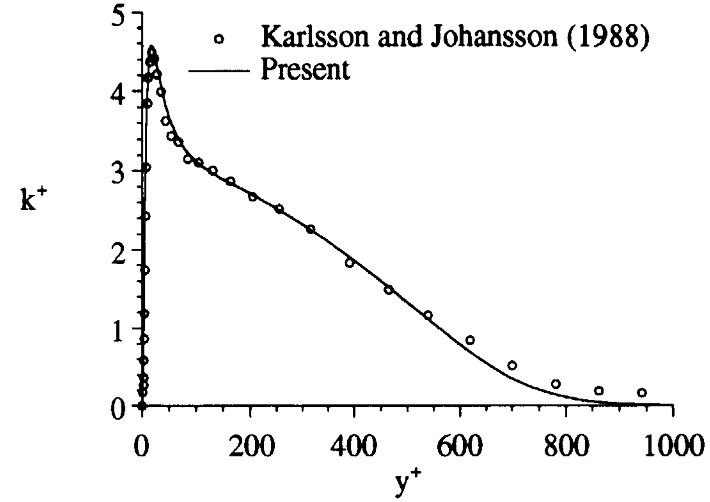

Fig. 22b Comparison of calculated k^+ with data.

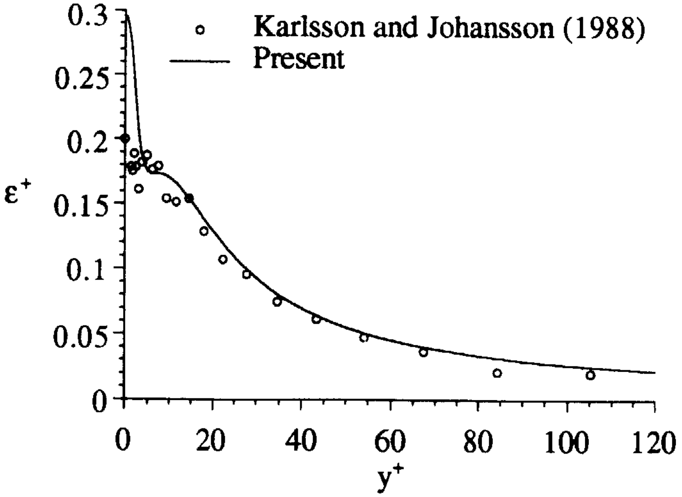

Fig. 22c Comparison of calculated ε^+ with data.

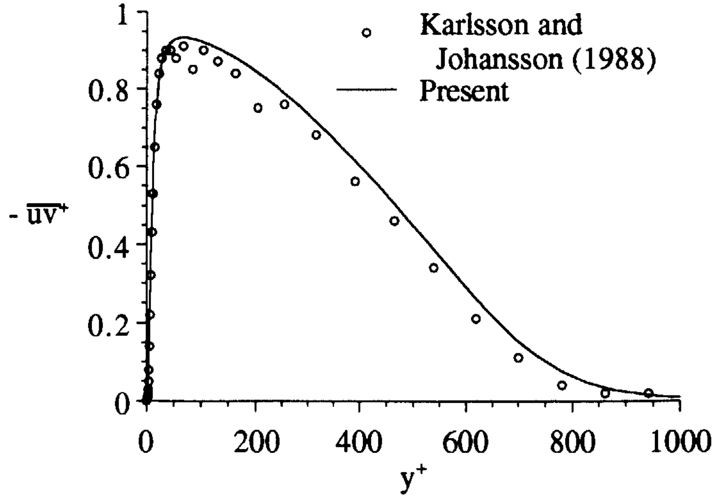

Fig. 22d Comparison of calculated $\overline{uv}^+$.

C-2.

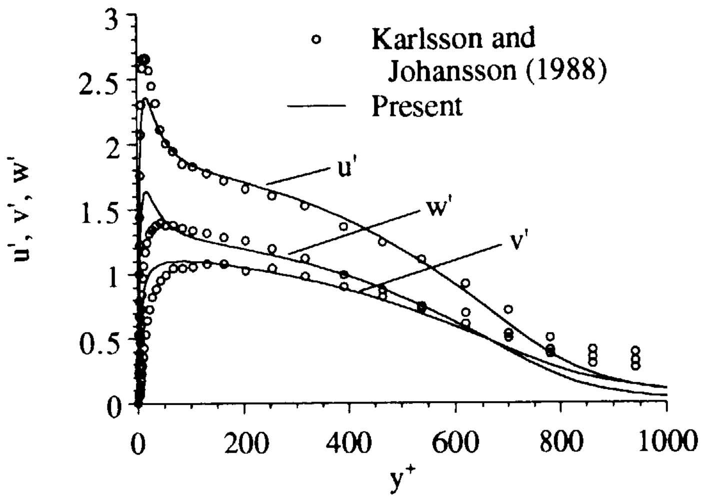

Fig. 22e Comparison of normal stresses with data.

	Karlsson and Johansson (1988)	Present
κ	0.41	0.36
$C_f \times 10^3$	3.54	3.44
a_k	0.13	0.148
a_u^2/a_k	1.72	1.36
$a_v^2/a_k \times 10^3$	2.0	21.3
a_w^2/a_k	0.31	0.64
$a_{uv}/(a_u\, a_v)$	0.33	0.068
$(a_u^2+a_v^2+a_w^2)/a_k$	2.03	2.02

Table 22 Comparison of near-wall asymptotes with data.

Table 24 Comparison of C_f and κ with data.

	Klebanoff (1954)	Present
κ	0.43	0.40
$C_f \times 10^3$	2.81	2.84

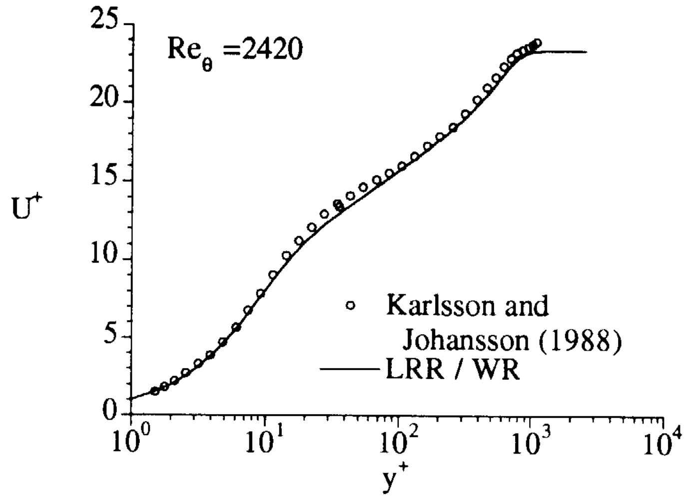

Fig. 23a Comparison of calculated U^+ with data.

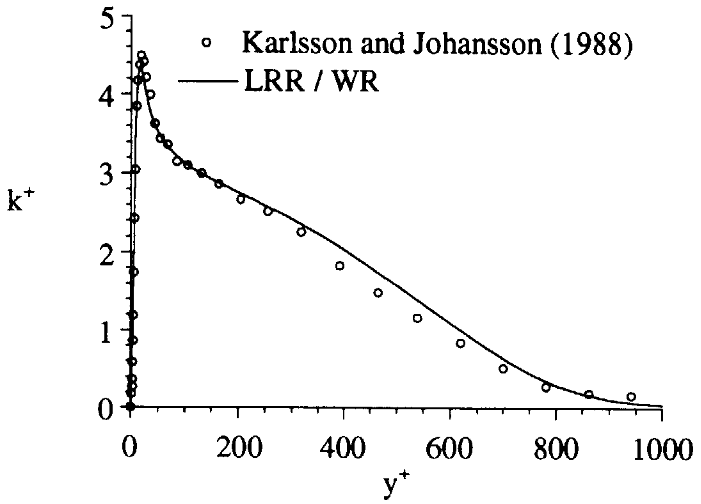

Fig. 23b Comparison of calculated k^+ with data.

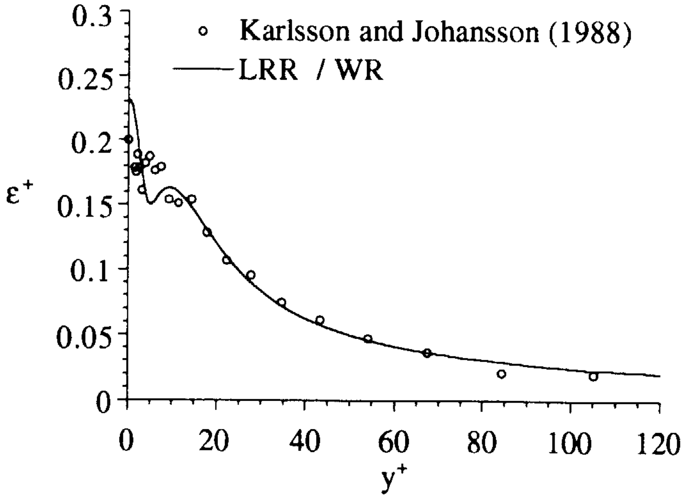

Fig. 23c Comparison of calculated ε^+ with data.

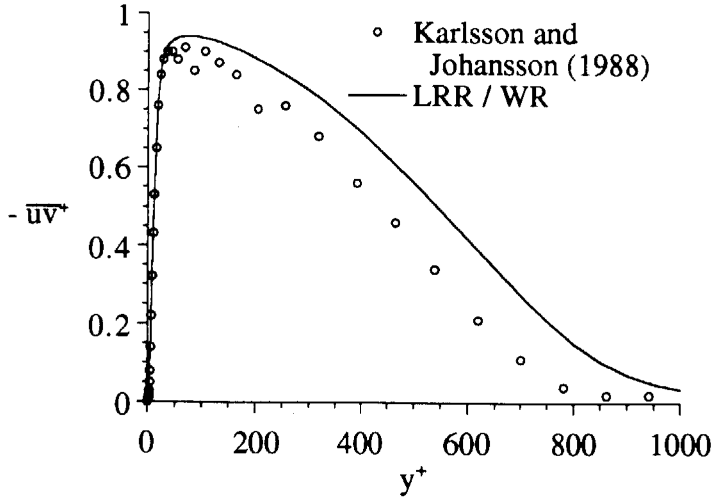

Fig. 23d Comparison of calculated $\overline{uv}^+$ with data.

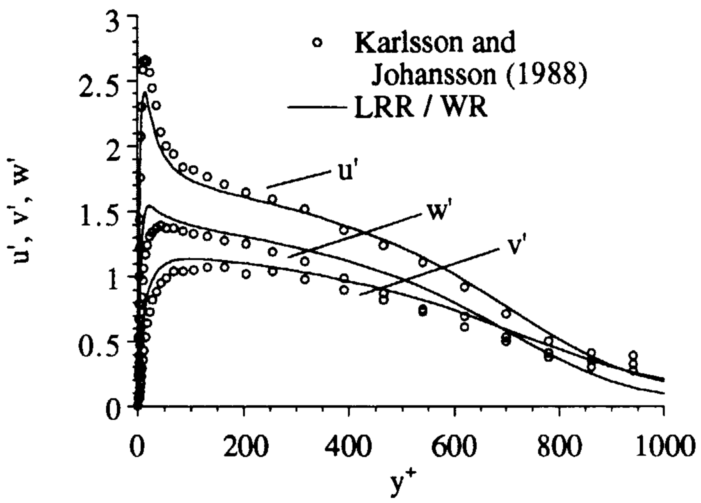

Fig. 23e Comparison of normal stresses with data.

	Karlsson and Johansson (1988)	LRR / WR
κ	0.41	0.40
$C_f \times 10^3$	3.54	3.63
a_k	0.13	0.116
a_u^2/a_k	1.72	1.59
$a_v^2/a_k \times 10^3$	2.0	5.18
a_w^2/a_k	0.31	0.42
$a_{uv}/(a_u\, a_v)$	0.33	0.28
$(a_u^2+a_v^2+a_w^2)/a_k$	2.03	2.01

Table 23 Comparison of near-wall asymptotes with data.

Table 25 Comparison of C_f and κ with data.

	Klebanoff (1954)	Present
κ	0.43	0.41
$C_f \times 10^3$	2.81	2.77

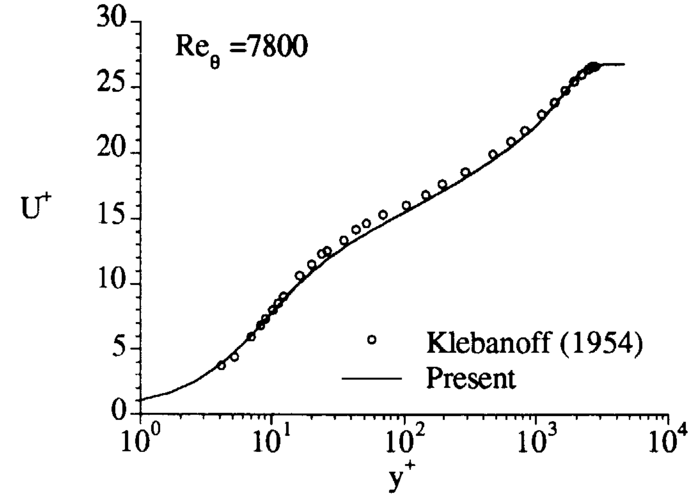

Fig. 24a Comparison of calculated U^+ with data.

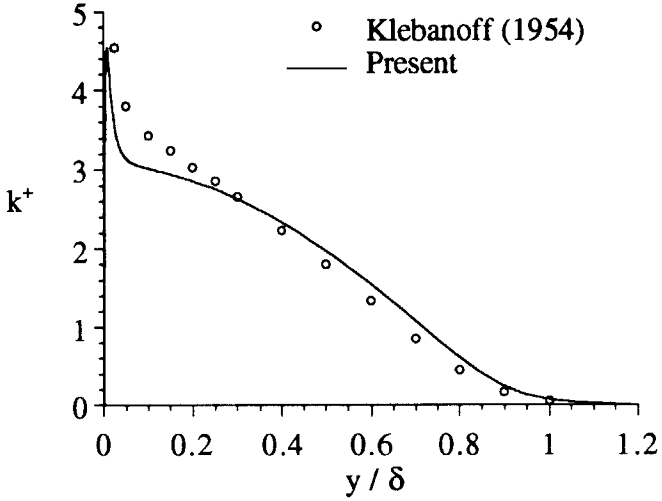

Fig. 24b Comparison of calculated k^+ with data.

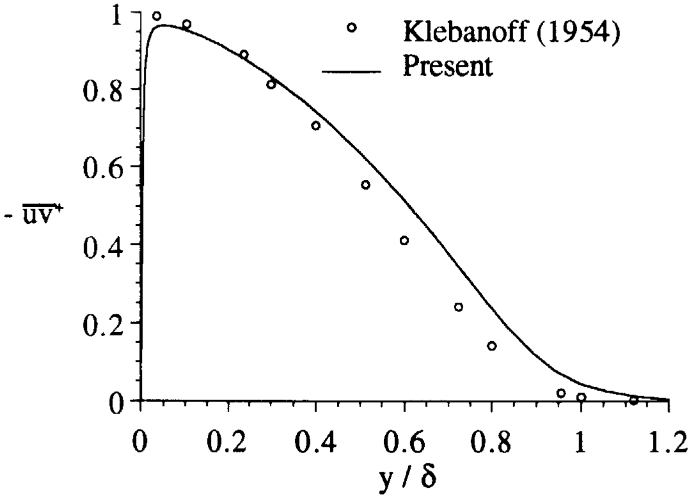

Fig. 24d Comparison of calculated $\overline{uv}^+$.

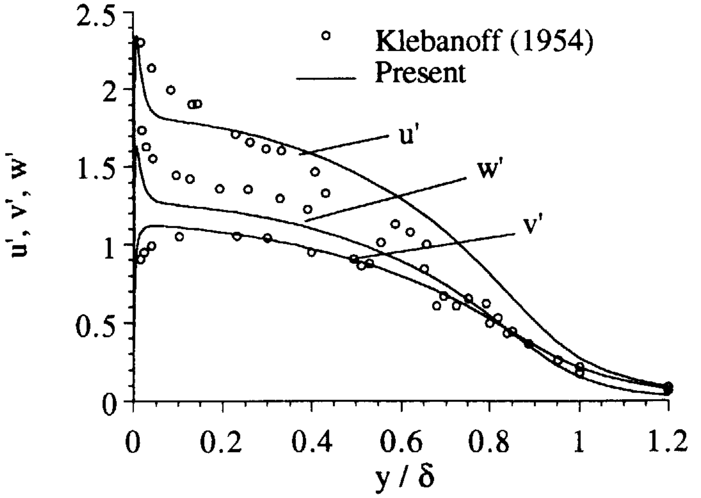

Fig. 24e Comparison of normal stresses with data.

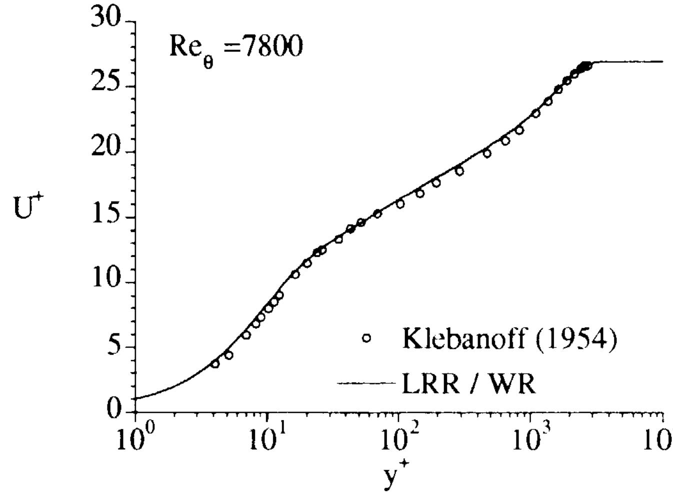

Fig. 25a Comparison of calculated U+ with data.

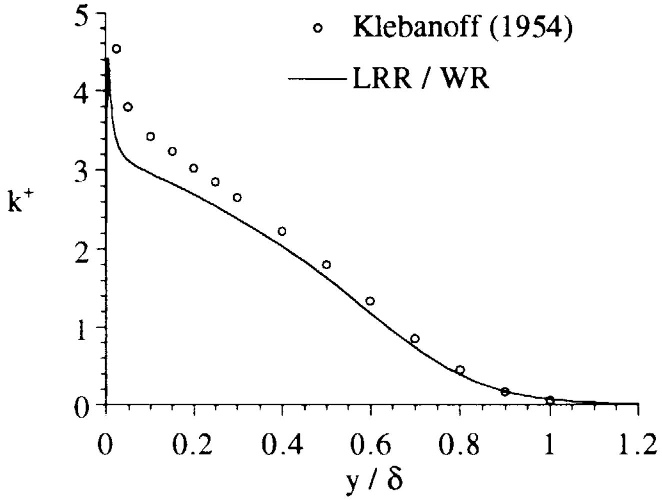

Fig. 25b Comparison of calculated k+ with data.

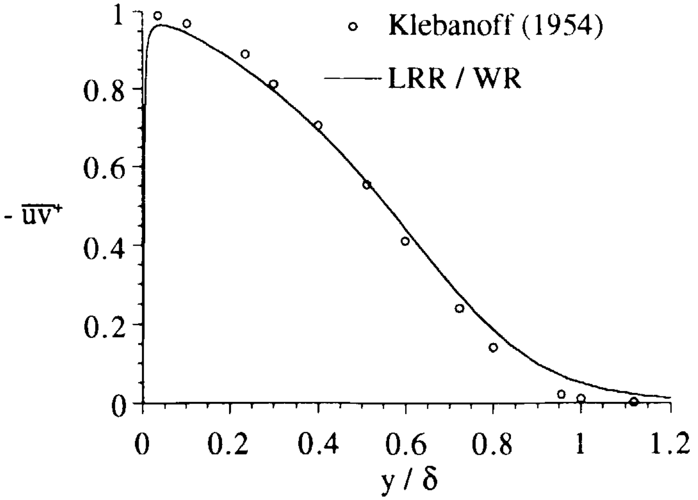

Fig. 25c Comparison of calculated $\overline{uv}^+$ with data.

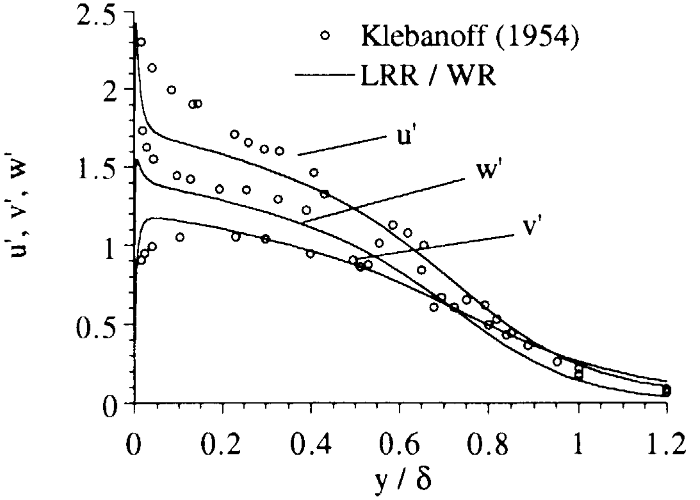

Fig. 25d Comparison of normal stresses with data.

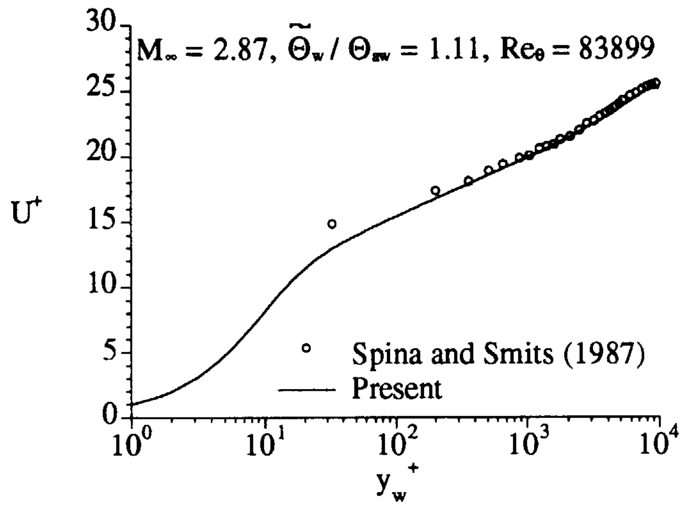

Fig. 26a Comparison of calculated U+ with data.

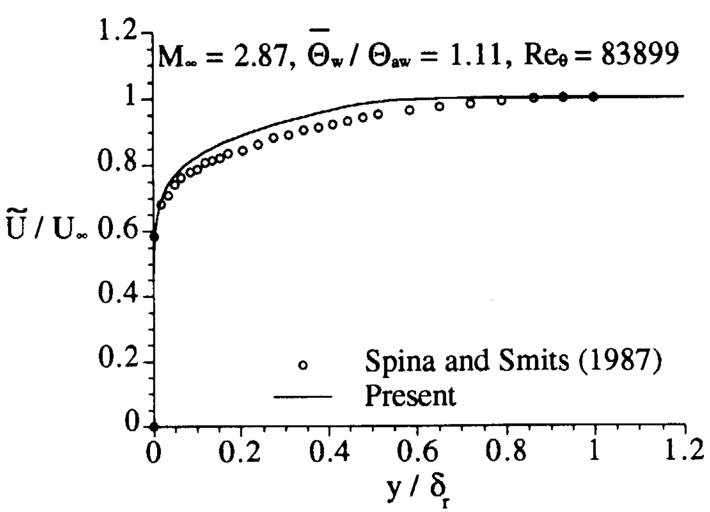

Fig. 26b Comparison of calculated mean U with data.

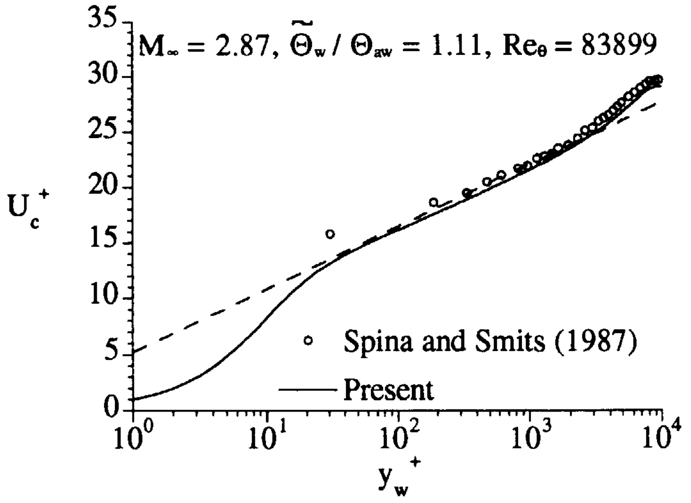

Fig. 26c Comparison of calculated U_c^+ with data.

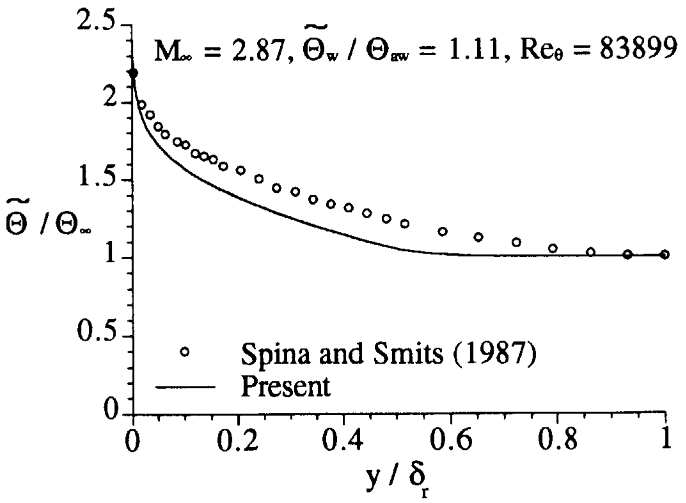

Fig. 26d Comparison of calculated mean Θ with data.

Table 26. Comparisons of the calculated and measured C_f and κ.

M_∞	Θ_w / Θ_{aw}	Re_θ	$C_f x 10^3$			κ			κ_c		
			Data	Present model	LRR/WR	Data	Present model	LRR/WR	Data	Present model	LRR/WR
2.87	1.11	83,899	1.10	1.15	1.14	0.52	0.51	0.49	0.37	0.35	0.38
2.24	1.0	20,797	1.62	1.65	1.69	0.41	0.41	0.44	0.38	0.38	0.38
4.54	1.0	5,320	1.26	1.18	1.32	0.41	0.41	0.42	0.28	0.29	0.30
10.31	1.0	15,074	0.24	0.20	0.24	0.54	0.58	0.54	0.28	0.29	0.29
5.29	0.92	3,936	1.31	1.12	1.22	0.48	0.44	0.40	0.34	0.29	0.26
8.18	0.3	4,600	0.98	1.05	0.96	0.35	0.40	0.31	0.29	0.28	0.29

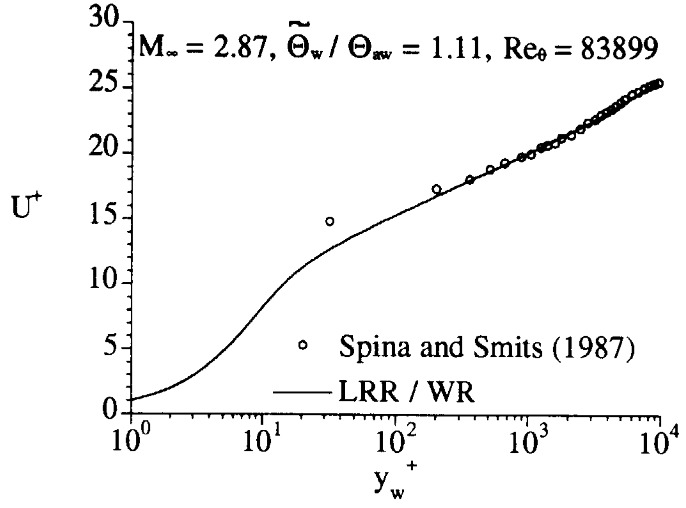

Fig. 27a Comparison of calculated U+ with data.

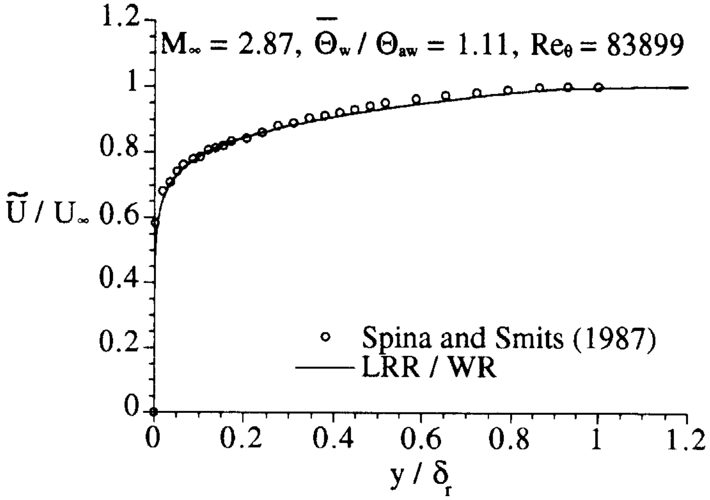

Fig. 27b Comparison of calculated mean U with data.

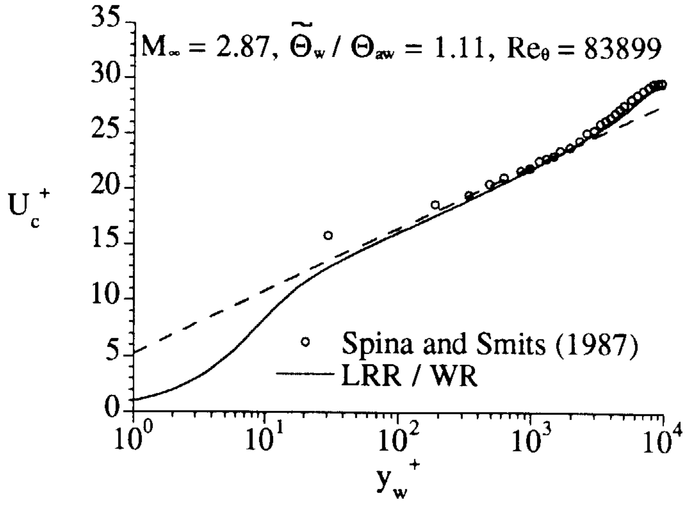

Fig. 27c Comparison of calculated U_c^+ with data.

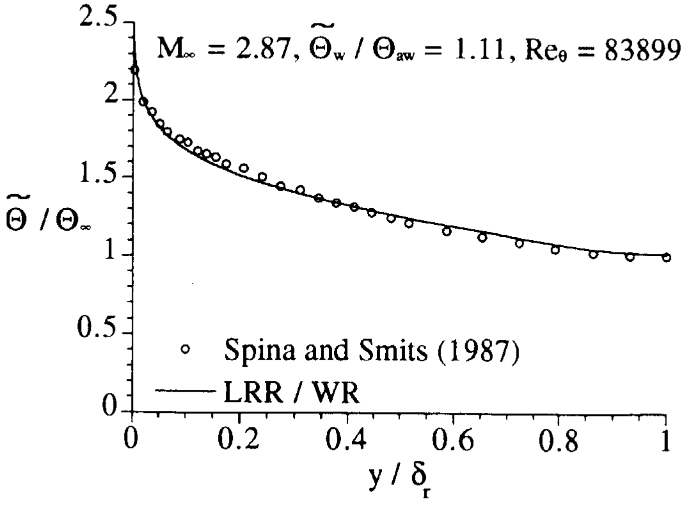

Fig. 27d Comparison of calculated mean Θ with data.

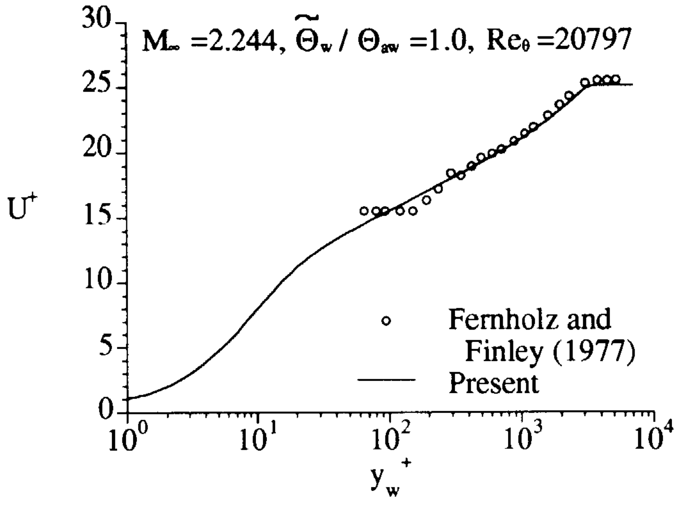

Fig. 28a Comparison of calculated U^+ with data.

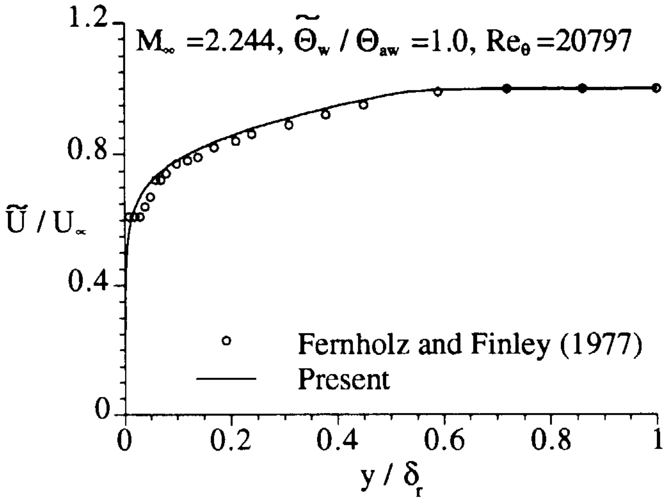

Fig. 28b Comparison of calculated mean U with data.

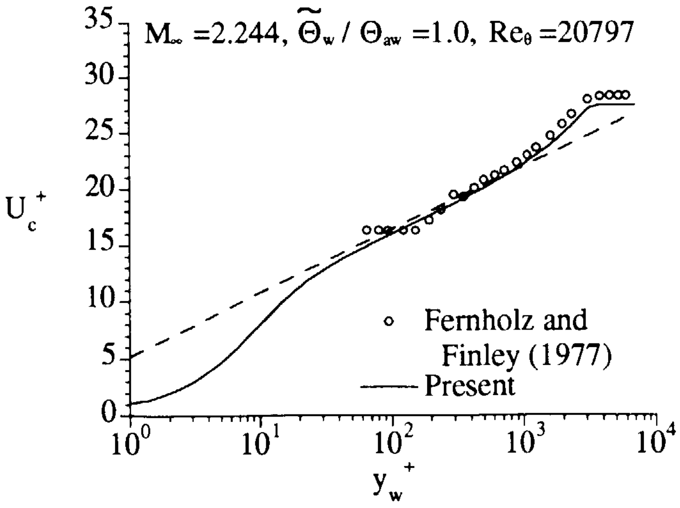

Fig. 28c Comparison of calculated U_c^+ with data.

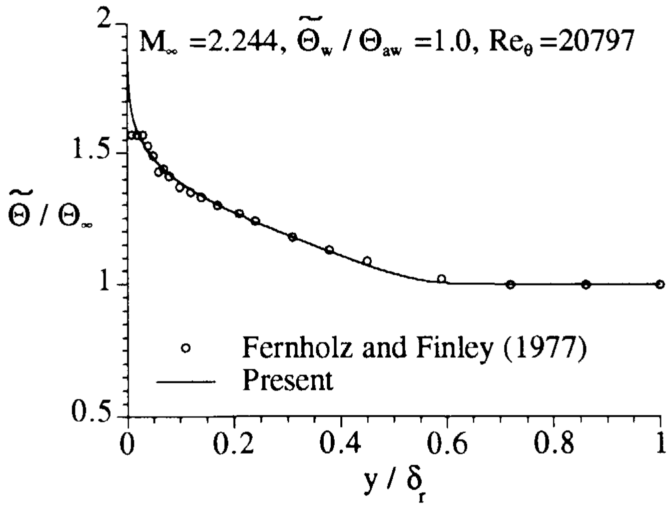

Fig. 28d Comparison of calculated mean Θ with data.

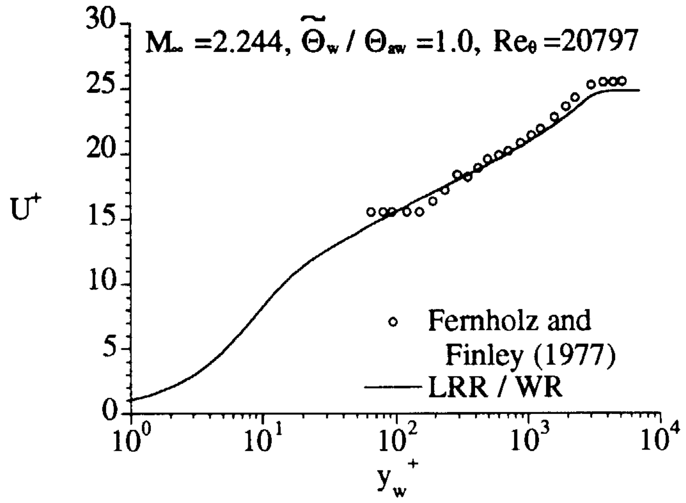

Fig. 29a Comparison of calculated U+ with data.

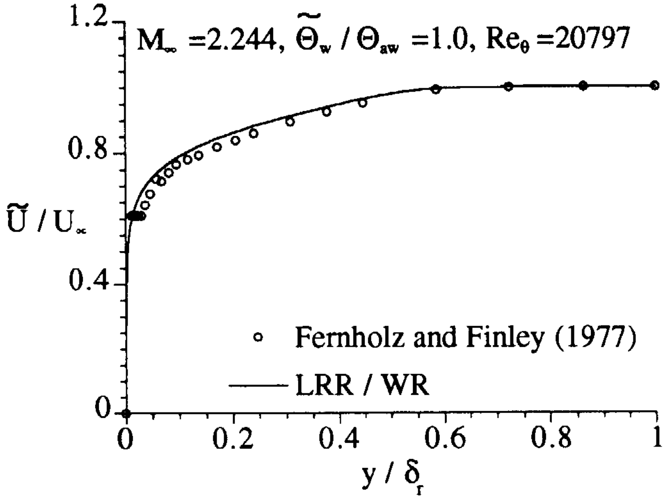

Fig. 29b Comparison of calculated mean U with data.

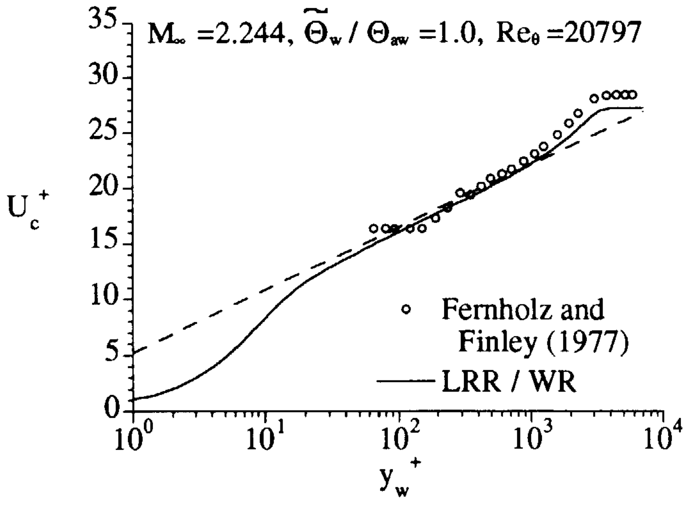

Fig. 29c Comparison of calculated U_c^+ with data.

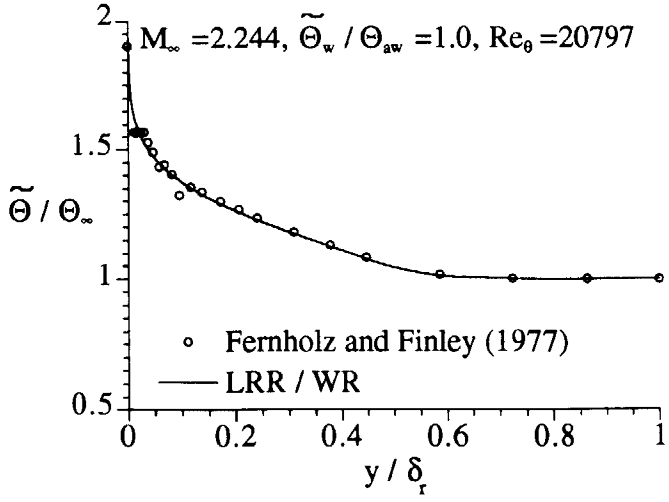

Fig. 29d Comparison of calculated mean Θ with data.

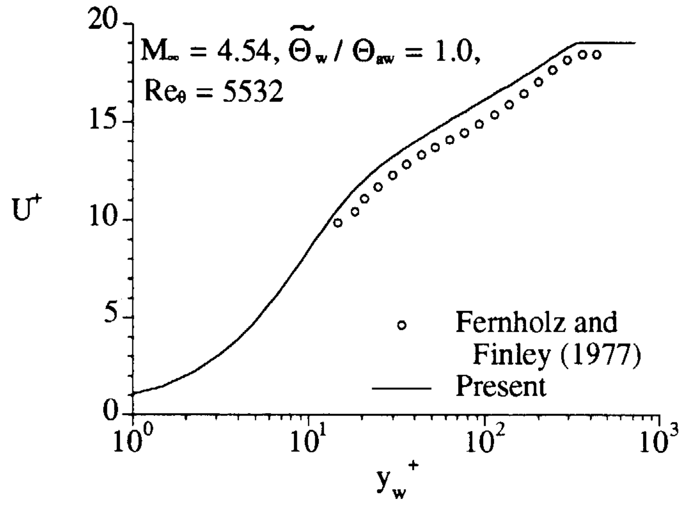

Fig. 30a Comparison of calculated U+ with data.

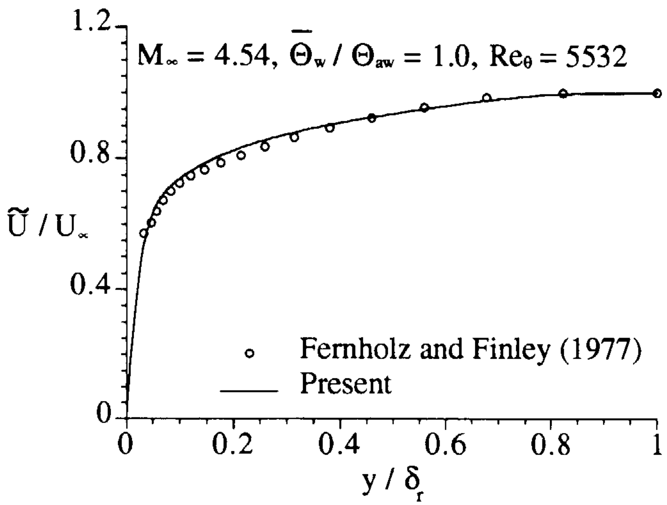

Fig. 30b Comparison of calculated mean U with data.

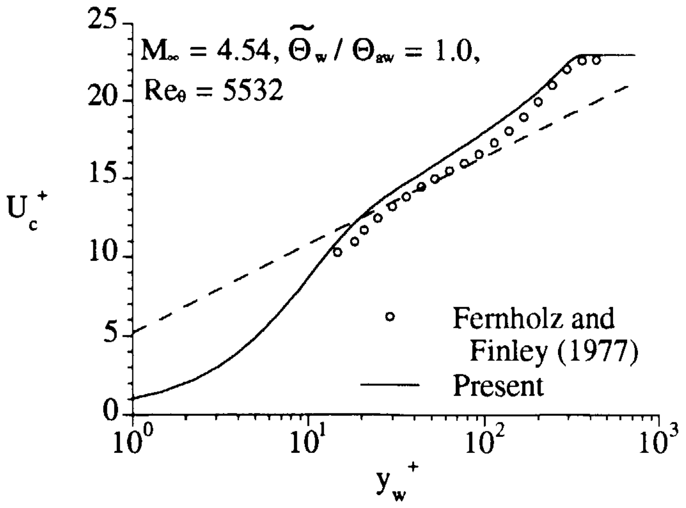

Fig. 30c Comparison of calculated U_c^+ with data.

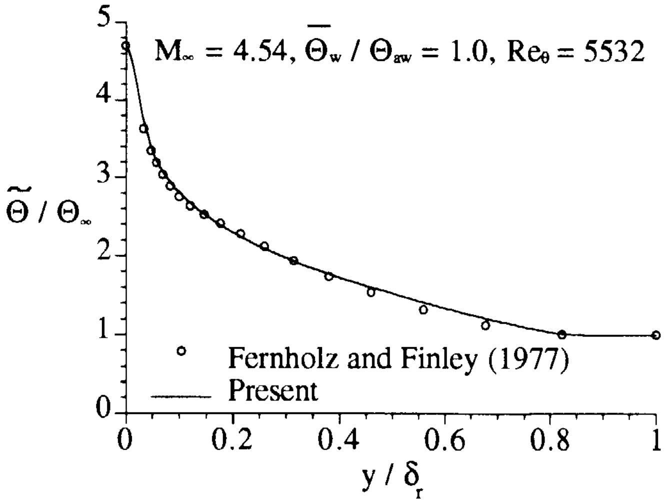

Fig. 30d Comparison of calculated mean Θ with data.

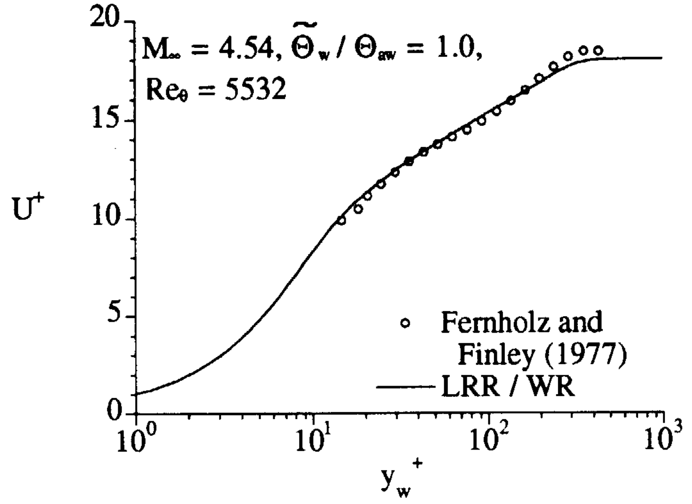

Fig. 31a Comparison of calculated U^+ with data.

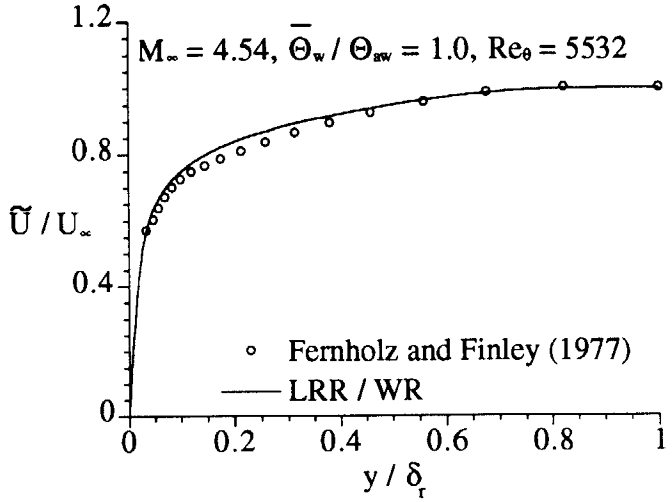

Fig. 31b Comparison of calculated mean U with data.

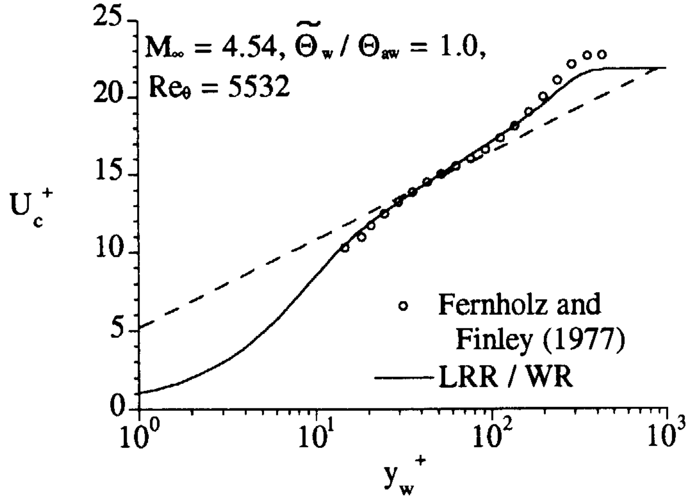

Fig. 31c Comparison of calculated U_c^+ with data.

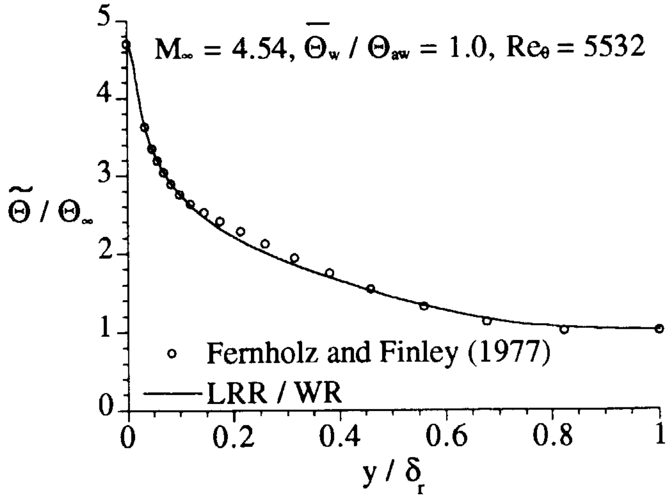

Fig. 31d Comparison of calculated mean Θ with data.

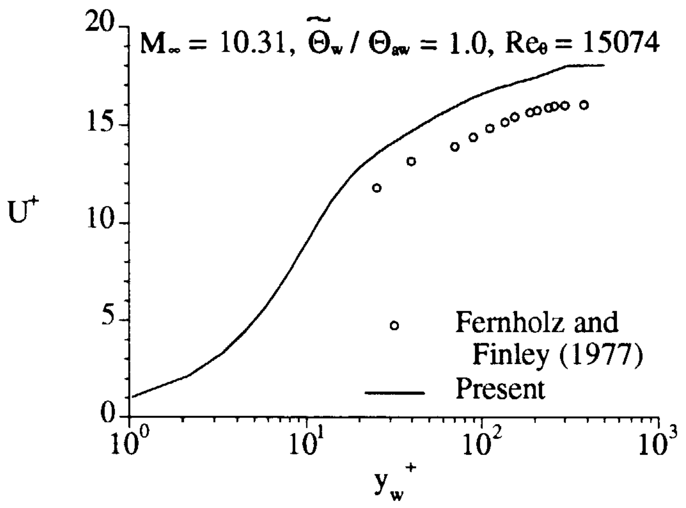

Fig. 32a Comparison of calculated U+ with data.

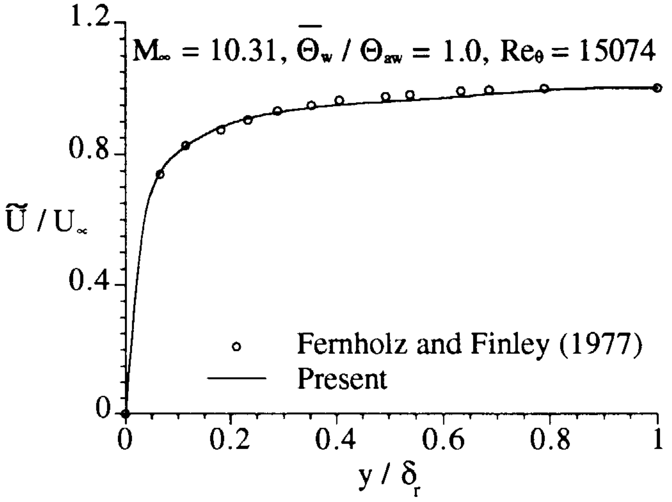

Fig. 32b Comparison of calculated mean U with data.

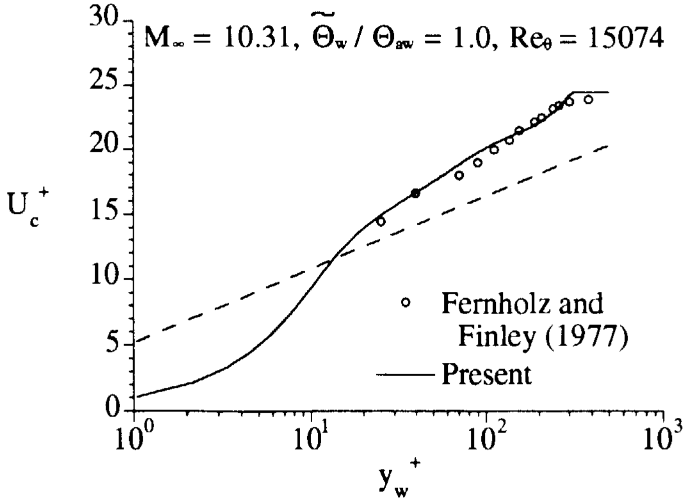

Fig. 32c Comparison of calculated U_c^+ with data.

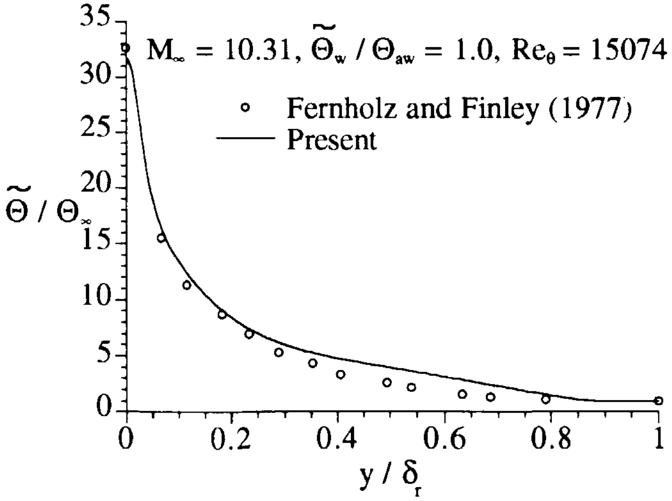

Fig. 32d Comparison of calculated mean Θ with data.

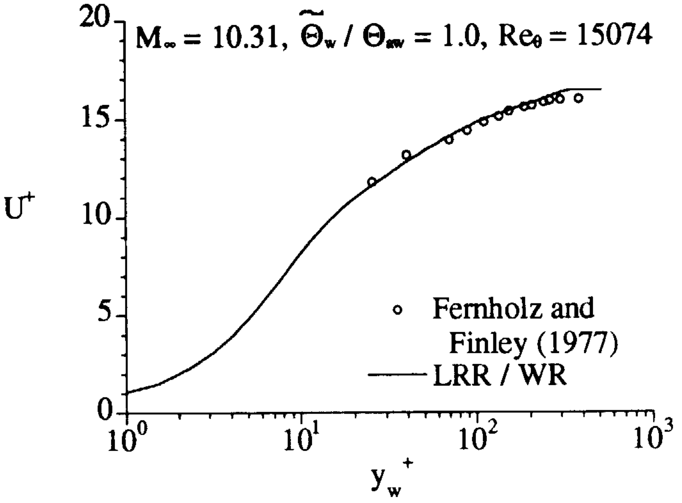

Fig. 33a Comparison of calculated U^+ with data.

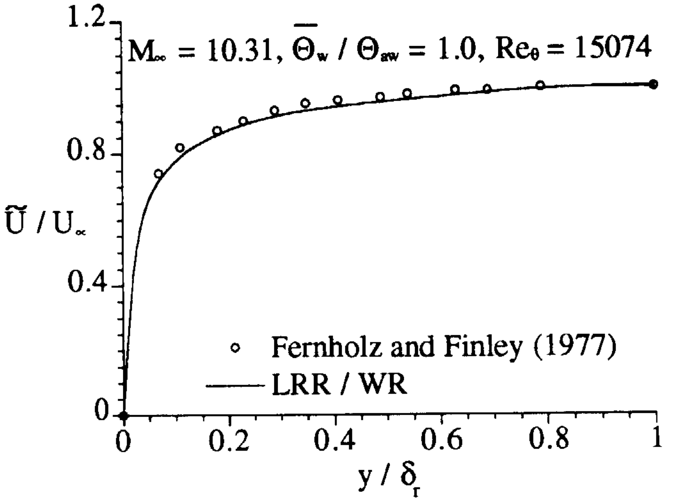

Fig. 33b Comparison of calculated mean U with data.

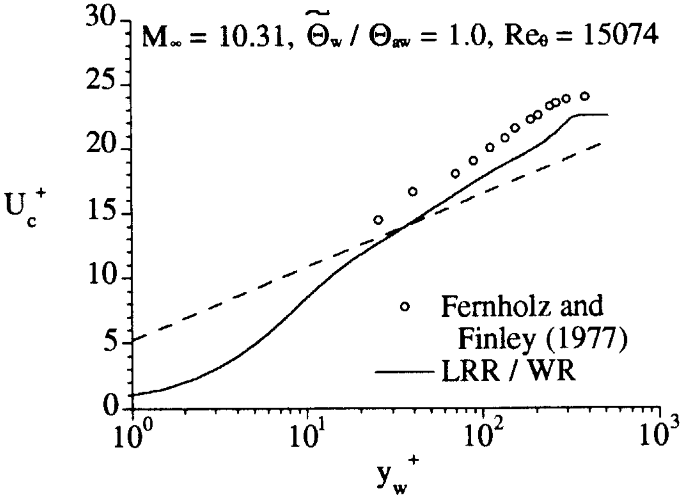

Fig. 33c Comparison of calculated U_c^+ with data.

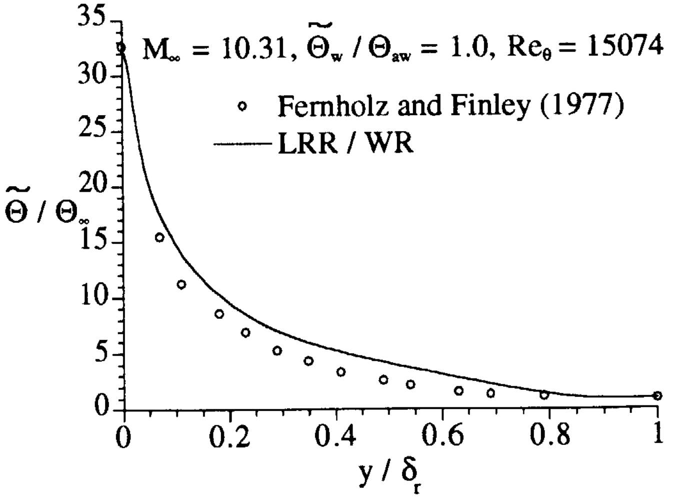

Fig. 33d Comparison of calculated mean Θ with data.

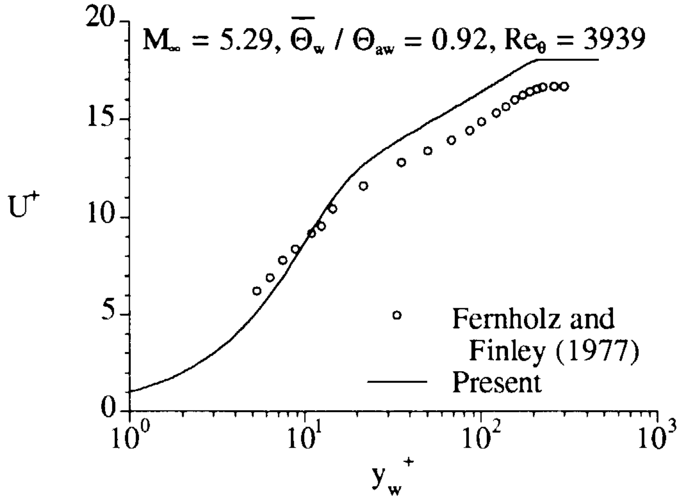

Fig. 34a Comparison of calculated U^+ with data.

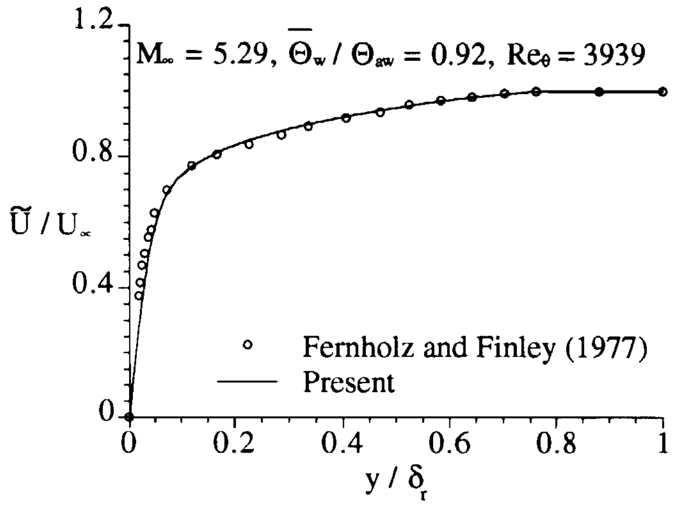

Fig. 34b Comparison of calculated mean U with data.

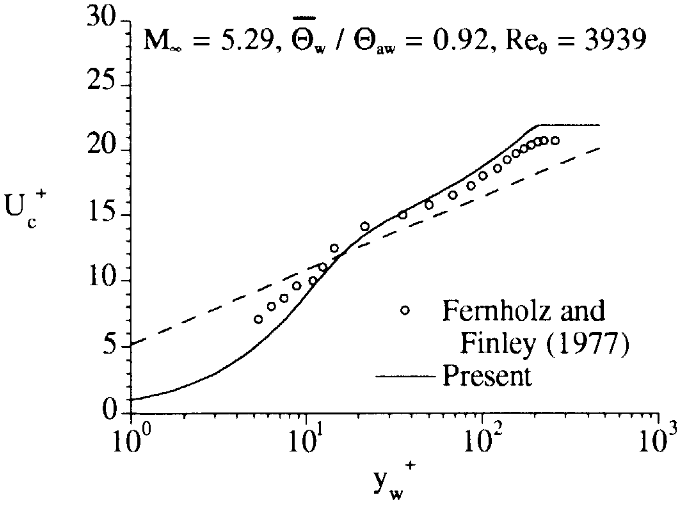

Fig. 34c Comparison of calculated U_c^+ with data.

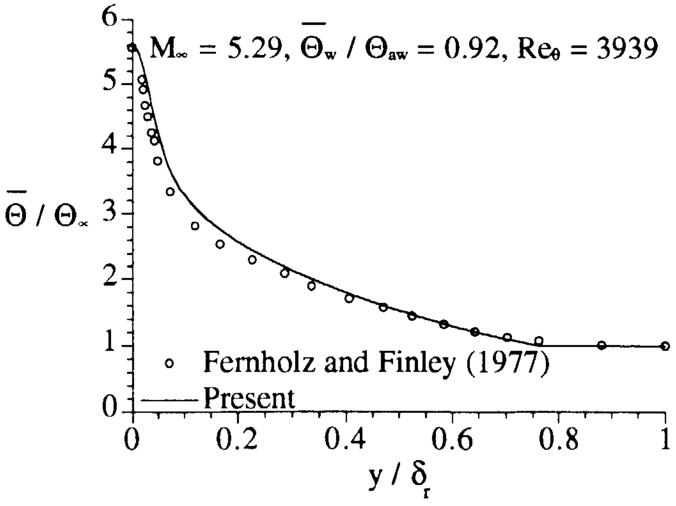

Fig. 34d Comparison of calculated mean Θ with data.

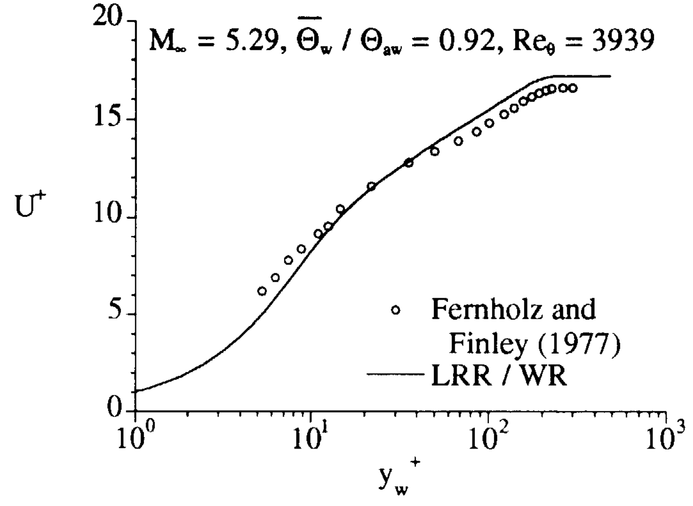

Fig. 35a Comparison of calculated U+ with data.

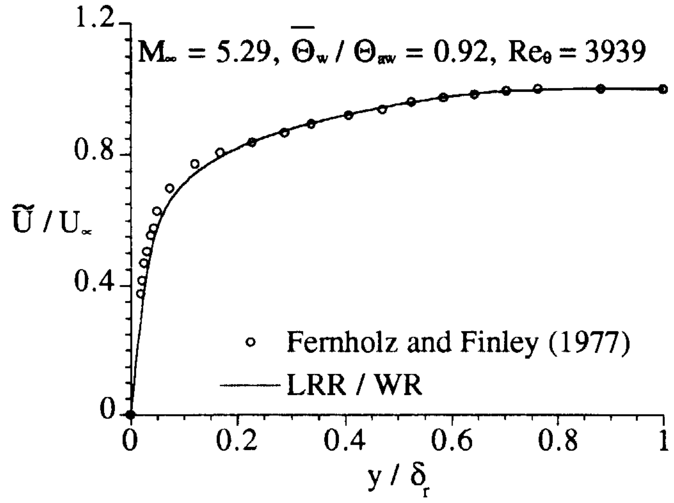

Fig. 35b Comparison of calculated mean U with data.

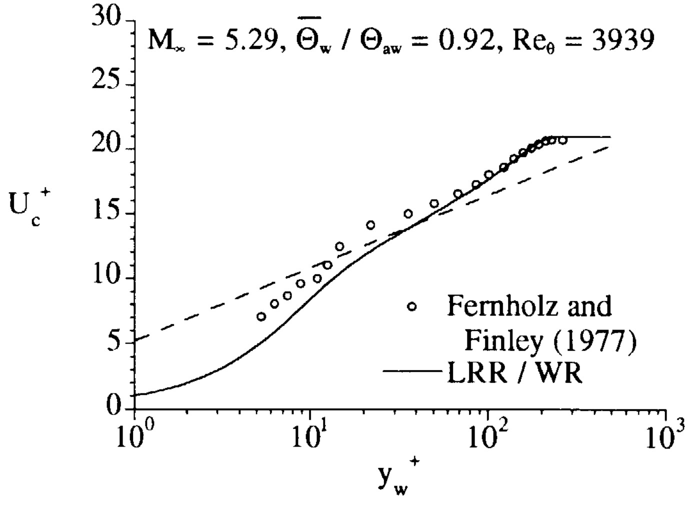

Fig. 35c Comparison of calculated U_c^+ with data.

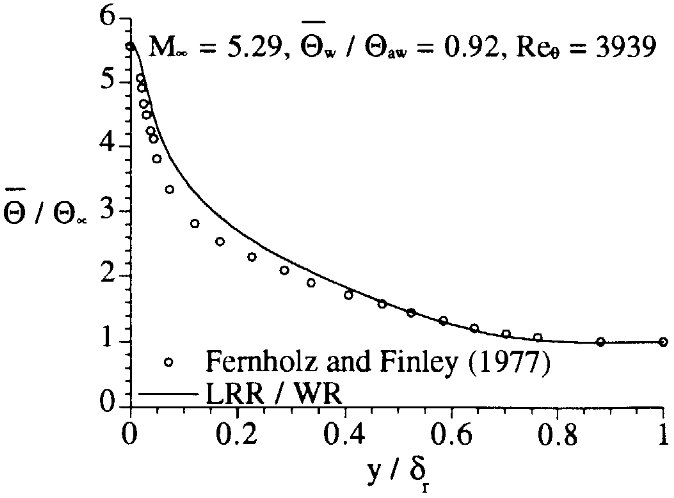

Fig. 35d Comparison of calculated mean Θ with data.

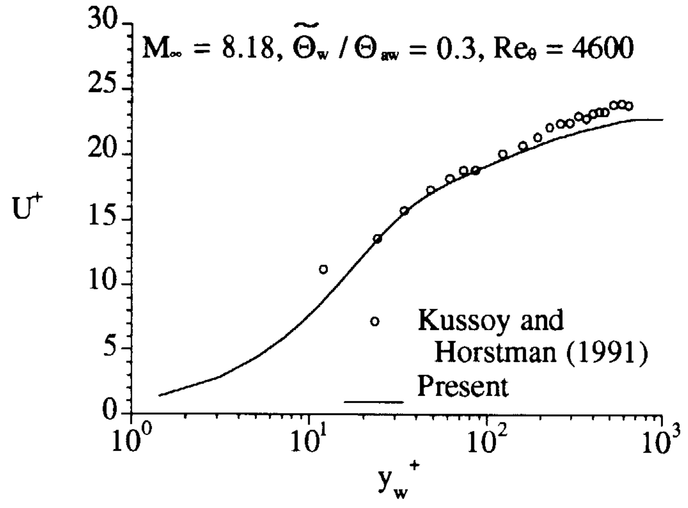

Fig. 36a Comparison of calculated U^+ with data.

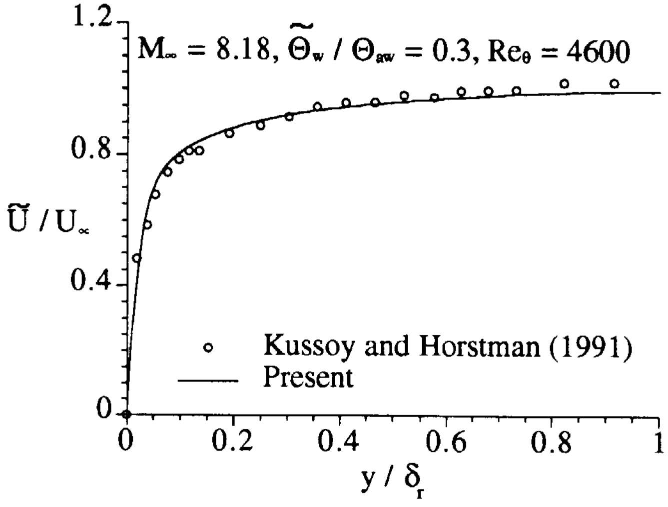

Fig. 36b Comparison of calculated mean U with data.

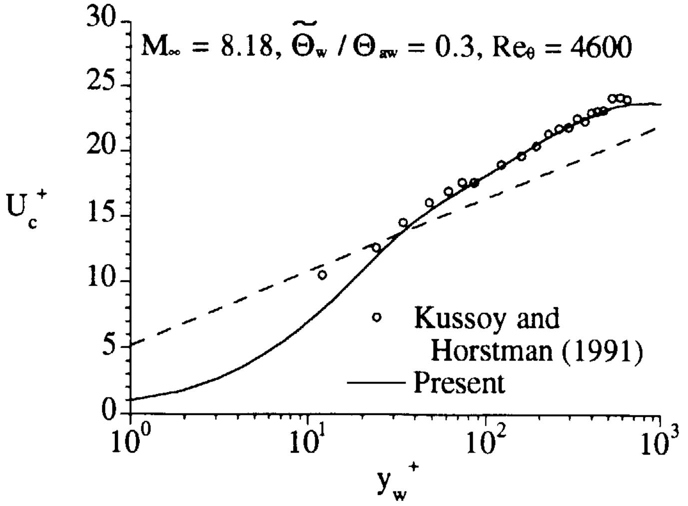

Fig. 36c Comparison of calculated U_c^+ with data.

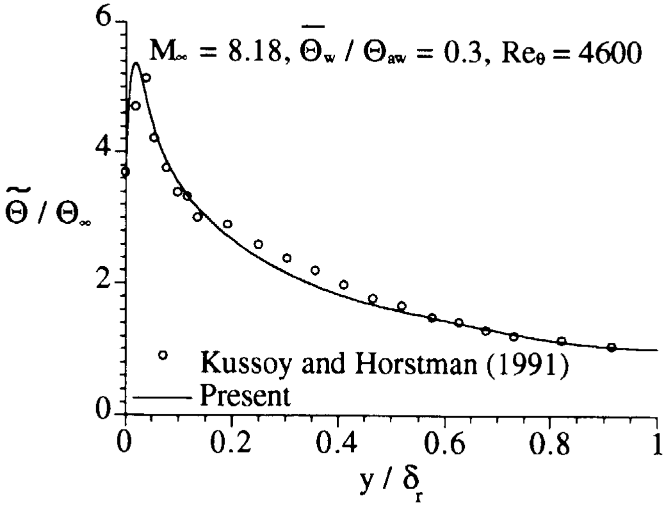

Fig. 36d Comparison of calculated mean Θ with data.

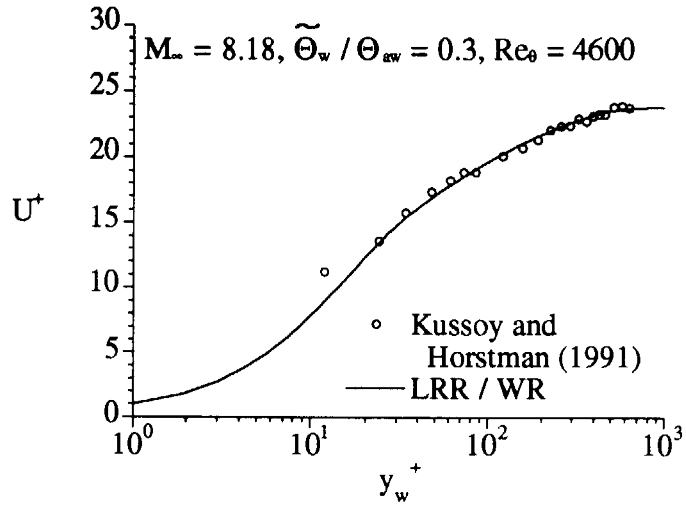

Fig. 37a Comparison of calculated U^+ with data.

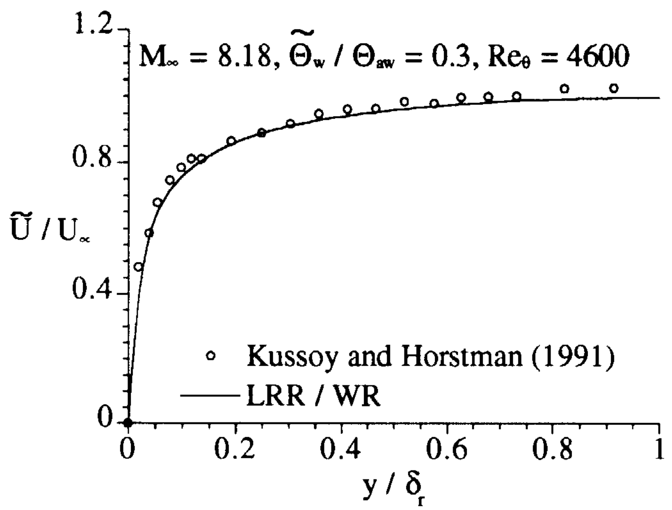

Fig. 37b Comparison of calculated mean U with data.

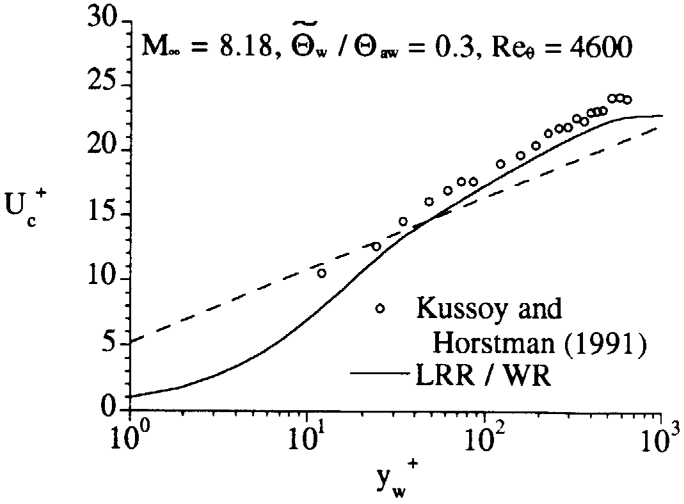

Fig. 37c Comparison of calculated U_c^+ with data.

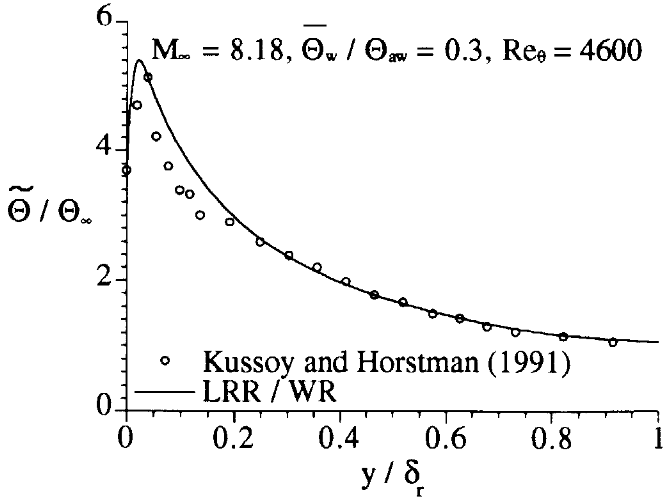

Fig. 37d Comparison of calculated mean Θ with data.

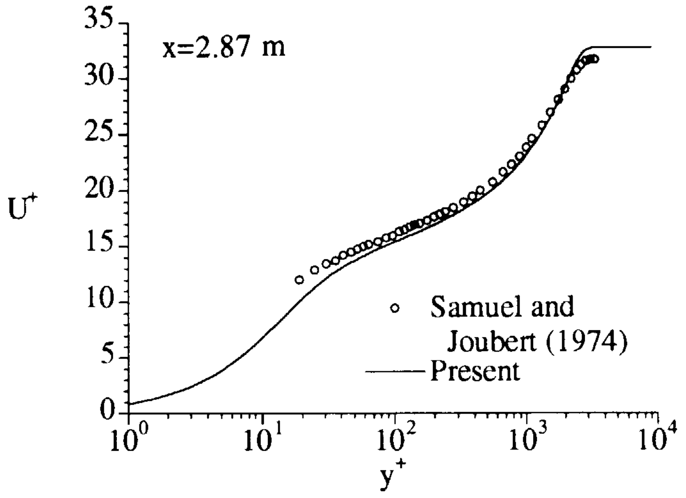

Fig. 38a Comparison of U+ with data at x = 2.87m.

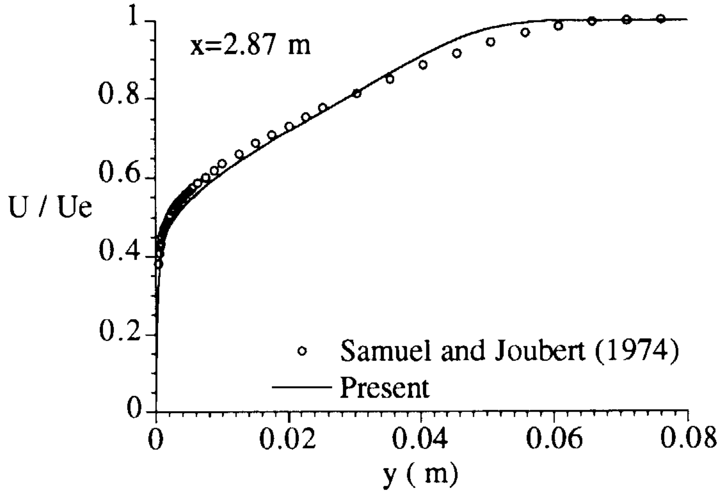

Fig. 38b Comparison of U with data at x = 2.87m.

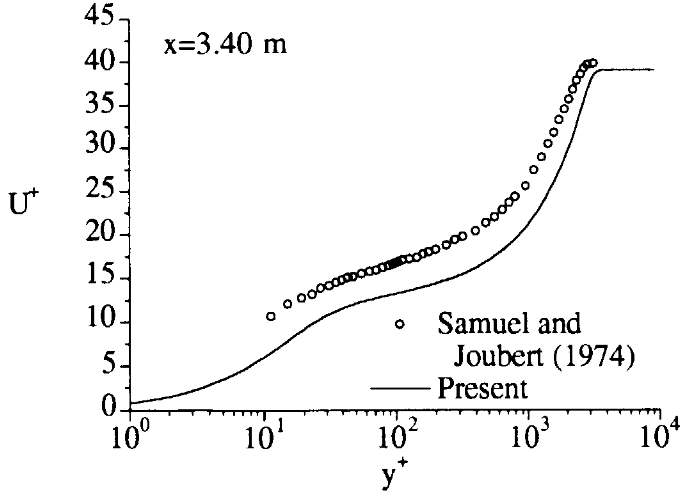

Fig. 38c Comparison of U+ with data at x = 3.40m.

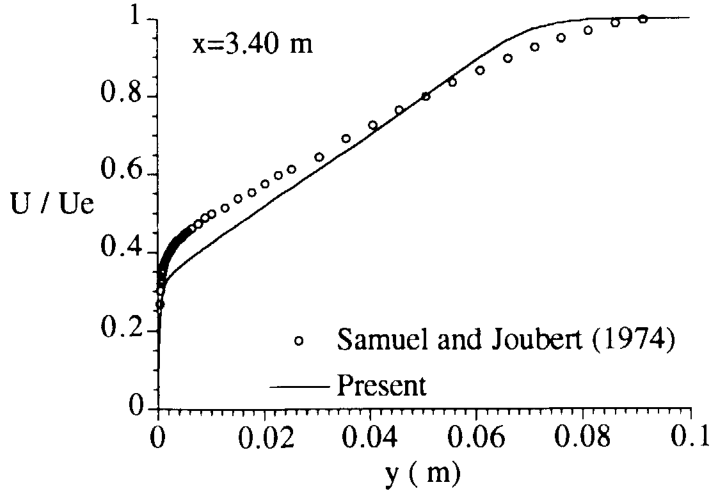

Fig. 38d Comparison of U with data at x = 3.40m.

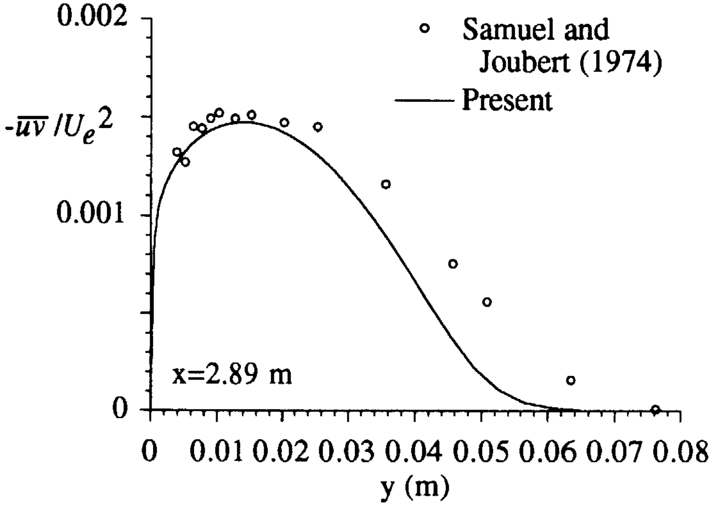

Fig. 38e Shear stress comparison at x = 2.89m.

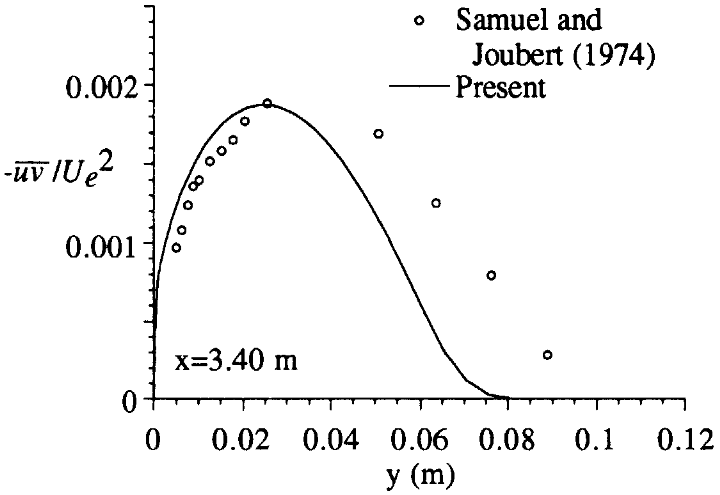

Fig. 38f Shear stress comparison at x = 2.89m.

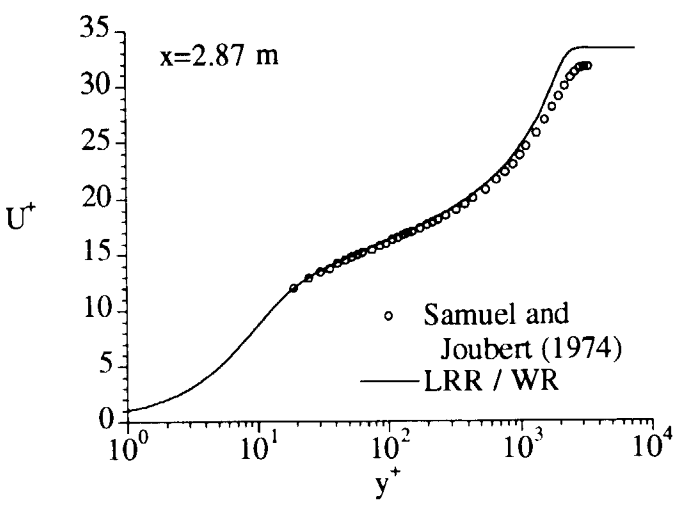

Fig. 39a Comparison of U+ with data at x = 2.87m.

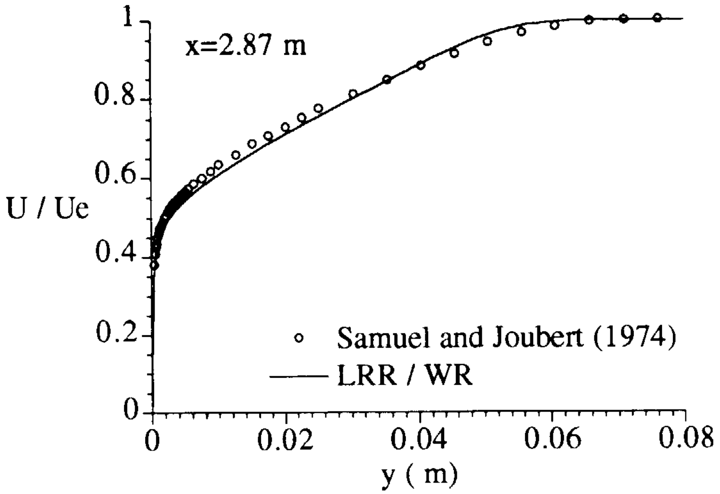

Fig. 39b Comparison of U with data at x = 2.87m.

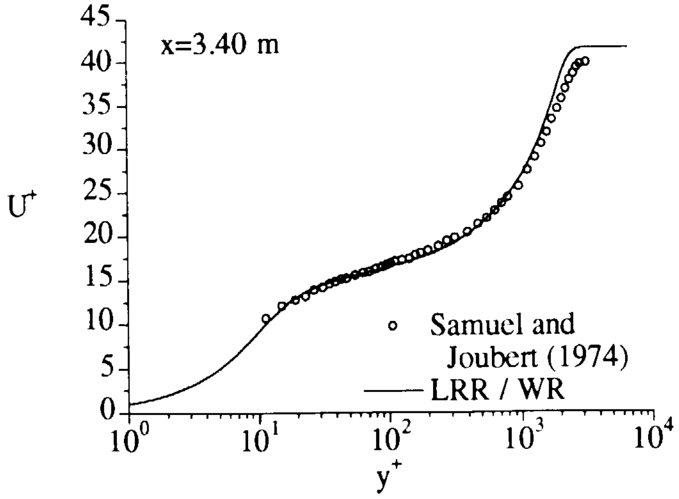

Fig. 39c Comparison of U+ with data at x = 3.40m.

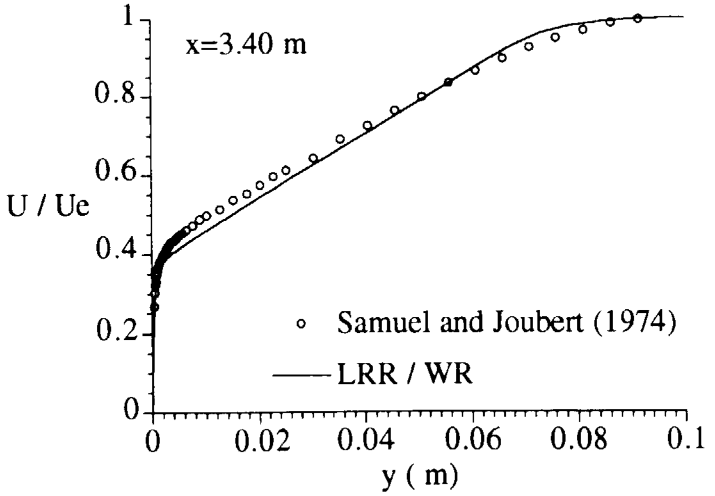

Fig. 39d Comparison of U with data at x = 3.40m.

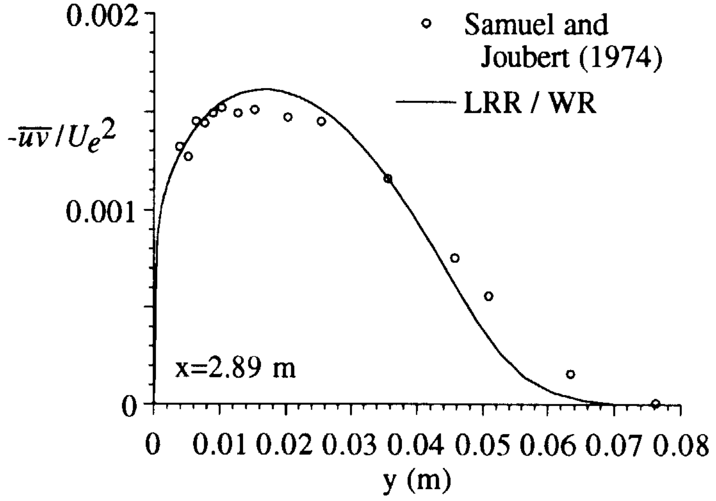

Fig. 39e Shear stress comparison at x = 2.89m.

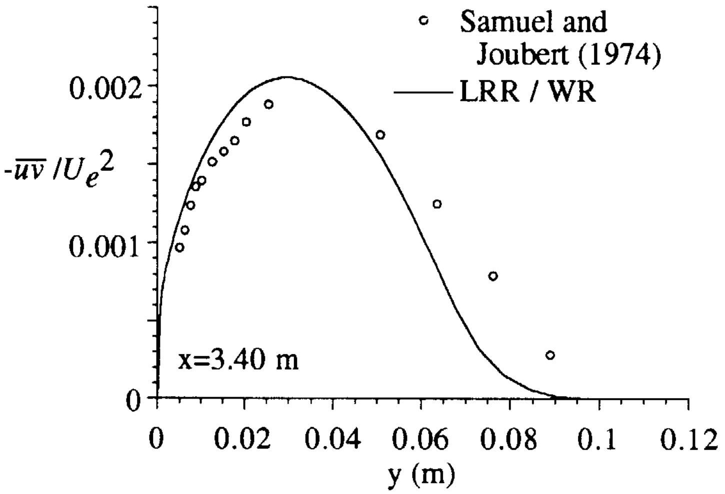

Fig. 39f Shear stress comparison at x = 3.40m.

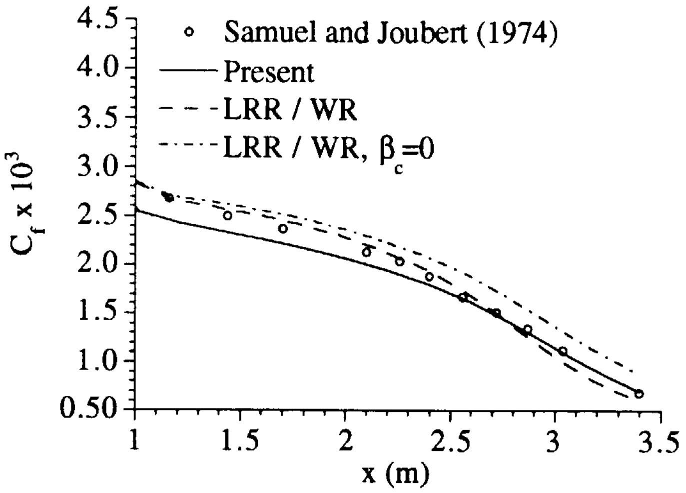

Fig. 40a Comparison of C_f development.

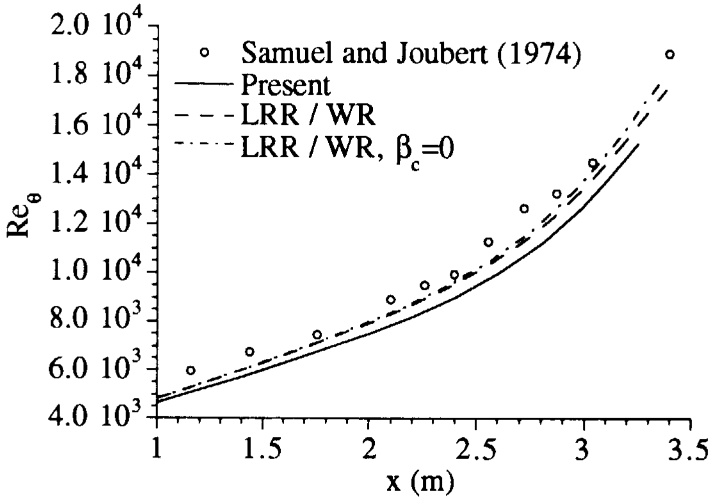

Fig. 40b Comparison of Re_θ development.

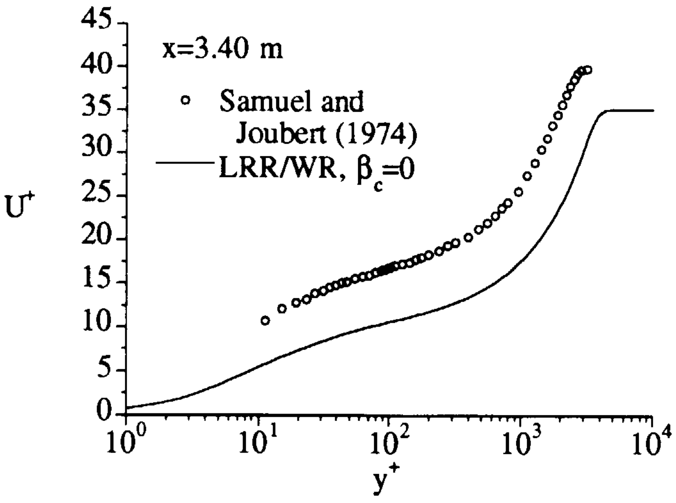

Fig. 40c Comparison of U^+ with data at x = *3.40m.*

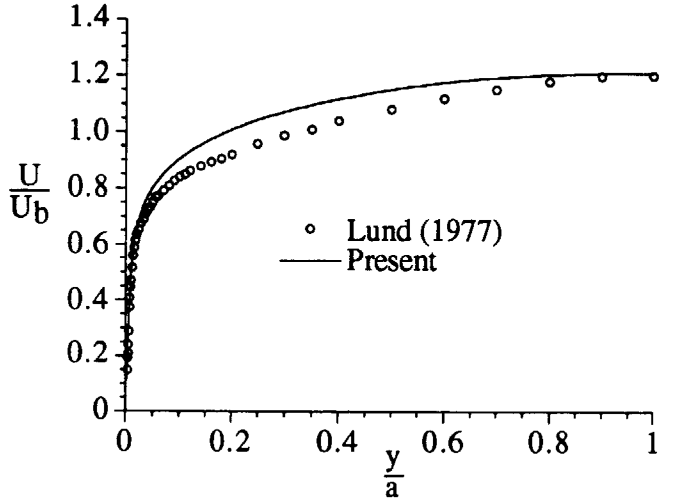

Fig. 41a Velocity profiles along the wall bisector.

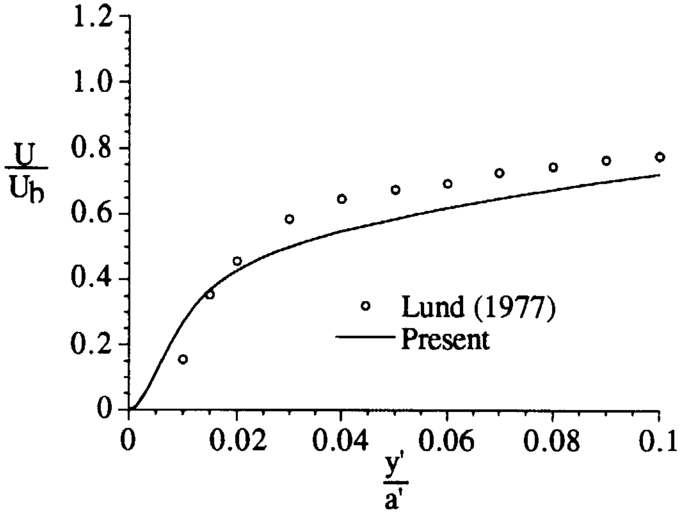

Fig. 41b Velocity profiles along the corner bisector.

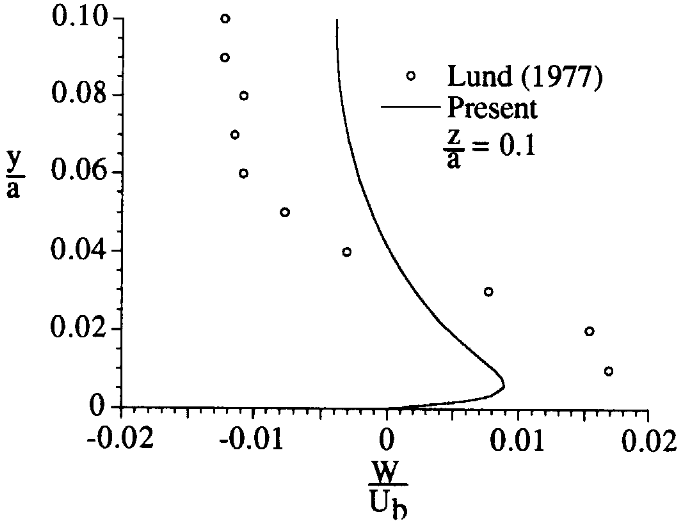

Fig. 41c Secondary velocity profiles at z/a = 0.1.

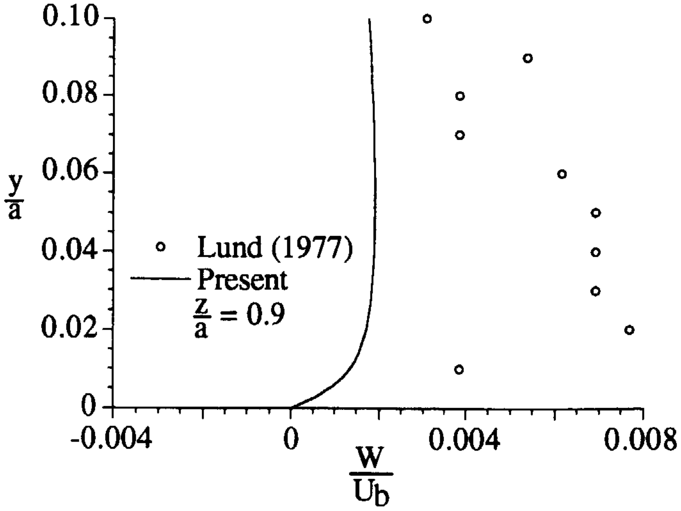

Fig. 41d Secondary velocity profiles at z/a = 0.9.

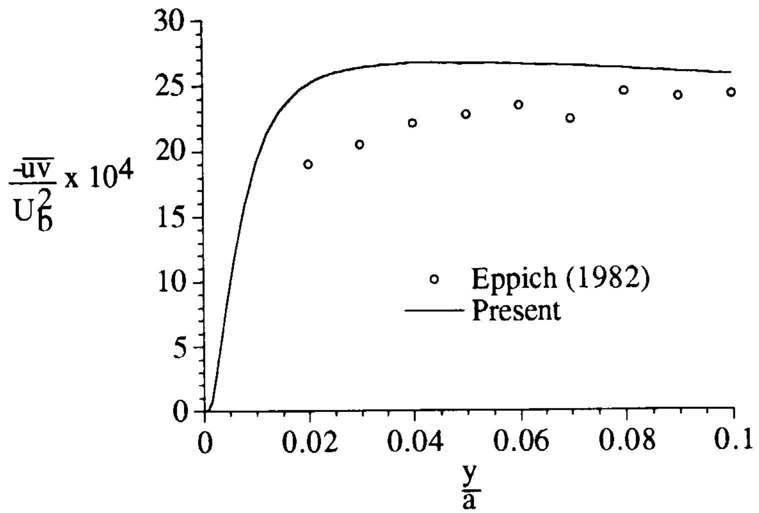

Fig. 41e Turbulent shear stress along the wall bisector.

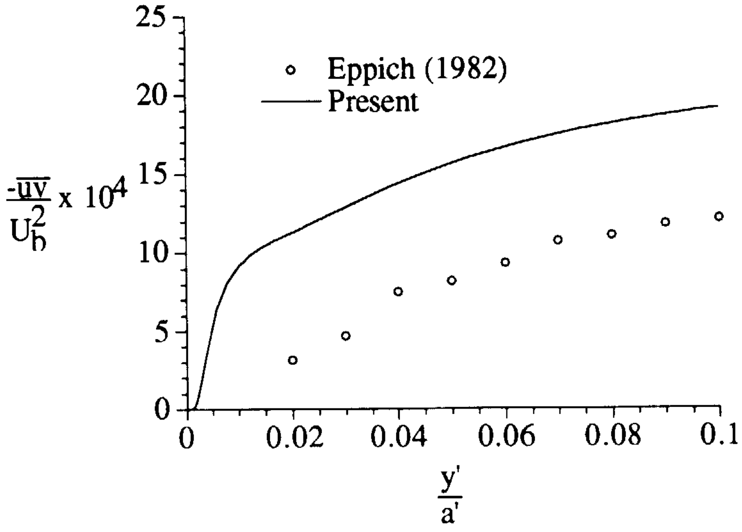

Fig. 41f Turbulent shear stress along the corner bisector.

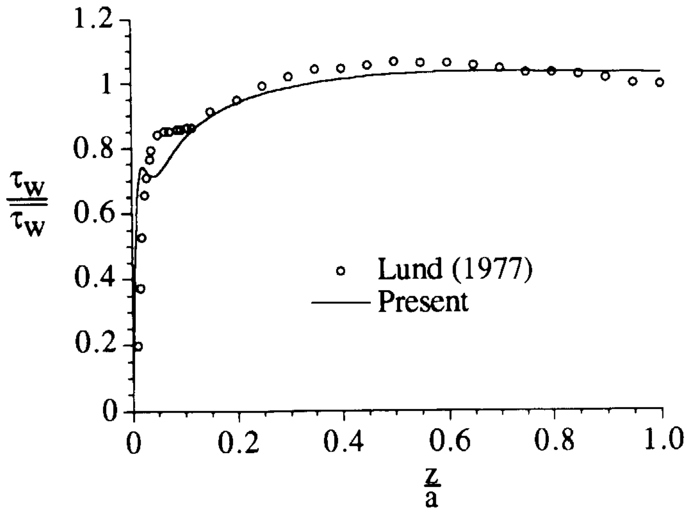

Fig. 41g Local wall shear stress distribution.

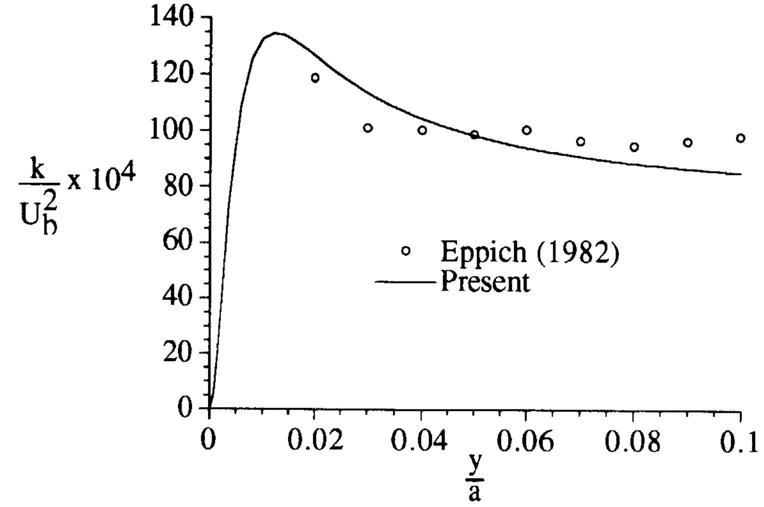

Fig. 42a Turbulent kinetic energy along the wall bisector.

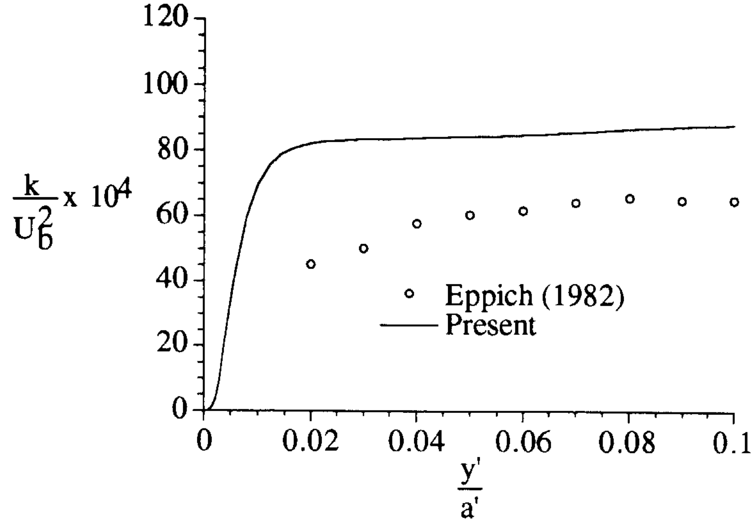

Fig. 42b Turbulent kinetic energy along the corner bisector.

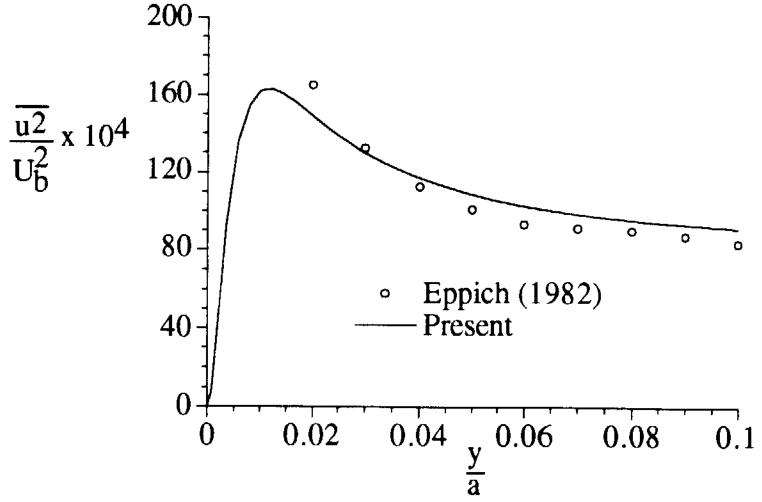

Fig. 42c x-direction normal stress along the wall bisector.

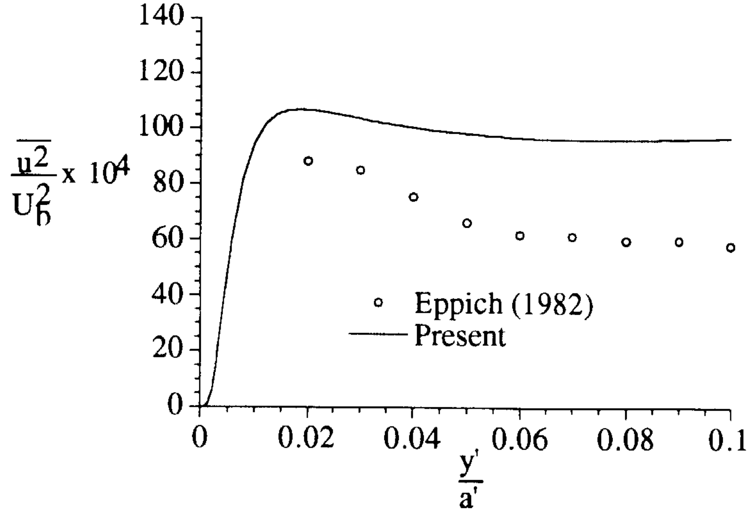

Fig. 42d x-direction normal stress along the corner bisector.

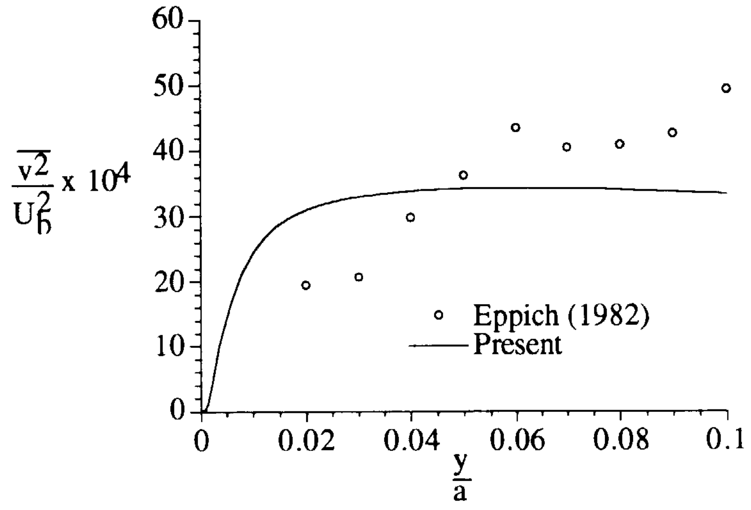

Fig. 42e y-direction normal stress along the wall bisector.

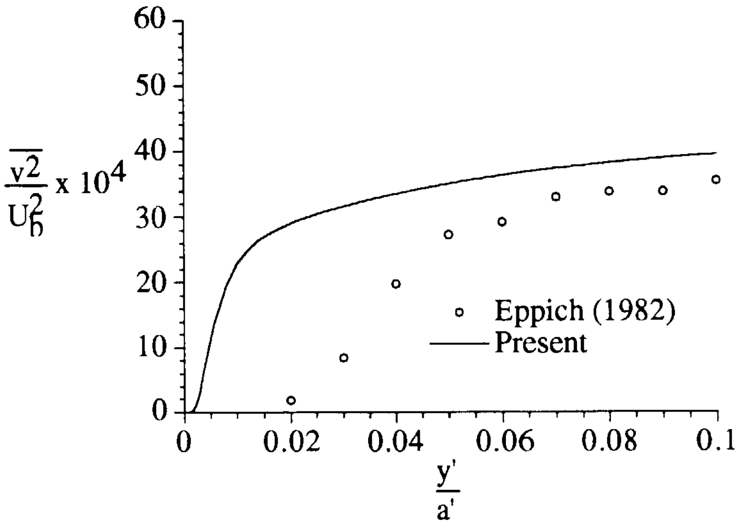

Fig. 42f y-direction normal stress along the corner bisector.

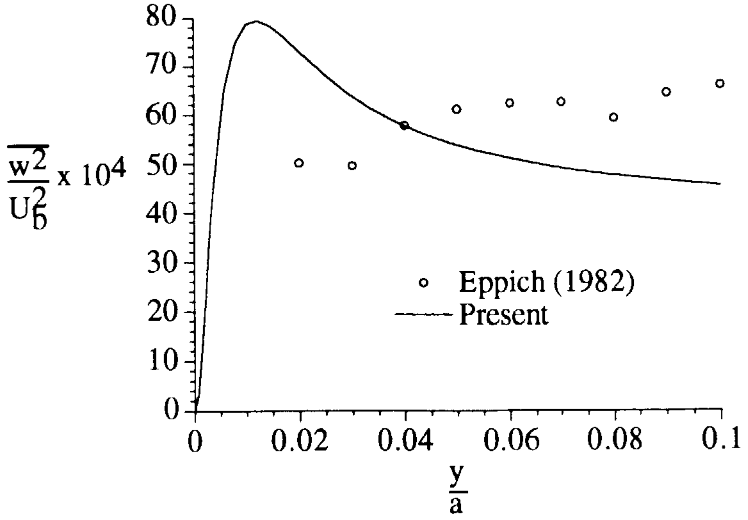

Fig. 42g z-direction normal stress along the wall bisector.

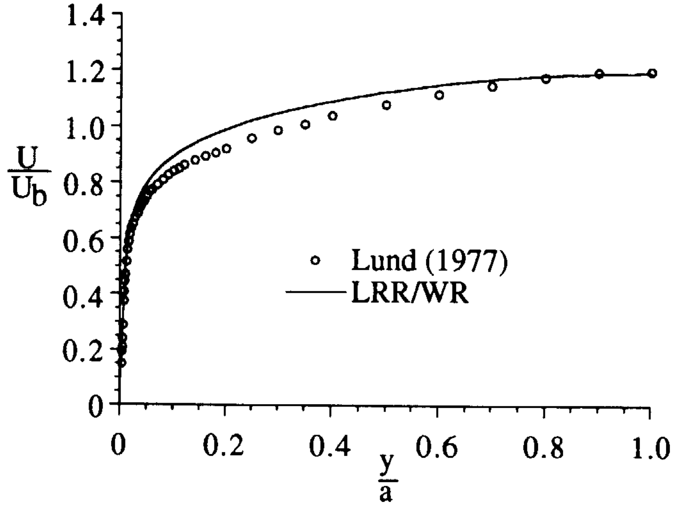

Fig. 43a Velocity profiles along the wall bisector.

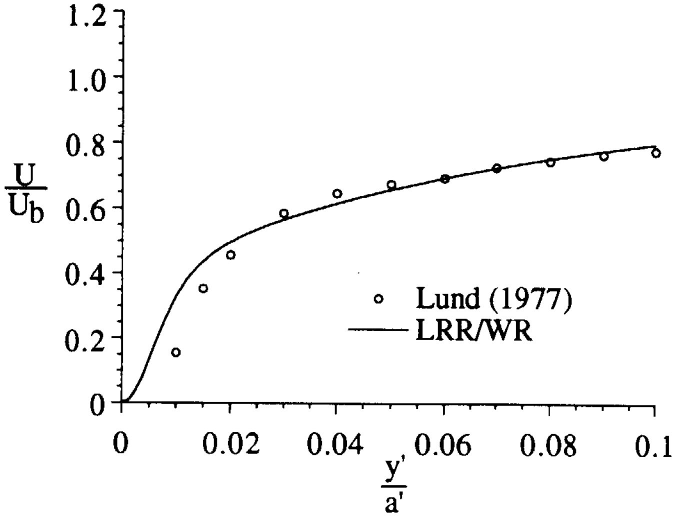

Fig. 43b Velocity profiles along the corner bisector.

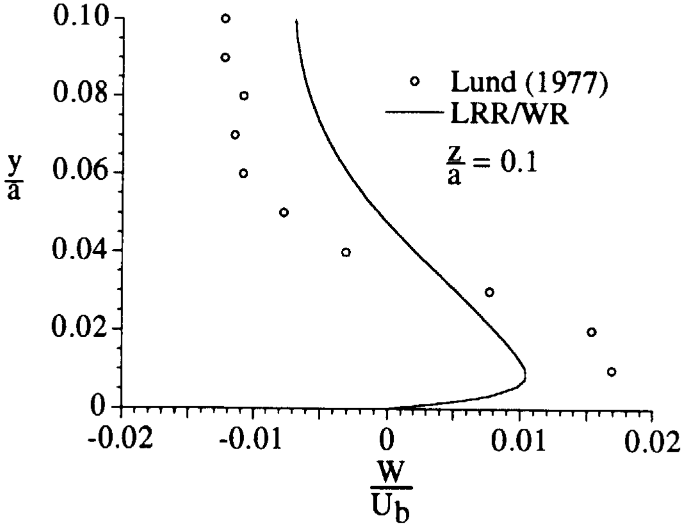

Fig. 43c Secondary velocity profiles at z/a = 0.1.

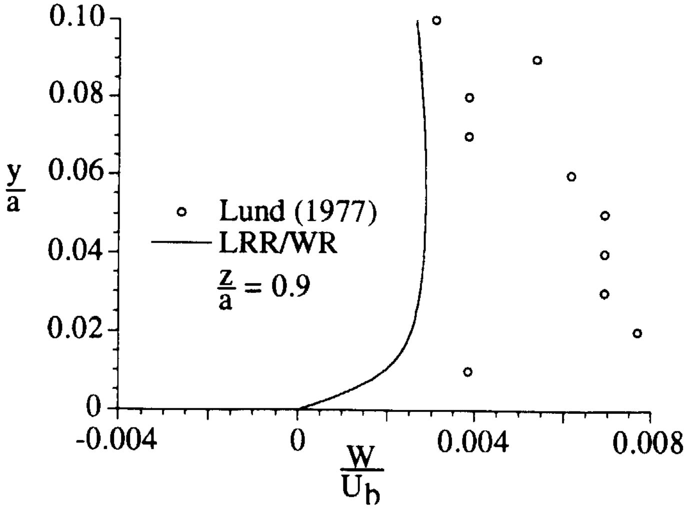

Fig. 43d Secondary velocity profiles at z/a 0.9.

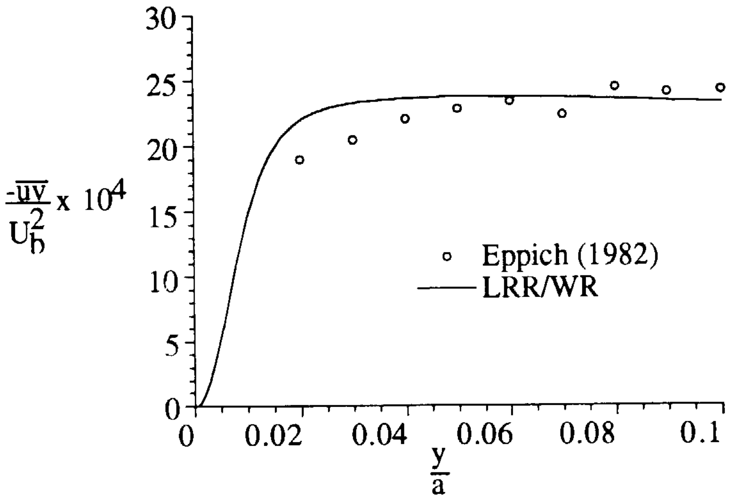

Fig. 43e Turbulent shear stress along the wall bisector.

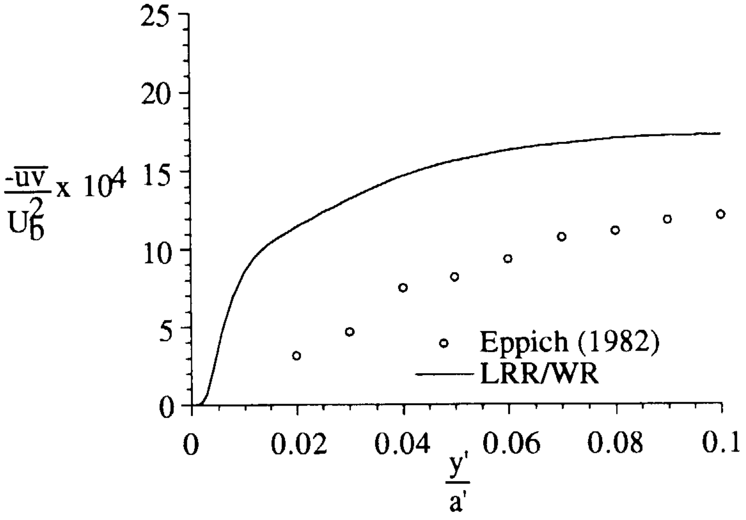

Fig. 43f Turbulent shear-stress along the corner bisector.

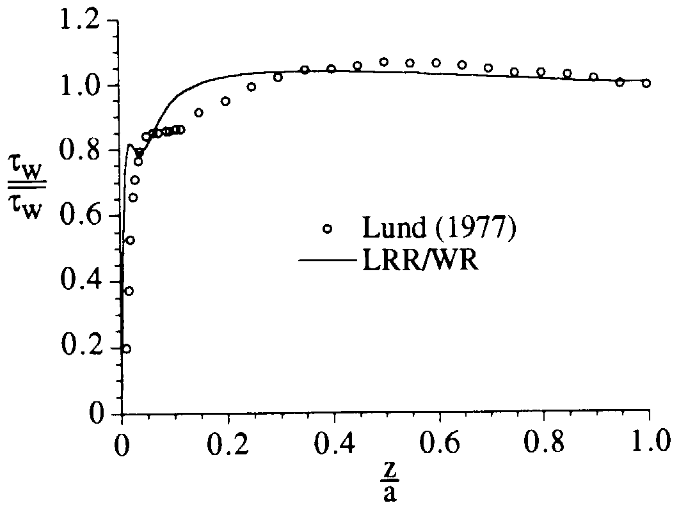

Fig. 43g Local wall shear stress distribution.

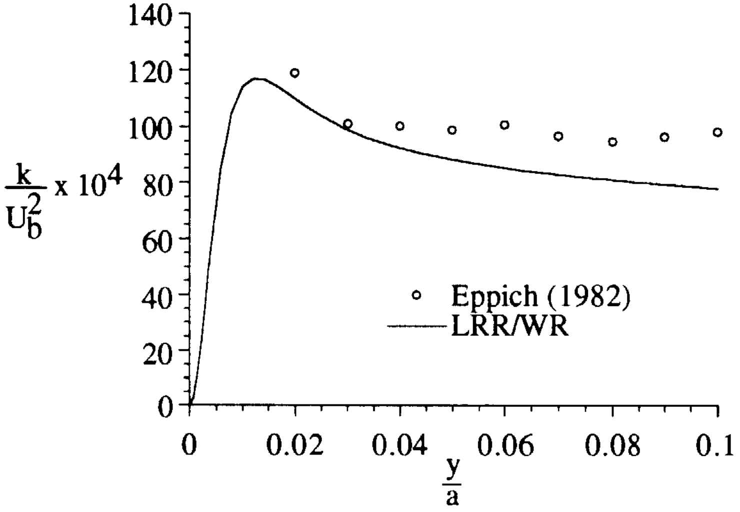

Fig. 44a Turbulent kinetic energy along the wall bisector.

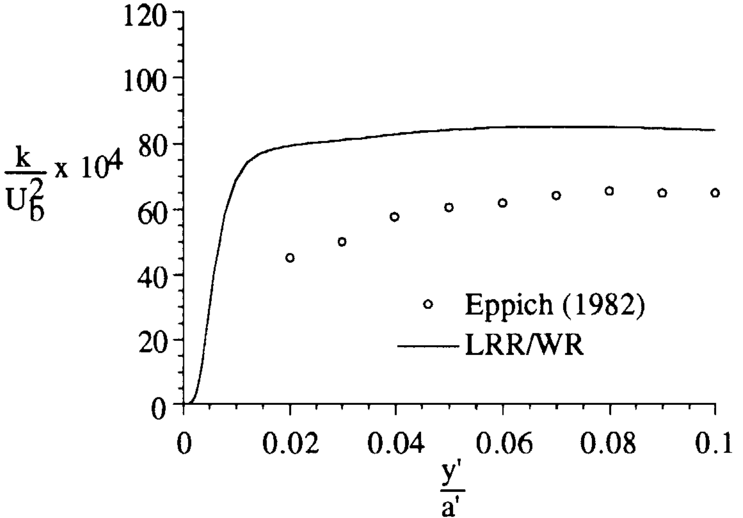

Fig. 44b Turbulent kinetic energy along the corner bisector.

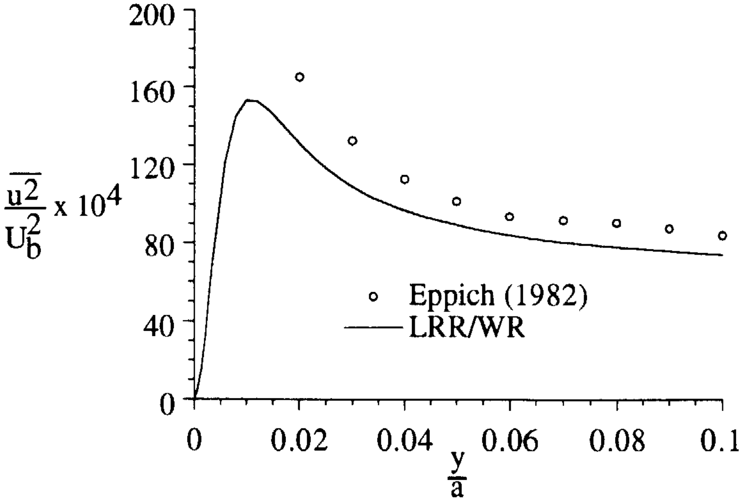

Fig. 44c x-direction normal stress along the wall bisector.

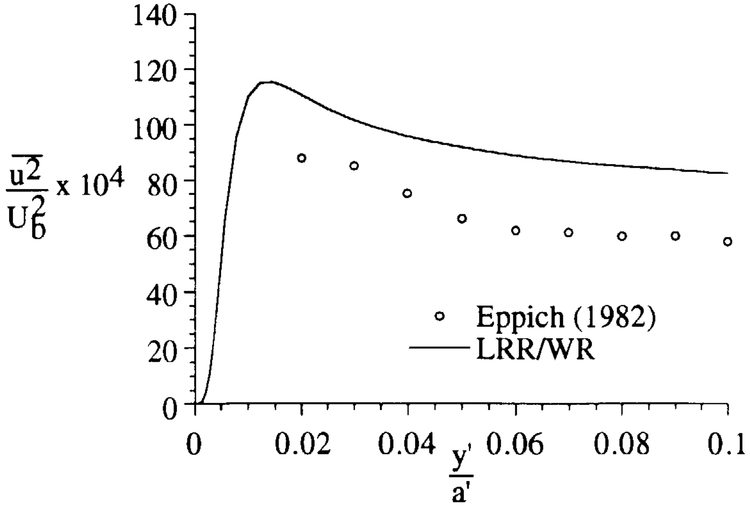

Fig. 44d x-direction normal stress along the corner bisector.

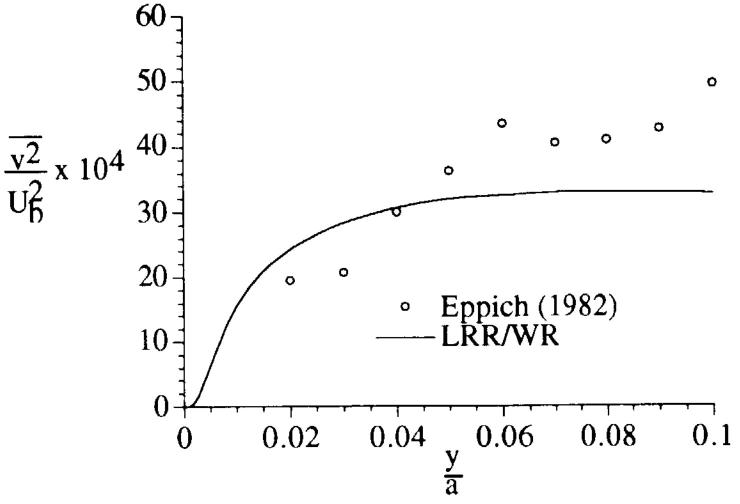

Fig. 44e y-direction normal stress along the wall bisector.

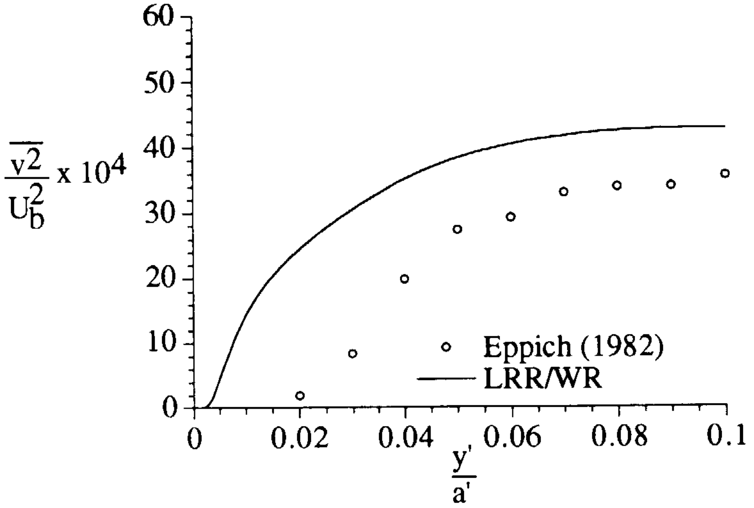

Fig. 44f y-direction normal stress along the corner bisector.

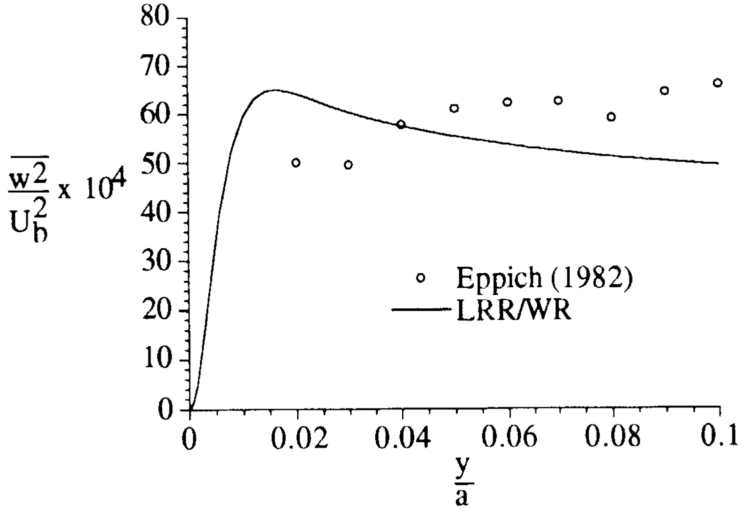

Fig. 44g z-direction normal stress along the wall bisector.

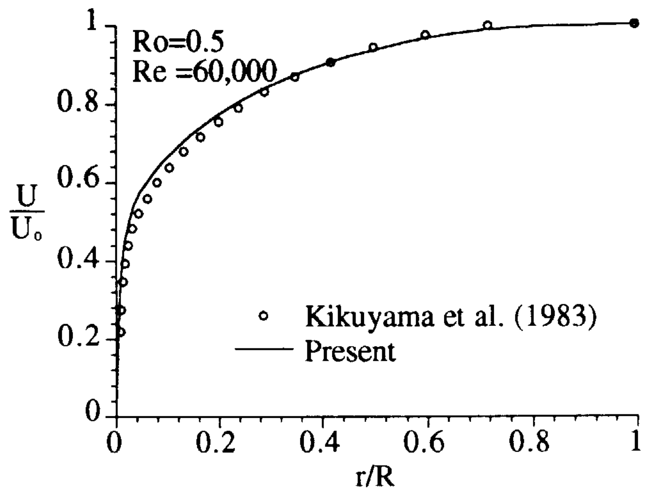

Fig. 45a Comparison of calculated U with data.

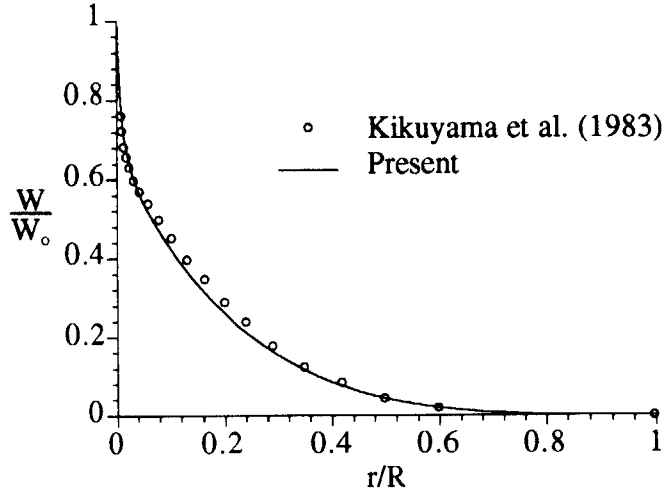

Fig. 45b Comparison of calculated W with data.

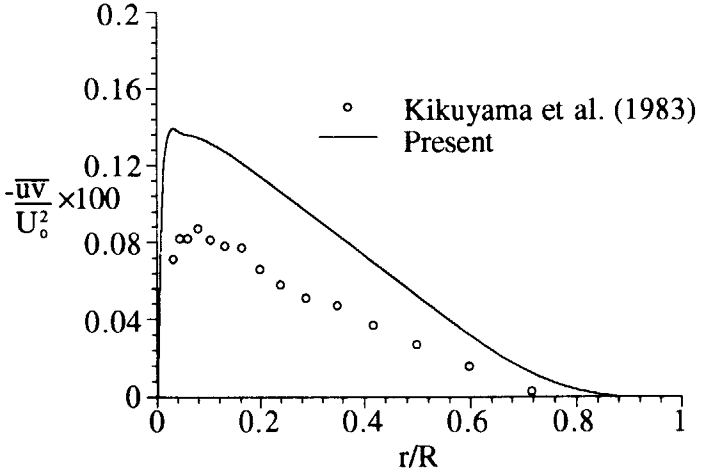

Fig. 45c Comparison of calculated $\overline{uv}$ with data.

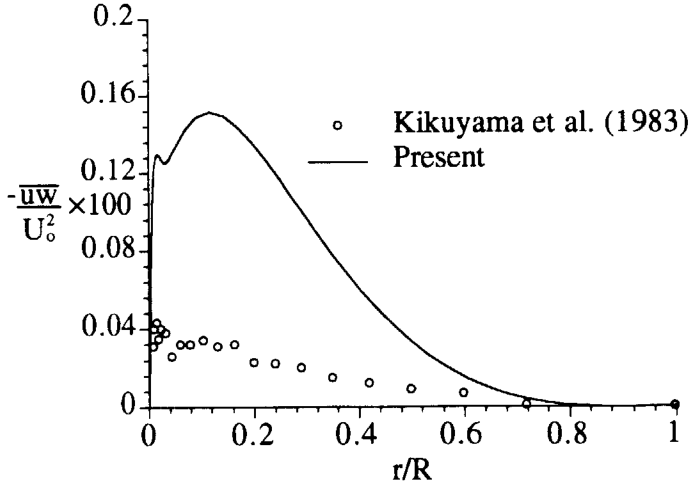

Fig. 45d Comparison of calculated $\overline{uw}$ with data.

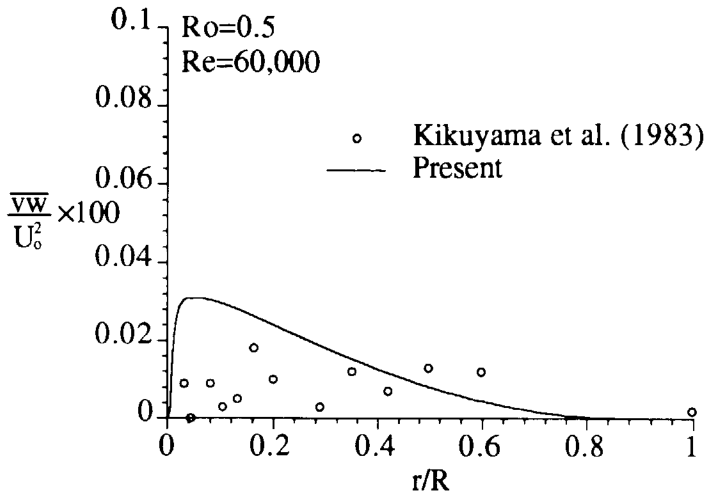

Fig. 45e Comparison of calculated $\overline{vw}$ with data.

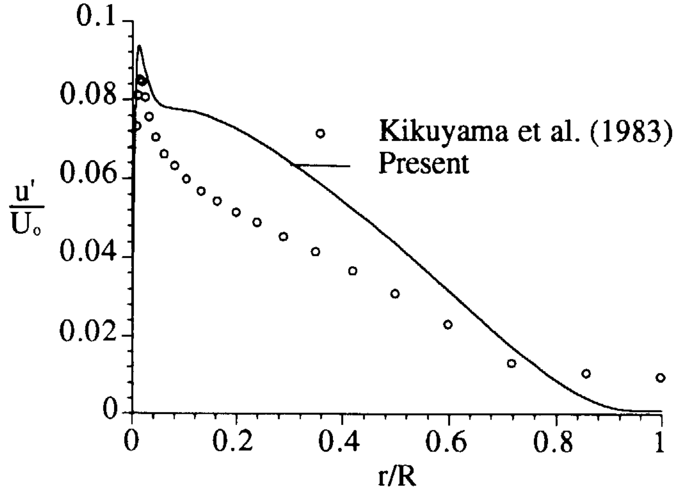

Fig. 45f Comparison of calculated u' with data.

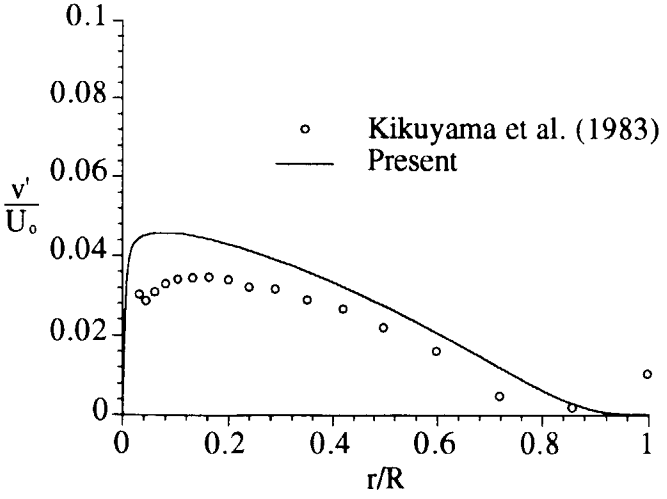

Fig. 45g Comparison of calculated v' with data.

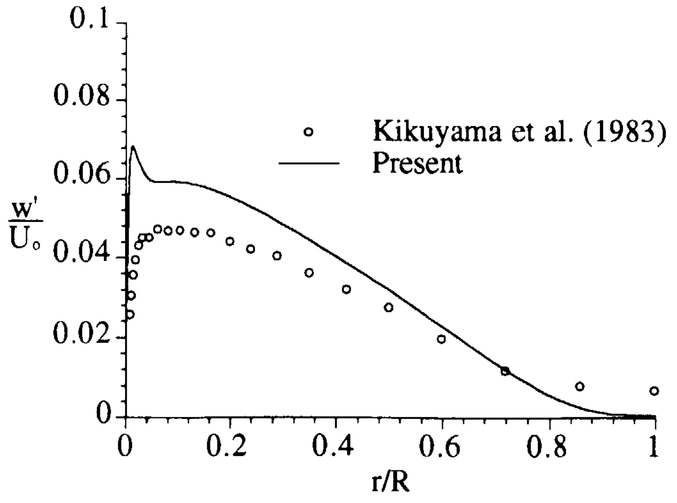

Fig. 45h Comparison of calculated w' with data.

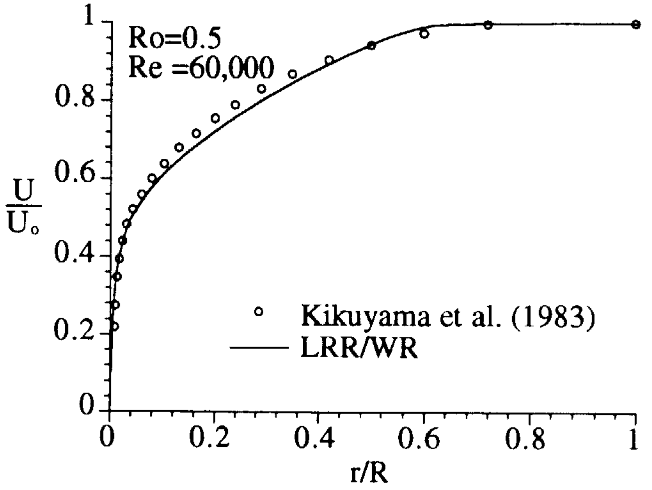

Fig. 46a Comparison of calculated U with data.

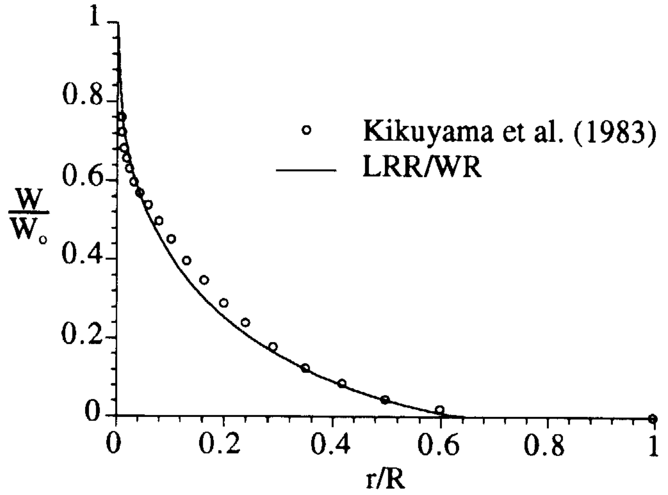

Fig. 46b Comparison of calculated W with data.

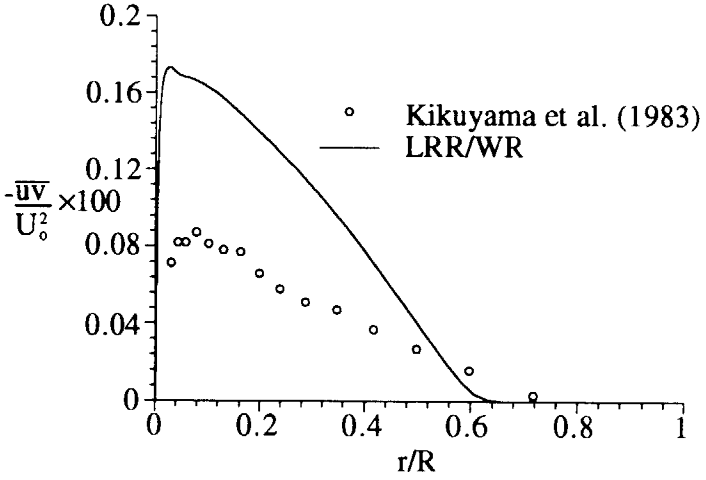

Fig. 46c Comparison of calculated $\overline{uv}$ with data.

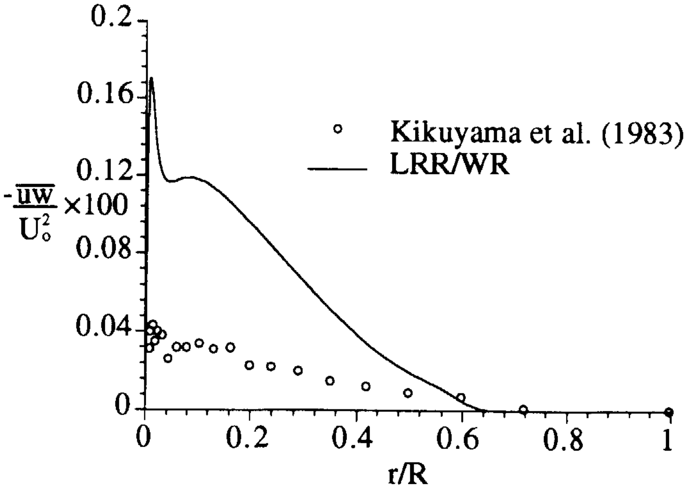

Fig. 46d Comparison of calculated $\overline{uw}$ with data.

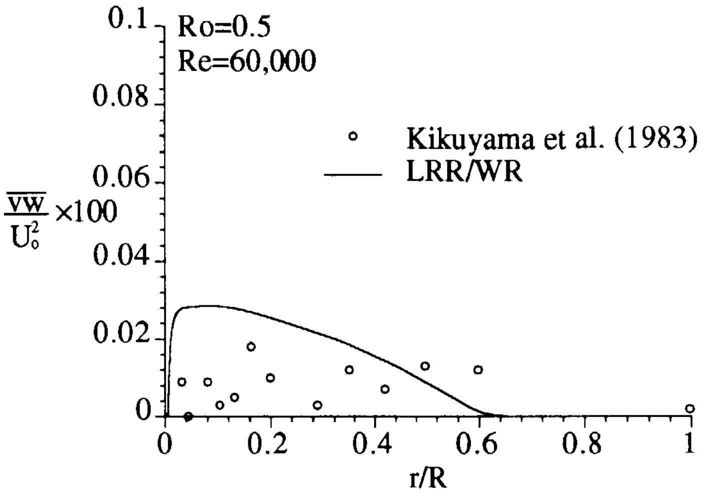

Fig. 46e Comparison of calculated $\overline{vw}$ with data.

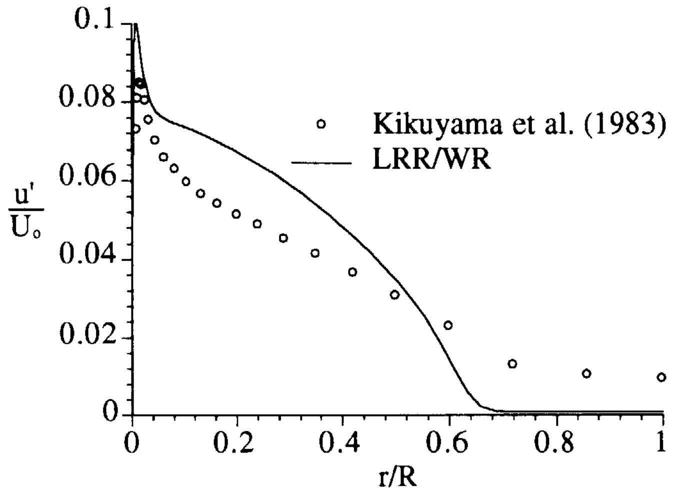

Fig. 46f Comparison of calculated u' with data.

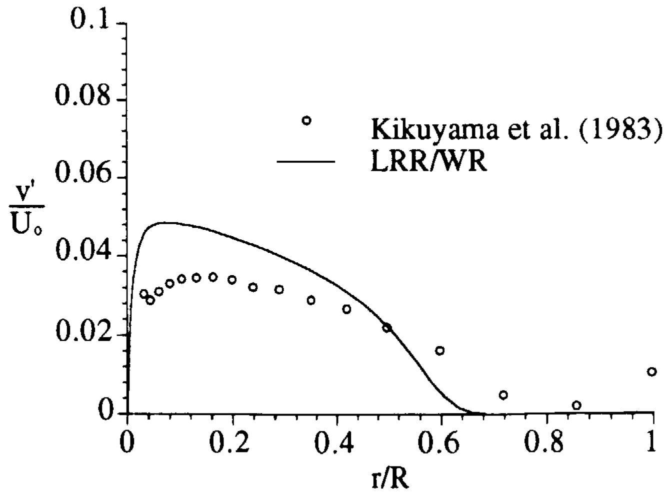

Fig. 46g Comparison of calculated v' with data.

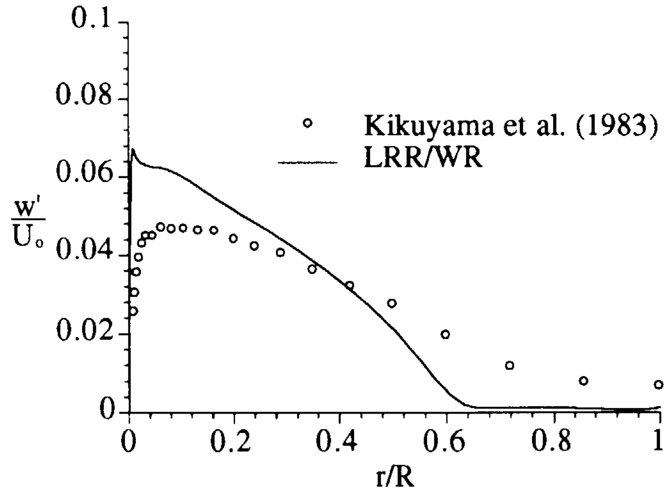

Fig. 46h Comparison of calculated w' with data.

REPORT DOCUMENTATION PAGE			Form Approved OMB No. 0704-0188

1. AGENCY USE ONLY (*Leave blank*)	2. REPORT DATE August 1994	3. REPORT TYPE AND DATES COVERED Contractor Report

4. TITLE AND SUBTITLE Development of a Near-Wall Reynolds-Stress Closure Based on the SSG Model for the Pressure Strain	5. FUNDING NUMBERS G NAG1-1080 WU 505-59-50-05
6. AUTHOR(S) R. M. C. So, H. Aksoy, T. P. Sommer, and S. P. Yuan	
7. PERFORMING ORGANIZATION NAME(S) AND ADDRESS(ES) Arizona State University Department of Mechanical and Aerospace Engineering Tempe, AZ 85287	8. PERFORMING ORGANIZATION REPORT NUMBER ASU/TFML-94-7
9. SPONSORING / MONITORING AGENCY NAME(S) AND ADDRESS(ES) National Aeronautics and Space Administration Langley Research Center Hampton, VA 23681-0001	10. SPONSORING / MONITORING AGENCY REPORT NUMBER NASA CR-4618

11. SUPPLEMENTARY NOTES

Langley Technical Monitor: Thomas B. Gatski

12a. DISTRIBUTION / AVAILABILITY STATEMENT Unclassified - Unlimited Subject Category: 02	12b. DISTRIBUTION CODE

13. ABSTRACT (*Maximum 200 words*)

In this research, a near-wall second-order closure based on the Speziale et al. (1991) or SSG model for the pressure-strain term is proposed. Unlike the LRR model, the SSG model is quasi-nonlinear and yields better results when applied to calculate rotating homogeneous turbulent flows. An asymptotic analysis near the wall is applied to both the exact and modeled equations so that appropriate near-wall corrections to the SSG model and the modeled dissipation-rate equation can be derived to satisfy the physical wall boundary conditions as well as the asymptotic near-wall behavior of the exact equations. Two additional model constants are introduced and they are determined by calibrating against one set of near-wall channel flow data. Once determined, their values are found to remain constant irrespective of the type of flows examined. The resultant model is used to calculate simple turbulent flows, near separating turbulent flows, complex turbulent flows and compressible turbulent flows with a free stream Mach number as high as 10. In all the flow cases investigated, the calculated results are in good agreement with data. This new near-wall model is less ad hoc, physically and mathematically more sound and eliminates the empiricism introduced by Zhang (1993). Therefore, it is quite general, as demonstrated by the good agreement achieved with measurements covering a wide range of Reynolds numbers and Mach numbers.

14. SUBJECT TERMS near-wall modeling, complex flow modeling, compressible turbulence modeling, near separating flow modeling	15. NUMBER OF PAGES 136
	16. PRICE CODE A07

17. SECURITY CLASSIFICATION OF REPORT Unclassified	18. SECURITY CLASSIFICATION OF THIS PAGE Unclassified	19. SECURITY CLASSIFICATION OF ABSTRACT Unclassified	20. LIMITATION OF ABSTRACT Unlimited